The Influence of Sintering Additives on the Microstructure and Properties of AlON

Yechezkel Ashuach

The Influence of Sintering Additives on the Microstructure and Properties of ALON

Research Thesis

Submitted in Partial Fulfillment of the Requirements for the Degree of Master of Science in Materials Engineering

Yechezkel Ashuach

Submitted to the Senate of
the Technion – Israel Institute of Technology

TEVET, 5764 HAIFA DECEMBER 2003

The research thesis was done under the supervision of Prof. Wayne D. Kaplan in the Faculty of Materials Engineering.

ACKNOWLEDGEMENTS

I would like to thank Prof. Wayne D. Kaplan for his support, help and dedicated guidance.

I deeply appreciate the real support of Rafael – Ballistics and Explosives Dept. of my education and of this research.

I would like to thank Rafael – Materials and Processes Dept. for the free access they gave me to all their equipment.

I am deeply grateful to David Gorni, Shimshon Bar-Ziv, Shlomit Zamir, Oren Aharon, Itzhak Baum and Yehoshua Hachamo for their assistance.

I would like to thank Dr. Alex Berner for his help in the quantitative analyses.

Thanks to Hedva Tzipin for her assistance in transmittance measurements.

Thanks to Mike Lieberthal and my friends at the ceramic group.

Special thanks to Dr. Shuki Yeshurun for his support during all stages of this research.

Table of Contents

Abstract **1**

List of symbols and abbreviations **3**

1. Introduction **5**

2. Literature survey **6**

2.1 Composition and structure of AlON 6

2.2 Synthesis and processing 13

2.2.1 Reaction sintering 14

2.2.2 Carbothermal nitridation of alumina 18

2.2.3 Other synthesis processes 19

2.2.4 Hot-pressing of AlON 20

2.2.5 Microwave sintering of AlON 21

2.2.6 AlON composites 21

2.3 Influence of additives 22

2.3.1 Additives to translucent alumina 22

2.3.2 Additives to transparent AlON 26

2.4 Properties 28

2.4.1 Mechanical properties 29

2.4.2 Optical properties 30

2.4.3 Oxidation resistance 31

2.4.4 Chemical stability 32

2.5 Transparency 33

2.5.1 Light-matter interaction 33

2.5.1.1 Reflection 35

2.5.1.2 Absorption 35

2.5.1.3 Scattering 36

2.5.2 Microstructural sources of light scattering and the influence on transparency 38

2.5.2.1 Light scattering from porosity 39

Table of Contents (Continued)

2.5.2.2 Influence of grain size on scattering 41

2.6 Applications 42

3. Research goals 44

4. Experimental methods 45

4.1 Process description 45

4.2 Characterization methods 48

4.2.1 Density 48

4.2.2 Hardness 48

4.2.3 Chemical analysis 48

4.2.4 X-ray diffraction (XRD) 48

4.2.5 Scanning electron microscope (SEM) 49

4.2.6 Energy dispersive spectroscopy (EDS) 49

4.2.7 Wavelength dispersive spectroscopy (WDS) 49

4.2.8 Transmission electron microscope (TEM) 49

4.2.9 Spectrophotometer 49

5. Results 50

5.1 Process development 50

5.2 Dilatometric analysis 51

5.3 Phase identification by XRD 54

5.3.1 XRD patterns of AlON 54

5.3.2 Lattice parameter calculations 59

5.4 Quantitative elemental analysis 60

5.4.1 Chemical analysis 60

5.4.2 EDS and WDS analyses 62

5.5 Microstructure characterization 63

5.5.1 Microstructure of etched samples 63

5.5.2 Fracture surfaces 68

5.5.3 Grain size measurements 77

Table of Contents (Continued)

5.5.4 TEM characterization 78

5.6 Light transmission 81

5.7 Oxidation resistance experiment 82

5.8 Hardness measurements 84

6. Discussion 85

6.1 Process discussion

6.2 Influence of additives discussion

6.3 Liquid phase discussion

7. Summary and Conclusions 89

8. Recommendations for Future Work 90

9. References 91

Figure List

Figure 2.1. Phase diagram for the AlN-Al_2O_3 pseudo-binary system. 6

Figure 2.2. Schematic drawing of the spinel structure. 10

Figure 2.3. Effect of reaction temperature on Al_2O_3, AlN, and AlON volume-fraction (firing time of 2.5 hrs), expressed by XRD peak intensity ratios. 16

Figure 2.4. Effect of reaction time on unreacted AlN fraction (firing temperature of: □ 1820°C , ■ 1750°C). 16

Figure 2.5. Dependence of lattice parameter of AlON on the concentration of starting Al_2O_3. 17

Figure 2.6. a) Final density and b) final grain size, as a function of MgO concentration in sintered alumina samples. 24

Figure 2.7. Schematic phase diagram showing the composition range of the highest light transmission of alumina with MgO, Y_2O_3 and La_2O_3 additives. 26

Figure 2.8. In-line transmittance of AlON in UV, visible and IR wavelengths. 30

Figure 2.9. AlON window fabricated by Raytheon in 1986. 31

Figure 2.10. Oxidation of AlON at various temperatures as a function of time in air. 32

Figure 2.11. Illustration of the light transmission of (a) translucent material with a high diffuse transmission and a low in-line transmission and (b) transparent material with a low diffuse transmission and a high in-line transmission. 33

Figure 2.12. The interaction of light with a transparent material. 34

Figure 2.13. The effect of particle size on the relative scattering coefficient. 37

Figure 2.14. Light scattering at grain boundaries occurs only in anisotropic materials. 38

Figure 2.15. Calculated transmission curves for an alumina sample of 0.5 mm thickness with 0.2% porosity of different uniform sizes r, as a function of wavelength. 40

Figure List (Continued)

Figure 2.16. Calculated in-line and total (including forward scattering) transmission at 600 nm, 0.1% porosity and 0.8 mm thickness, assuming that the pores are monodispersed and randomly divided over a homogeneous matrix with n=1.76 (for alumina). 41

Figure 5.1. The relation between relative shrinkage and the sintering time of pure and doped AlON. 53

Figure 5.2. The relation between relative shrinkage and the sintering temperature of pure and doped AlON. 53

Figure 5.3. a) XRD of AlON powder synthesized at 1750°C for 4 hrs, b) XRD of AlON powder produced by Sienna; ○ - AlON , ♦ - AlN , ● - Al_2O_3. 55

Figure 5.4. XRD of E-type AlON sample sintered at 1800°C for 2 hrs and then at 1950°C for 2 more hrs: a) as sintered, b) after polishing; ○ – AlON , Δ - AlN. 57

Figure 5.5. XRD patterns of: a) J-type sample, b) LA-type sample. 58

Figure 5.6. Lattice parameters determined for various AlON samples (doped and undoped) with different Al_2O_3/AlN ratios, with a comparison to some results from the literature. 60

Figure 5.7. Optical micrograph of a J-type sample sintered at 2010°C for 12 hrs (originally x12.5). 64

Figure 5.8. Optical micrograph of an MC-type sample sintered at 2010°C for 12 hrs (originally x12.5). 64

Figure 5.9. Optical micrograph of an MB-type sample sintered at 2010°C for 12 hrs (originally x12.5). 65

Figure 5.10. Optical micrograph of an MYA-type sample sintered at 1930°C for 12 hrs (originally x12.5). 65

Figure 5.11. Optical micrograph of an LA-type sample sintered at 1930°C for 12 hrs (originally x12.5). 66

Figure 5.12. Optical micrograph of a YLA-type sample sintered at 1930°C for 12 hrs (originally x12.5). 66

Figure List (Continued)

Figure 5.13. SEM microstructure of an MLD-type sample sintered at 2000°C for 12 hrs (originally x40). 67

Figure 5.14. Optical micrograph of a transparent sample of Surmet (originally x25). 68

Figure 5.15. SEM fracture surface of an E-type sample sintered in two steps: 1800°C for 2 hrs and 1950°C for another 2 hrs (originally x1000). 69

Figure 5.16. SEM fracture surface of an F-type sample sintered at 1950°C for 4 hrs (heating rate of 500 °C/hr, originally x500). 70

Figure 5.17. SEM fracture surface of an F-type sample sintered at 1950°C for 4 hrs (heating rate of 900 °C/hr, originally x500). 70

Figure 5.18. SEM fracture surface of an I-type sample sintered at 2000°C for 12 hrs (originally x250). 71

Figure 5.19. SEM fracture surface of an MA-type sample sintered at 1950°C for 4 hrs (originally x500). 72

Figure 5.20. SEM fracture surface of an LA-type sample sintered at 1950°C for 12 hrs (originally x250). 72

Figure 5.21. SEM fracture surface of a YA-type sample sintered at 2000°C for 12 hrs (originally x250). 73

Figure 5.22. SEM fracture surface of a YLA-type sample sintered at 2000°C for 12 hrs (originally x250). 73

Figure 5.23. Elemental mapping SEM micrographs of a fracture surface of an MLD sample sintered at 1950°C for 12 hrs (originally x500). 75

Figure 5.24. XRD of an MLD-type AlON sample sintered at 1950°C for 12 hrs; ○ - AlON , ∇ - $LaAl_{11}O_{18}$. 76

Figure 5.25. TEM micrograph of a grain boundary in an MLA-type sample. 79

Figure 5.26. Electron diffraction pattern from an AlON grain in an MLA sample. 79

Figure 5.27. TEM micrograph of a triple point in a sample of transparent AlON from Surmet. 80

Figure 5.28. Electron diffraction pattern from an AlON grain in a transparent sample from Surmet. 80

Figure List (Continued)

Figure 5.29. Photographs of AlON samples lying on a paper with the word "ALON": a) pure AlON (F-type), sintered at 2025°C for 4 hrs, 1.66 mm thick sample; b) doped AlON (MA-type), sintered at 2025°C for 12 hrs, 2.8 mm thick sample. 81

Figure 5.30. Transmission curves of an MA-type AlON sample and the transparent AlON produced by Surmet, in the UV, visible and IR regions. 82

Figure 5.31. XRD runs of an AlON sample of Surmet (which was originally transparent) before and after an oxidation resistance experiment at 2000°C for 4 hrs: a) before the experiment, b) the lower (transparent) part after the experiment, c) the upper (opaque) part after the experiment; ○ - AlON , Δ - AlN. 83

Figure 5.32. Optical micrograph of an etched AlON sample of Surmet after heating at 2000°C for 4 hrs. 83

Figure 6.1. Phase diagram of the La_2O_3-Al_2O_3 quasi-binary system above 1800°C. 86

Table List

Table 2.1.	Aluminum oxynitride phases observed in the AlN-Al_2O_3 pseudo-binary system.	9
Table 2.2.	Compositions of aluminum oxynitride by McCauley's constant anion model.	12
Table 2.3.	Chemical reactions known to produce AlON phases.	13
Table 2.4.	Representative properties of AlON compared with other similar ceramics: α-Al_2O_3, AlN and transparent spinel ($MgAl_2O_4$).	29
Table 4.1.	Raw materials (α-Al_2O_3, AlN) used to synthesize AlON.	45
Table 4.2.	Additive substances used in the synthesis of AlON.	46
Table 4.3.	Compositions of powder mixtures prepared to sinter AlON.	47
Table 5.1.	Reflections attributed to AlON with lattice parameter of 0.7950 nm (Cu Kα radiation). The last column indicates whether the reflection was used while determining the lattice parameter.	56
Table 5.2.	Compositions of powder mixtures and Surmet transparent AlON plate. In parentheses are the concentrations of dopants added to the mixtures.	61
Table 5.3.	Compositions of sintered AlON samples measured by EDS and WDS.	62
Table 5.4.	Average grain sizes measured for various AlON samples, with different composition types and sintering temperatures and times.	77
Table 5.5.	Knoop hardness measured for various AlON samples, with different composition types and sintering temperatures and times.	84

Abstract

γ-aluminum oxynitride (AlON) is a hard transparent ceramic material. Like many other ceramics, it has a good thermal and chemical stability. This unique combination of properties makes AlON an attractive candidate for a wide range of applications, while current focus is on transparent armor and missile domes. Another material which has similar properties is sapphire, but as a single crystal it is manufactured through expensive methods, while polycrystalline AlON is prepared by conventional sintering methods. Thus, AlON can be an alternative material to sapphire wherever high hardness and transparency in the visible and infrared regions are needed.

AlON is a solid solution in the Al_2O_3-AlN pseudo-binary system. Its crystallographic structure is cubic spinel, thus its optical properties are isotropic. It is usually manufactured from powder mixtures of alumina and either AlN or carbon black. Pressureless sintering of AlON usually results in a white, single phase, ceramic material. Pores are the most important light scattering centers in AlON. The production of transparent AlON is extremely challenging because residual porosity must be reduced to an absolute minimum, beyond that required from conventional ceramic processing. This can be achieved by introducing sintering additives, which assist densification through liquid phase sintering.

The main goal of the current research was to study the influence of sintering additives (magnesium, lanthanum and yttrium) on the microstructure and light transmission of AlON. As a first stage towards this goal, a high temperature (~2000°C) reaction sintering process was developed. Dopants were added to the Al_2O_3 and AlN starting powders and the sintered microstructure was investigated as a function of dopant concentration, and sintering temperature and time.

Mg, La and Y doping resulted in significantly improved materials relative to undoped AlON, with much less porosity. However, while Y doping causes a small amount of residual large pores, Mg and La doping (together or separately) resulted in a dense microstructure (grain size of ~150 μm) with the highest degree of transparency, due to very low residual porosity. It was shown that a dopant concentration above the

solubility limit results in a secondary phase at grain boundaries, which scatters light, and thus should be avoided. The higher the sintering temperature, the larger the grain size, and longer dwells at this temperature resulted in better transparency, because of more efficient porosity removal via grain boundary diffusion.

List of Symbols and Abbreviations

Å - Angstrom (length unit)

A - The fraction of absorbed light

a - Crystallographic Unit Cell Parameter

AlON - γ-Aluminum Oxynitride

at.% - Atomic Percent

BSE - Backscattered Electrons

°C - Celsius Degrees (temperature unit)

c - Light velocity in vacuum

cm - Centimeter (length unit)

EDS - Electron Dispersive Spectroscopy

eV - Electron-Volt (energy unit)

FCC - Face Centered Cubic crystal structure

g - Gram (weight unit)

GPa - Giga-Pascal (stress or pressure unit)

hrs - Hours (time unit)

ICP-OE- Inductively Coupled Plasma Optical Emission Spectroscopy

IGF - Inert Gas Fusion

IR - Infrared

K - Kelvin (temperature unit)

kV - Kilovolt (voltage unit)

λ - Wavelength

l - The thickness of a plate

mA - Milliampere (current unit)

min - Minute (time unit)

μm - Micrometer (length unit)

mm - Millimeter (length unit)

mol% - Mole Percent

MPa - Mega-Pascal (stress or pressure unit)

n - Refractive Index

nm - Nanometer (length unit)

ppm - Parts Per Million

List of Symbols and Abbreviations (Continued)

R - The fraction of reflected light

r - The total reflectance

S - The fraction of scattered light

SE - Secondary Electrons

SEM - Scanning Electron Microscopy

T - In-line Transmission

TD - Theoretical Density

TEM - Transmission Electron Microscopy

2θ - The angle between the detector and the source at XRD

UV - Ultraviolet

V - Vacancies

$V_{unit\ cell}$ - Volume of Unit Cell

v - Light velocity in a material

vol% - Volume Percent

WDS - Wavelength Dispersive Spectroscopy

wt.% - Weight Percent

XRD - X-Ray Diffraction

YAG - Yttrium Aluminum Garnet

1. Introduction

Aluminum oxynitride (γ-AlON) is a hard ceramic material in the AlN-Al_2O_3 system. Most of its properties are comparable with those of alumina, but its cubic spinel crystal structure allows processing it as a fully dense, polycrystalline, completely transparent material, if a proper sintering route is used. Its high hardness and good transmission properties make AlON a real candidate for advanced applications such as transparent armor and missile domes.

AlON can be synthesized by the reaction of Al_2O_3 with AlN in nitrogen or by the carbothermal reduction of Al_2O_3 and carbon mixtures. Pressureless sintering can be utilized to produce fully dense AlON. Its similar properties, as well as the conventional sintering methods, make it a potential alternative material to sapphire, which is very expensive because of being a single crystal.

A transparent ceramic must not contain any scattering centers. There are many kinds of scattering sources in the bulk, one of the most important of them being porosity. In other words, transparency can be achieved only when the material contains no porosity. One of the well-known ways to reduce porosity is by introducing sintering additives, which form a liquid phase at the grain boundaries. Raytheon developed manufacturing processes for transparent AlON, including yttrium and lanthanum additives. High temperatures and long times of the sintering processes were reported as essential conditions to obtain full transparency.

This research intends to investigate the influence of three sintering additives (Mg, Y, La) on the microstructure and transparency of AlON. Towards this goal, various compositions of single phase AlON were manufactured by reaction sintering of Al_2O_3+AlN powder mixtures. The effect of sintering parameters such as temperature and time were also studied. General guiding principles on improving transparency were deduced.

2. Literature Survey

2.1 Composition and Structure of AlON

The AlN-Al_2O_3 system contains three important materials: AlN, AlON and Al_2O_3. It was first reported in 1959 by Yamaguchi and Yanagida[1] that Al_2O_3 could be stabilized by nitrogen to form a spinel phase at elevated temperatures. In the 1960's and early 1970's more work was done[2-11] on crystal phases in the AlN-Al_2O_3 system. Long and Foster[2] found that a spinel type (γ) phase exists at about 76 mol% Al_2O_3 and a tetragonal (δ) phase appears at about 93 mol% Al_2O_3. The first phase diagram for the AlN-Al_2O_3 pseudo-binary system was reported in 1964 by Lejus[6], in which six phases were identified. Lejus observed that below 1600°C no reaction took place and that only above this temperature the γ-phase could be found. He found that the homogeneity region of this phase extends from 67 to 84 mol% Al_2O_3 at 1700°C and from 50 to 86 mol% Al_2O_3 at 2000°C.

The phase diagram has been modified by Gauckler and Petzow[12], who found that one of the phases is actually composed of two polytypes. The polytypes, which are on the AlN-rich part of the diagram, were further investigated by Sakai.[13,14] He found three more polytype phases and added them to the diagram. The polytypes are layered superstructures based on AlN with a large axis perpendicular to the layer. The high temperature part of the alumina-rich portion of the diagram was determined under flowing nitrogen by McCauley and Corbin in 1979.[15] In this region the compounds have basically defective spinel-type structures. They concluded that the γ-phase (AlON) is stable between 60 and 73 mol% Al_2O_3 for all temperatures between 1750°C and 2000°C. The AlON phase seemed to melt incongruently at about 2050°C. These results helped the authors to propose an updated phase diagram. In the same work it was shown that γ-AlON spinel can be sintered to nearly full density and exhibits visible light transparency.

The most recent phase diagram of the Al_2O_3-AlN pseudo-binary system for an atmosphere of 1 atm of nitrogen was published by McCauley and Corbin in 1983.[16] It is shown in Figure 2.1. In the new diagram some changes were introduced: the AlON

phase was determined to melt congruently, and the melting point was changed to 2165°C. Phase diagrams of the AlN-Al_2O_3 pseudo-binary system were also calculated from thermodynamic considerations.[17-20] This will not be discussed here, but it should be mentioned that the thermodynamic properties of AlON have not been accurately determined.

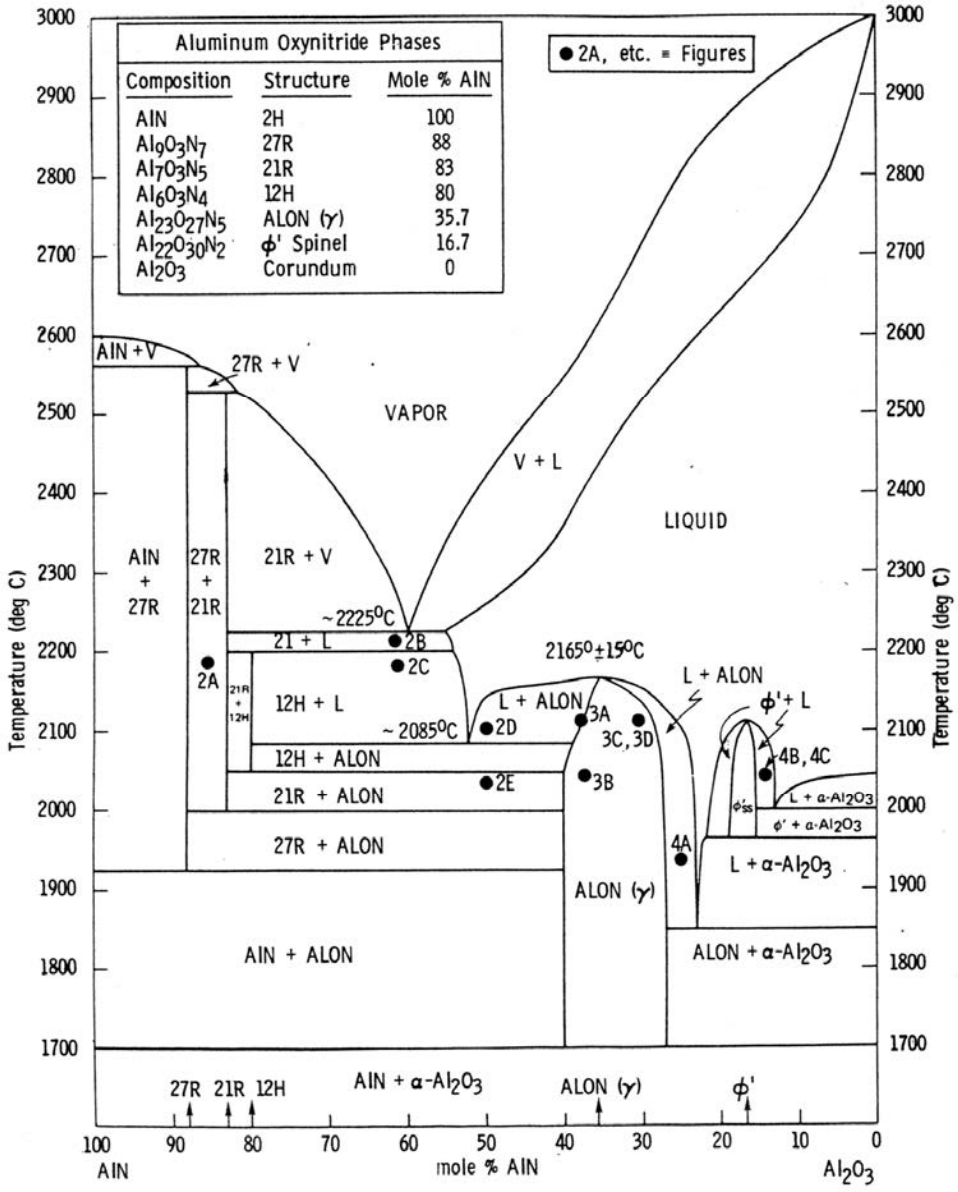

Figure 2.1. Phase diagram for the AlN-Al_2O_3 pseudo-binary system.[16]

Takebe *et al.*[21] suggested, like Lejus, that the AlON homogeneity region is a function of temperature. They found that it extends from 68 to 72 mol% Al_2O_3 at 1700°C and from 66 to 80 mol% Al_2O_3 at 1800°C. In a recent work by Tabary *et al.*[22], the widest homogeneity region was measured to be 64.5-76.5 mol% Al_2O_3.

Most of the authors agree that AlON is stable only above 1600°C. Lejus[6] and Gilles[7] reported that an AlON sample heated in a graphite crucible at 1400°C was converted into α-Al_2O_3 and AlN. Sappei *et al.*[23] made annealing experiments of AlON powder under nitrogen at about 1400°C and after 4 hours found that it was completely converted in α-Al_2O_3 and AlN. However, Irene, Silvestri and coworkers[24,25] observed the formation of thin AlON layers on silicon substrates at 900°C when gaseous precursors were used.

Even though the current research deals with γ-aluminum oxynitride (AlON), some attention should be given to the other phases in this system. The AlN-Al_2O_3 phase diagram contains at least 13 different phases with varying concentration ranges[26], which are listed in Table 2.1. As mentioned earlier, there are two main groups of phases which are separated by their crystallographic structures. The first one is aluminum nitride polytypes, which are based on the AlN wurtzite structure. These polytypes, in contradiction to SiC polytypes, differ in composition as well as the stacking sequence of a two dimensional layer (polytypoids) and the compositions given in Table 2.1 consider specific metal/nonmetal ratios which allow for charge neutrality. The second group is based on the spinel structure.

Table 2.1. Aluminum oxynitride phases observed in the AlN-Al_2O_3 pseudo-binary system.[26,27]

Notation	Mol% AlN	Fomula	Structure
2H	100	AlN	Polytype
32H	93.3	$Al_{16}O_3N_{14}$	Polytype
$2H^{\delta}$	~91	$Al_{12}O_3N_{10}$	Polytype
20H	88.9	$Al_{10}O_3N_8$	Polytype
27R	87.5	$Al_9O_3N_7$	Polytype
16H	85.7	$Al_8O_3N_6$	Polytype
21R	83.3	$Al_7O_3N_5$	Polytype
12H	80.0	$Al_6O_3N_4$	Polytype
γ-AlON	35.7	$Al_{23}O_{27}N_5$	Spinel
γ'-AlON	~21.0	$Al_{19.7}O_{29.5}N_{2.5}$	Spinel
ϕ'-AlON	16.7	$Al_{22}O_{30}N_2$	Spinel
δ-AlON	10	$Al_{19}O_{27}N$	Spinel
ϕ-AlON	7.1	$Al_{27}O_{39}N$	Monoclinic
α-Al_2O_3	0	Al_2O_3	Rhombohedral

From the early results of Yamaguchi and Yanagida[1] it was known that the crystal structure of AlON phase is spinel. Goursat and coworkers[28,29] determined it to be spinel-type with the space group $Fd\bar{3}m$, by neutron diffraction.

The spinel structure is based on an FCC close-packed anion sublattice in which fractions of the octahedral and tetrahedral sites are filled. Spinel compounds often have AB_2X_4 stoichiometry in which the cations A and B are divalent and trivalent, respectively ($AX \cdot B_2X_3$).[28] The number of atoms in a spinel unit cell is 56, since it consists of eight FCC anion subcells in a cubic array. Figure 2.2 shows a three dimensional depiction of the spinel structure.[30] The cations occupy one-half of the octahedral sites (16 out of 32) and one-eighth of the tetrahedral sites (8 out of 64). Thus, A^{2+} ions occupy the 8a sites, B^{3+} ions occupy the 16d sites and the X^{2-} anions occupy the 32e sites (the characters are the Wyckoff letters of the positions, the numbers stand for the multiplicity). This is the situation in a normal spinel, but in an inverse spinel the cations are exchanged. The B^{3+} ions occupy the 8a and half of the 16d sites and the A^{2+} ions occupy the rest of the 16d sites. In reality most spinels, whether they are normal or inverse, are disordered to some degree by exchange of the A^{2+} and B^{3+} cations.[30] One can find more details on the spinel structure in the review by Sickafus *et al.*[31]

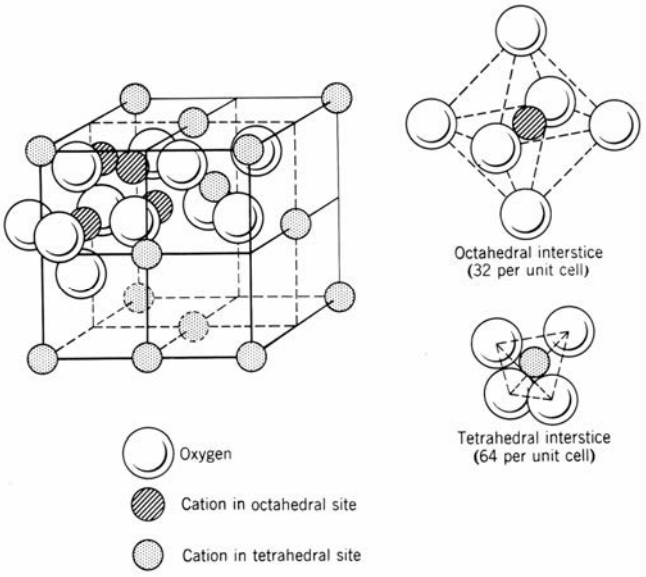

Figure 2.2. Schematic drawing of the spinel structure.[30]

For γ-AlON the anions X are both oxygen and nitrogen (randomly distributed on the 32e sites), while aluminum stands for both A and B cations. This means that one-third of the aluminum ions are Al^{2+} and the other two-thirds are Al^{3+}. Goursat *et al.*[28] verified this from neutron diffraction results on AlON. Since they found that trivalent ions (Al^{3+}) are located in the tetrahedral positions of the spinel structure, AlON can be considered as an inverse spinel. The γ-AlON spinel phase was found to be stable only when a disordered vacancy is in the spinel octahedral position. According to their results the vacancies are located on the octahedral sites (16d positions). This will be explained later in this chapter by the "constant anions" model of McCauley.

To summarize the description of the spinel structure, the atoms are located on the following positions:[32]

Equivalent positions – (0,0,0) , (0,½,½) , (½,0,½) , (½,½,0)

Al (A)- (0,0,0) , (¼,¼,¼)

Al (B) - (⅝,⅝,⅝) , (⅝,⅞,⅞) , (⅞,⅝,⅞) , (⅞,⅞,⅝)

O , N (X) - (u,u,u) , $(¼-u,¼-u,¼-u)$, $(u,\bar{u},\bar{u})$, $(¼-u,¼+u,¼+u)$,

$(\bar{u},u,\bar{u})$, $(¼+u,¼-u,¼+u)$, $(\bar{u},\bar{u},u)$, $(¼+u,¼+u,¼-u)$

If the anion parameter *u* is 0.375, the octahedra have a regular shape and the structure is called ideal. In the non-ideal structure, the anions are moved from the ideal positions along the <111> direction and the octahedra are trigonally distorted. Thus, in the ideal structure the anions are located on the following positions:

O , N (X) - (⅜,⅜,⅜) , (⅞,⅞,⅞) , (⅜,⅝,⅝) , (⅞,⅝,⅝) ,
(⅝,⅜,⅝) , (⅝,⅞,⅝) , (⅝,⅝,⅜) , (⅝,⅝,⅞)

The anion parameters which appear in the literature for γ-AlON indicate only a slight shift from the ideal structure. For example, Goursat *et al.*[28] found an anion parameter of 0.3816 for AlON with a lattice parameter of 7.9447Å. In a more recent work by Tabary and Servant[27], a very similar value was found for the anion parameter, 0.38176. This means that the anion FCC structure is slightly deformed. The spinel structure forces a rule of forbidden diffraction reflections, which is:

hkl: h+k=2n, h+l=2n, k+l=2n.

0kl: k+l=4n, k,l=2n.

hhl: h+l=2n.

h00: h=4n.

Some defect models for the composition of AlON were proposed by Adams *et al.*[4], Lejus *et al.*[6] and McCauley.[33] Most of the models use a "constant anion" lattice of oxygen and nitrogen where cation (aluminum) vacancies decrease as the nitrogen content increases. McCauley's constant anion model[33] is the most convenient to use because the total number of anions is 32, which is the number of anion sites in a spinel unit cell. This model describes the composition of AlON as:

$$Al_{(\frac{64+x}{3})}V_{Al,(\frac{8-x}{3})}O_{32-x}N_x$$

where V_{Al} are aluminum vacancies (or interstitials). In this model x=8 is an ideal spinel ($Al_{24}O_{24}N_8$), x<8 represents cation vacancies, and x>8 represents cation interstitials. Of particular interest are compositions which give integer numbers of aluminum cations and defects. Some of these appear in Table 2.2, with the corresponding mol% of AlN.

Table 2.2. Compositions of aluminum oxynitride by McCauley's constant anion model.[33]

x	Defect	Fomula	Mol% AlN
2	2 vacancies	$Al_{22}O_{30}N_2$	16.7
5	1 vacancy	$Al_{23}O_{27}N_5$	35.7
8	- (ideal)	$Al_{24}O_{24}N_8$	50.0
11	1 interstitial	$Al_{25}O_{21}N_{11}$	61.1

From the phase diagram (see Figure 2.1) we know that the composition with x=5 is the only one in the stability region of γ-AlON spinel. Thus, its stoichiometric formula is $Al_{23}O_{27}N_5$ and there is one aluminum vacancy in each unit cell, which agrees with the observation of Goursat *et al.*[28] mentioned above. The charge of the aluminum ions in the defected AlON is always 3+ and that of the nitrogen ions is 3-: $Al^{3+}{}_{23}O^{2-}{}_{27}N^{3-}{}_{5}$.

Dravid *et al.*[34] utilized TEM electron diffraction methods to determine the structure symmetry of γ-AlON spinel. They established the point group to be $m\bar{3}m$ and the space group was determined to be $Fd\bar{3}m$ (as that of ideal spinel). Most reports[27,28,35] showed (from structure refinement of neutron diffraction and X-ray diffraction data) that the vacancies are situated only on octahedral (16d) sites. The results of Dravid *et al.*[34], which indicated that the vacancies are not ordered and the symmetry of the structure is that of ideal spinel, are exceptional and considered to be incorrect. In any case, there is a wide agreement among AlON researchers that the constant anion model is the best one to describe AlON.

The calculations of Fang *et al.*[36] suggested that the O/N anions are partially ordered. Moreover, the most stable structure (with the lowest energy) of the defected AlON was found to have an Al vacancy at the octahedral site with six O nearest neighbors. However, in a nonstoichiometric AlON with less than 35.7 mol% AlN there is an increase in the number of vacancies and the defect mechanism may change.

The lattice parameter of stoichiometric AlON was found to be 7.950±0.005Å.[32] The dependence of the lattice parameter of AlON on composition was measured by various researchers. Some formulas for a linear relationship between the AlN content and the lattice parameter of AlON were found. For example, the results of Tabary and

Servant[27], which agree with those of Sakai[13], are that the lattice parameter increases from 7.923 to 7.950 Å with an increase of AlN content from 9.8 to 28.6 mol%. Willems *et al.*[37] found an increase from 7.932 to 7.953 Å with increasing AlN content from 19 to 34 mol%. For transparent AlON, the composition range was determined by Hartnett *et al.* to extend between 5.52-8.20 at.% nitrogen (or 23.7-32.9 mol% AlN)[38]. They found an equation which correlates the lattice constant with nitrogen content:

$$a\ (Å) = 7.9032 + 0.00625x \qquad (2.1)$$

where x is the atomic percent nitrogen content.

2.2 Synthesis and Processing

The synthesis of γ-aluminum oxynitride spinel (AlON) can be conducted by several methods, which appear in Table 2.3. There are two main synthesis processes which are widely discussed in the literature, and a few other secondary processes. The two main processes will be described thoroughly in this chapter, while the others will be mentioned briefly.

Processing of optically transparent AlON is more difficult than the synthesis of opaque single phase AlON, because the material must be fully dense, pure, and free of any secondary phases.

Table 2.3. Chemical reactions known to produce AlON phases.[26]

Synthesis equation	Required temperature (°C)	References
$Al_2O_{3\,(s)} + AlN_{(s)} \rightarrow AlON_{(s)}$	≥1650°C	2,6,14,15,21,39,40
$Al_2O_{3\,(s)} + C_{(s)} + N_{2\,(g)} \rightarrow AlON_{(s)} + CO_{(g)}$	≥1700°C	41-48
$Al_2O_{3\,(s)} + C_{(s)} + Air \rightarrow AlON_{(s)} + CO_{(g)}$	≥1700°C	1
$Al_2O_{3\,(s)} + Al_{(l)} + N_{2\,(g)} \rightarrow AlON_{(s)}$	>1500°C	18
$Al_2O_{3\,(s)} + Al_{(l)} + Air \rightarrow AlON_{(s)}$	>2045°C	8,10
$Al_2O_{3\,(s)} + NH_{3\,(g)} + H_{2\,(g)} \rightarrow AlON_{(s)} + H_2O$	≥1650°C	3
$Al_{(l)} + Air \rightarrow AlON_{(s)}$	~1500°C	9
$AlCl_{3\,(g)} + CO_{2\,(g)} + NH_{3\,(g)} + N_{2\,(g)} \rightarrow AlON_{(s)} + CO_{(g)} + N_{2\,(g)} + HCl_{(g)}$	900°C	24,25
$Al_2O_{3\,(s)} + BN_{(s)} + N_{2\,(g)} \rightarrow AlON_{(s)}$	≥1700°C	49

In general, two different approaches to solid state processing of AlON have been employed in order to reach high density and translucency:

1) Reaction sintering of Al_2O_3 and AlN mixtures.
2) Traditional sintering of pre-reacted AlON powders.

Both methods consist of some common characteristic stages:[50]

1) Mixing powders (usually ball milling in alcohol with alumina balls). Sintering additives can be introduced.
2) Reacting the powder mixture to form (mostly) AlON powder.
3) Ball milling of the above powder, possibly with a binder or appropriate sintering additives.
4) Drying the powder (or spray drying).
5) Filling a mold.
6) Pressing a blank to nearly net-shape and ~60% of the theoretical density (~20% oversize). This step can be followed by cold isostatic pressing of the blank.
7) Binder burnout (if used).
8) Sintering the blank at high temperature for an extended time (to allow atomic diffusion) to a 100% dense transparent ceramic with ~100-200 μm sized grains.
9) Grinding the AlON ceramic.
10) Final polishing to achieve high light transmission and minimal scattering.

2.2.1 Reaction Sintering

The reaction of a mixture of AlN and Al_2O_3 above 1650°C can be used to produce AlON powders, reaction sintered samples, and reaction hot-pressed specimens. The synthesis equation is the following (except for small deviations from stoichiometry):

$$9\ Al_2O_3 + 5\ AlN \rightarrow AlON \qquad (2.2)$$

The normal processing scheme includes ball-milling of a mixture of Al_2O_3 and AlN in alcohol, pressing, and sintering at high temperature under flowing nitrogen.

The effects of temperature and time on the reaction (2.2) were investigated by Bandyopadhyay *et al.*[51]. They reported that AlON formation (with 35.7 mol% AlN)

started between 1560°C to 1630°C, and above 1670°C the fraction of AlON increased dramatically. Single phase AlON appeared at ≥1800°C with a sintering time of 2.5 hrs (see Figure 2.3). The evolution of phase composition with reaction time during isothermal firing at 1820°C is shown in Figure 2.4, as calculated from the relative intensities of XRD reflections. It was found that at this temperature Al_2O_3 disappeared almost instantaneously, but the remaining AlN reacted with the formed AlON for longer times. In other words, oxygen-rich AlON forms first, followed by a subsequent slower reaction of this phase with AlN. It seems that AlON phase formation is controlled by the rate of nitrogen diffusion through the AlON lattice.

The dependence of the lattice parameter of AlON on the Al_2O_3 content was measured for samples fired at 1850°C and is presented in Figure 2.5. There is an increase in the lattice parameter as more nitrogen is introduced.

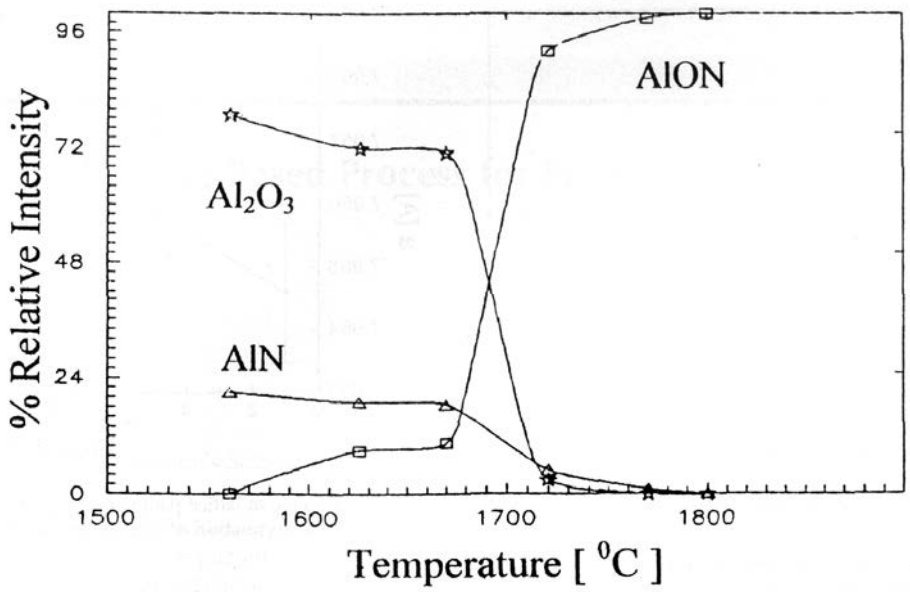

Figure 2.3. Effect of reaction temperature on Al_2O_3, AlN, and AlON volume-fraction (firing time of 2.5 hrs), expressed by XRD peak intensity ratios.[51]

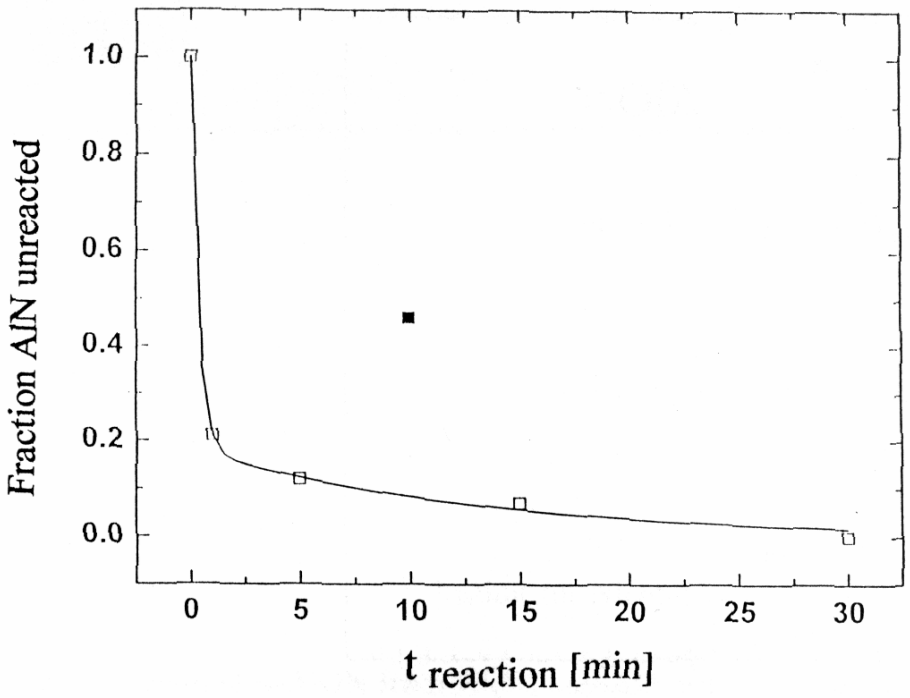

Figure 2.4. Effect of reaction time on unreacted AlN fraction (firing temperature of: □ 1820°C , ■ 1750°C).[51]

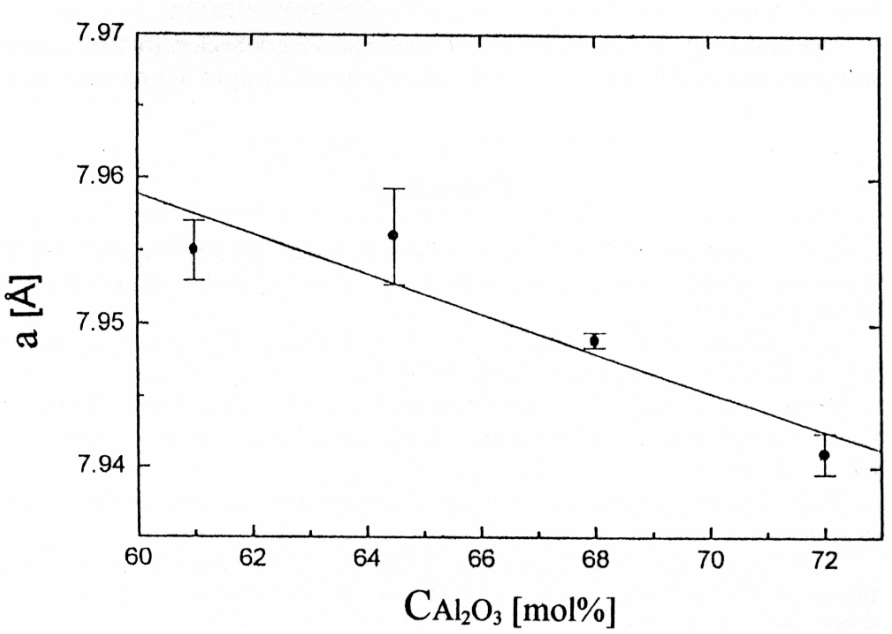

Figure 2.5. Dependence of lattice parameter of AlON on the concentration of starting Al_2O_3.[51]

Several different furnaces were used by Willems *et al.*[17] in order to sinter AlON. In those with graphite heating elements, the outer surface tended to be composed of some phase mixture of AlN and AlON. The same result was achieved when graphite crucibles were used for the sintering experiments. Using a powder bed consisting of AlN mixed with Al_2O_3 and BN decreased the amount of AlN on the surface. In the furnaces where heating elements were outside of an alumina tube, the outer surface consisted of AlON and alumina. It is clear that the presence of carbon inside the furnace cause the reduction of alumina into aluminum nitride (see section 2.2.2), which can remain as a second phase if the reaction does not proceed to its end.

The influence of nitrogen pressure on the reaction was also investigated by Willems *et al.*[17] High pressures, up to 80 bar, were used and the end density was lower than in the case of normal pressures (1-3 bar). This was attributed to a kinetically more rapid formation of AlN, which increased the amount of AlN in the product, while AlN has a lower density compared to AlON.

2.2.2 Carbothermal Nitridation of Alumina

Reaction of Al_2O_3 and carbon in nitrogen atmosphere above 1700°C results in the formation of AlON, according to:

$$23\ Al_2O_3 + 15\ C + 5\ N_{2\,(g)} \rightarrow 2\ AlON + 15\ CO_{(g)} \qquad (2.3)$$

This reaction is usually called carbothermal reduction (or nitridation) of alumina. Carbothermal nitridation of alumina has become a well established way to synthesize AlON since Yamaguchi and Yanagida[1] first reported it. Many investigations have been performed on this preparation route.[41-46]

In general, alumina and carbon black fine powders are ball milled, usually in alcohol, and dried. The powder mixture can react at a temperature to give AlON powder which is then pressed and sintered. It can also be pressed and reaction sintered to give dense AlON parts.

Ish-Shalom[42] found that AlON formed as an intermediate compound in a certain range of compositions. He reacted α-alumina and carbon powder mixtures at various temperatures for different durations. The relative amount of AlON in the products went through a maximum at a certain annealing time, which decreased with increasing annealing temperature. This observation was repeated by Yawei *et al.*[44], but was not reported in any other known research, and annealing times to sinter fully dense single phase AlON were sometimes very long, even up to a couple of days.

Zheng and Forslund[43] established the conditions needed in order to produce the AlON phase in terms of different annealing temperatures and times, atmosphere gases and pressures, and crucible or powder bed materials. They suggested that the synthesis should be performed in two steps, the first at 1600°C and the second at ~1800°C, to obtain single phase AlON powder. High nitrogen pressure and crucibles with alumina covers were found to effectively lower the nitridation rate, which can help to avoid deviating from the desirable composition. Additionally, adding CO to the reaction gas enhanced AlON formation, at the expense of AlN.

Some different alumina sources for the carbothermal reduction process were used by Yawei *et al.*[46], such as $Al(OH)_3$ or dried gel. It was found that all alumina sources used gave faster reaction rates than α-Al_2O_3. This is because the other sources transform into γ-Al_2O_3 while heating, and this has an FCC structure (such as that of AlON) and a higher reactivity than α-Al_2O_3.

Transparent AlON has been developed by the Raytheon Company since the 1980's, until it was transferred to the Surmet Company in 2002. The first publication on their study was that of McCauley and Corbin,[15,40] where they reaction sintered an isostatically pressed mixture of γ-Al_2O_3 and AlN at 1950-2100°C into a thin translucent disk of AlON. Later, Raytheon patented its transparent AlON manufacturing method based on carbothermal reduction of alumina.[47,48] Using various sintering additives (see section 2.4.2), they produced transparent AlON samples. Another patent was filed, which describes Raytheon's reaction sintering process to produce translucent AlON.[52] These patents hint that the procedure of reacting γ-Al_2O_3 and AlN powder to form AlON powder and then sintering it, is the leading method of manufacturing transparent AlON. According to Gentilman *et al.*, the initial powder composition was 35.7 mol%, but the high temperature firing process was believed to change the ratio between the elements.[50] In recent years no clues have been found in the open literature on the updated method utilized in the commercial manufacture of transparent AlON parts.

2.2.3 Other Synthesis Processes

AlON phase has been formed by several other high temperature processes, which appear in Table 2.3. Like carbon in reaction (2.3), aluminum and ammonia have also been used as reducing agents. Al_2O_3+Al mixtures reacted in air,[8] and Al_2O_3+ammonia reacted in nitrogen gas.[3] Aluminum liquid can be reacted in air to form an aluminum oxynitride phase.[9] The lowest temperature process reported in which AlON was formed as thin layers, involved a vapor phase reaction of $AlCl_3$ gas at 900°C.[24,25]

2.2.4 Hot-Pressing of AlON

Although pressureless sintering is the main method used to prepare AlON, some works have been done on hot-pressing. This process can be conducted either on pre-synthesized AlON powders or on Al_2O_3 and AlN mixtures (reaction hot-pressing). It is reasonable to think that hot-pressing should facilitate AlON manufacturing; however apparently this is not the case.

Reactive hot-pressing of AlN and α-Al_2O_3 powder mixtures performed by Turpin-Launay *et al.*[49] resulted in an almost pure single phase γ-AlON. Experiments were conducted at 1850°C, soaking time of 30 minutes, with a uniaxial pressure of 32.5 MPa under nitrogen. It should be noted that the raw powders were not pure: Al_2O_3 with 0.1 wt.% MgO and AlN with <0.15 wt.% Fe.

A similar process was used by Wang *et al.*[19] to produce ~98% dense single phase AlON. They added 3.6 mole% Al to the powder mixture and hot-pressed it at 1800°C for 3 hrs in N_2 gas at 25 MPa.

Hot pressing of translucent AlON was demonstrated by Martin and Calès.[53] After synthesizing the AlON powder by carbothermal nitridation of alumina, they hot-pressed it at 1700-1750°C under 50 MPa and achieved 98% theoretical density and a relatively small mean grain size (10 μm). Then the samples were annealed at 1920-1940°C for 10-20 hrs to promote grain growth. The highest optical transmission was obtained by the process at the highest temperature and longest sintering time, which yielded almost full density and a mean grain size of 200 μm. This sample exhibited 25% visible light transmission and a maximum of 55% transmission at 4 μm. The only mention of transparent AlON prepared by hot pressing was of Lefort *et al.*[54], but no process details were given.

2.2.5 Microwave Sintering of AlON

Fully dense AlON with high light transmission was fabricated by microwave sintering by Cheng *et al.*[55-57] In this process, the processing materials absorb microwave energy and convert it to heat within the sample volume, and therefore the heating is very rapid. Characteristically, the reaction and sintering rate in this process is higher than in the conventional sintering process. AlON was prepared from mixtures of α-Al_2O_3 and AlN powders with 0.5 wt.% Y_2O_3 additive (which was added in the form of yttrium nitrate hexahydrate). The powders with 3 wt.% of binder were ball milled for 24 hrs, uniaxially compacted into pellets and then isostatically pressed. Samples that were sintered with a heating rate of ~100 °C/min up to 1800°C and a soaking time of 60 minutes at this temperature showed high light transmission. The grain size of these samples was around 40-50 μm. This demonstrates that the microwave sintering process offers a lower sintering temperature and much shorter dwell times, in comparison to conventional sintering process. It should be mentioned that the ceramic pellets sintered by this process were relatively small (diameter of 12.7 mm) and that a maximum light transmittance achieved in the visible region was ~45% through a 0.6 mm thick sample, so the samples were not fully transparent.

2.2.6 AlON Composites[23,58]

In the literature there are some reports on the fabrication of alumina-AlON composites.[23,58] Their properties are different than those of pure AlON, and they are (obviously) not transparent.

Alumina-AlON (ALUMINALON) composites with ~1 wt.% N, based on an alumina matrix with a dispersion of γ-AlON grains, were prepared by Sappei *et al.*[23] They formed AlON on grain surfaces by reacting ammonia with γ-Al_2O_3 at about 1100°C. The composite powders were hot-pressed under nitrogen to almost full density and contained about 20 vol% of γ-AlON. Pure single phase fully dense AlON was reported to be fabricated by pressureless sintering of such a composite powder at 1700°C under neutral gas.[23]

Al_2O_3-AlON composites were also prepared via reaction bonding of Al_2O_3+Al mixtures by Cai *et al.*[58] In other study Launay *et al.*[59] reaction sintered Al_2O_3+AlN mixtures (both via pressureless sintering and via hot-pressing) to form ALUMINALON.

2.3 Influence of Additives

In order to achieve full transparency of a polycrystalline ceramic, one has to prevent any residual porosity in the sintered material. The main role of the additives is to help to eliminate the pores during the sintering process. The mechanisms by which the additives operate were investigated over the years, but are not fully understood.

Studies have been done on the influence of various additives in order to sinter translucent alumina. They are relevant to our discussion because of the similarities between alumina and AlON and the influences of additives on light transmission in both materials.

2.3.1 Additives to Translucent Alumina

There are a number of early studies on the preparation of translucent alumina by additions of Y_2O_3, MgO and La_2O_3. Coble[60] (General Electric Company) reported in an early patent that the addition of 0.06-0.5 wt.% of MgO into the alumina powder resulted in relatively high in-line transmission of the sintered bodies. The goal was to prevent excessive grain growth during sintering, which may cause undesired grain boundary cracking and pore trapping within the grains. The magnesia addition was believed to limit grain growth by pinning the grain boundaries and preventing them from sweeping past pores, and thus trapping the pores within the growing grains. However, excess MgO can result in the formation of spinel ($MgAl_2O_4$) as a second phase, which increases light scattering within the material because of the different refractive indices of alumina and spinel. Thus, there is an optimum range of magnesia addition percentages for the best optical properties. Coble reported that the maximum transparency in the infrared (IR) range occurs when 0.1 wt.% MgO is added. For

visible wavelengths 0.06 wt.% MgO or less is preferred. Indeed, transparent alumina (Lucalox) of General Electric Co. was reported by Grimm *et al.*[61] to contain 0.2 wt.% MgO.

Burke[62-63] proposed an explanation for the role of MgO in Lucalox, using the term of discontinuous grain growth. This process occurs when some grain boundaries are more mobile than others, because of an inhomogeneous distribution of pinning pores. Consequently, those grain boundaries move rapidly to absorb a few neighboring small grains and create some relatively large grains. This happens by bending of the boundaries around the array of small grains and migration over pores that earlier prevented the movement of other (less mobile) boundaries. Thus, pores are entrapped (occluded) inside the growing grains, where they appear to be stable.

Discontinuous grain growth requires highly mobile grain boundaries. Continuous grain growth occurs when the boundary mobility is low, and its rate is limited by the rate of disappearance of boundary pinning pores. In this case, the boundary can only move slowly, waiting for the disappearance of some pores to let it move slightly (until it encounters more pores). These pores are in turn removed by diffusion. It was found that small amounts of MgO additions only inhibit discontinuous grain growth, but do not prevent continuous grain growth from occurring. The pores in the pore free material were thus eliminated when the grain size was small and significant grain growth occurred later.

Burke[62-63] suggested that MgO reduces grain boundary mobility and prevents pore-grain boundary separation in alumina by poisoning grain boundary solution and growth sites. He assumed that grain growth occurs by a mechanism similar to crystal growth from a liquid: there is diffusion of atoms from a consumed grain through the grain boundary to a suitable attachment point in the growing grain. The "poison" atoms at grain boundary kink sites can impede addition or subtraction of atoms to or from kinks and thus reduce boundary mobility. Burke claimed that magnesium ions are specifically able to poison growth and/or dissolution sites.

Peelan[64] found that very small amounts of MgO, below the solubility limit, were effective in aiding the sintering of alumina. As demonstrated in Figure 2.6, both the

density and grain size were observed to pass through a maximum around the solubility limit of MgO in Al_2O_3 (~300 ppm).

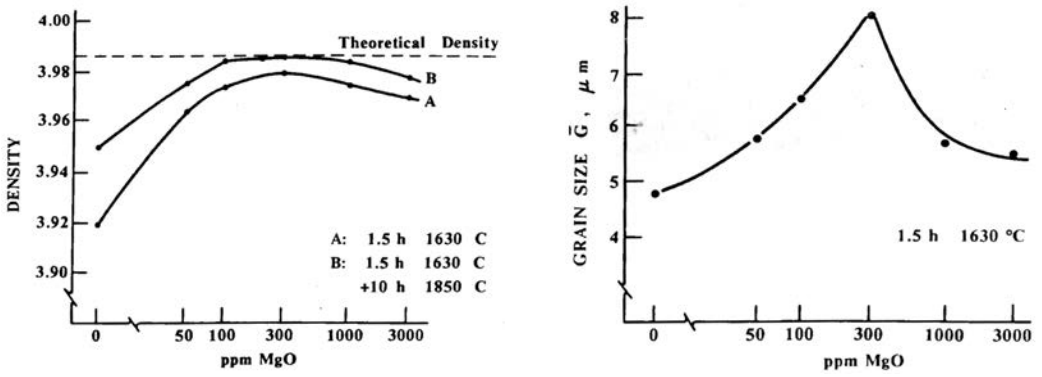

(a) (b)

Figure 2.6. a) Final density and b) final grain size, as a function of MgO concentration in sintered alumina samples.[64]

A few combinations of additives of up to 0.08 wt.% MgO, 0.05 wt.% Y_2O_3 and 0.04 wt.% ZrO_2 were used by Wei *et al.*[65] as sintering aids for high translucency alumina. Kaneno *et al.*[66] preferred to use (for the same goal) between 0.01-0.1 wt.% of MgO, La_2O_3 and Y_2O_3, simultaneously.

Krell *et al.*[67] reported that 0.03 wt.% MgO was the optimal quantity of addition for the ultrahigh purity alumina powder they used. They found that this small amount of additive results in a finer grain size and less residual porosity than observed in undoped microstructures. However, the addition had no influence on strength. Krell *et al.* discussed two other dopants. Y_2O_3 was mentioned as a grain growth inhibitor, like MgO. Doping with 0.2 wt.% ZrO_2 increased light transmission, although it is apparently less effective in pinning the alumina boundaries because ZrO_2 particles were observed within grains of the sintered material. Using this dopant they could sinter at higher temperatures without excessive grain growth.

Use of 0.02-0.6 wt.% MgO additive as a grain growth inhibitor was also reported by Aurial *et al.*[68] According to their patent, other metal oxide additives, such as La_2O_3, Y_2O_3 and BaO play the same role during sintering.

Kobayashi *et al.*[69] have another explanation for the use of other additives. They manufactured translucent alumina with high visible light transmission by mixing the alumina powders with 0.05-0.5 wt.% Y_2O_3, 0.05-0.5 wt.% La_2O_3 and 0.01-0.1 wt.% MgO additions. Yttria was said to accelerate the grain growth of the alumina crystals at relatively low temperatures (1200-1450°C). More than 0.5 wt.% Y_2O_3 caused excessive acceleration of grain growth and a non-uniform final grain size. Magnesia was supposed to spheroidize the alumina particles, but only at sintering temperatures less than 1700°C, otherwise the high vapor pressure accelerates the evaporation of MgO from the surface which results in exaggerated grain growth and reduced optical transmission. Evaporation is the reason why they recommended adding less than 0.1 wt.% MgO. As mentioned before, MgO reacts with Al_2O_3 to produce spinel near the grain boundaries, which inhibits grain growth. Lanthanum oxide stabilizes the spinel, and therefore controls the grain growth up to temperatures higher than 1700^0C. Furthermore, La_2O_3 and Y_2O_3 additions make the refractive index of grain boundary products, such as $MgAl_2O_4$, close to that of alumina and thus decrease optical scattering.

Kobayashi *et al.*[69] reported that the highest light transmission was achieved by making use of 0.05 wt.% MgO, 0.25 wt.% Y_2O_3 and 0.25 wt.% La_2O_3 additives. Figure 2.7 shows their schematic phase diagram illustrating the composition range of the highest transmission. It is important to mention that the transmission values are not in-line transmission but probably include scattered light, because they reached the unreasonable optical transmission of 96%.

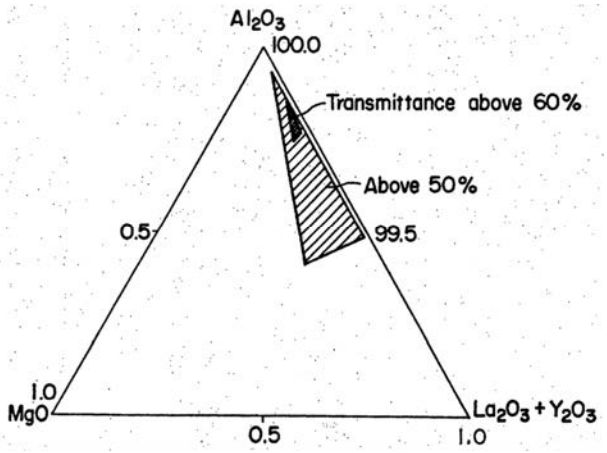

Figure 2.7. Schematic phase diagram showing the composition range of the highest light transmission of alumina with MgO, Y_2O_3 and La_2O_3 additives.[69]

2.3.2 Additives to Transparent AlON

Additions of Y_2O_3, La_2O_3 and boron were investigated in some works done by Raytheon. Hartnett *et al.*[47,48] prepared AlON powder by reacting γ-Al_2O_3 with carbon black under N_2 at temperatures in the range of 1550-1850°C. Gentilman *et al.*[52] prepared yttrium and boron doped AlON powder by reaction-calcining α-Al_2O_3 and AlN mixtures at 1600-1750°C. It was reported that additives may be added by one of a number of different ways:

1. Mixing during ball milling of the AlON powder.
2. Addition of metals (Y, La, B) or (preferably) oxides or nitrides (Y_2O_3, La_2O_3, BN).
3. Placing doping additions in the sintering chamber near the green body.
4. Dopants are present in the container material.

The green body was sintered at temperatures higher than 1900°C. The minimal amount of Y_2O_3 additive found to allow light transmittance was 0.02 wt.%. The preferred combination of sintering additives was found to be 0.08 wt.% Y_2O_3 and 0.02 wt.% La_2O_3. The sample which contained these additives and was sintered at 1930°C for 24 hrs yielded in-line transmission of 80% at a thickness of 1.45 mm.

The suggested explanation for the dopant effect was that at sintering temperatures there is a high vapor pressure of Al_xO_y gas species which react with nearby BN

additives to produce B_2O_3 gas and/or $AlBO_2$ gas and AlN solid. These vapors react with AlON to produce a liquid phase at grain boundaries, which enhances the early sintering stages. Additionally, B_2O_3 reacts with yttrium to produce YBO_2 gas, which transports to the AlON and dopes it with boron and yttrium. This can aid the final sintering stages by changing the solubility limit or precipitating second phase particles in order to pin grain boundaries, and thus prevent excessive grain growth which can trap pores within the grains.

Too high a content of additives can be deleterious because it may cause the introduction of a second phase during the liquid phase stage of the sintering process. This minor phase envelopes the AlON grains and remains at the grain boundaries. This is what happened when a relatively high content of Y_2O_3 additive was used by Martin and Calès[53]. They investigated Y_2O_3 doping of AlON sintered at 1900°C and showed that it promoted the densification, microstructural homogeneity, and the localization of pores at grain boundaries. They found that 0.5 wt.% was the ideal amount of Y_2O_3 dopant to achieve these effects, which resulted in translucency. However, when they annealed this doped AlON at 1950°C for 20 hrs, an Y_2O_3-rich phase segregated at the grain boundaries and grain growth became heterogeneous. This of course destroyed the samples' translucency.

A higher amount of Y_2O_3 additive (up to 1.66 wt.%) was used by Chen *et al.*[39]. Comparing samples sintered at 1800°C for 6 hrs with this additive or without it, they found that increasing the additive content reduced porosity because the liquid phase sintering eliminates porosity effectively. However, a second phase of $3Y_2O_3 \cdot 5Al_2O_3$ (YAG) appeared at the grain boundaries. Consequently, none of the examples were translucent, but the additive seemed to make the samples be "slightly translucent", perhaps because of the reduced porosity. They saw evidence for liquid phase formation at a temperature as low as 1600°C, as opposed to the results of Martin and Calès[53] (with less additive). Most of the densification was achieved by solid state sintering between 1300°C to 1600°C.

An even higher Y_2O_3 content, between 0-7 wt.%, was used by Takebe *et al.*[21] All the doped samples had a second phase (YAG). However, this still allowed the 1 wt.%

Y_2O_3 sample to be slightly translucent. Its density was close to 100%, much better than the 85% achieved without any additive (sintered at 1800°C).

It was found by Willems[32] that small additions of MgO (0.3-1 wt.%) result in higher densities. However, doping with at least 0.3 wt.% Y_2O_3 had the opposite effect. Furthermore, 1-3 wt.% Y_2O_3 addition resulted, as mentioned before, in YAG ($Y_3Al_5O_{12}$) as a second phase.

As a conclusion, it can be said that the sintering aids form a transient liquid phase which promotes liquid phase sintering during the early stages of densification.[26] The components of the liquid phase should be soluble in AlON in order to prevent formation of secondary phases in grain boundaries and therefore a transparent material.

2.4 Properties

The first report on the properties of dense, single phase AlON, was in the beginning of the 1980's by McCauley and Corbin.[15,16,40] They reported relatively high hardness, elastic modulus and flexural strength (also at elevated temperatures), which were similar to the properties of alumina. This strengthened the impression that AlON may be used for advanced applications where a combination of optical transparency and high mechanical properties is needed. As work proceeded more results on property measurements were published: mechanical properties[40,46,54,70-76], thermal properties[54,70,73,75], dielectric properties[40,73] and optical properties[38,73,75,77].

The typical microstructure reported for AlON contains relatively large grains (80-250 μm, depending on processing conditions) with occluded pores and/or pores at grain boundaries.[38,74,78] The grains are typically uniform in size.

The properties of AlON which appear in the literature are scattered because of composition and processing differences. Therefore, the properties listed in Table 2.4 are representative and not necessarily exact. Properties were taken mainly from the

recent review of McCauley.[79] If known, properties of transparent AlON materials, mainly from Raytheon, are noted.

Table 2.4. Representative properties of AlON compared with other similar ceramics: α-Al_2O_3, AlN and transparent spinel ($MgAl_2O_4$).[26]

Property	**AlON**	**α-Al_2O_3**	**AlN**	**$MgAl_2O_4$**[74]
Density (g/cm^3)	3.71	3.98	3.26	3.58
Hardness (GPa)	13.8	15	12	12.1
Young's Modulus (GPa)	320	415	310	275
Flexural Strength (MPa)	300	380	400	185
Fracture Toughness ($MPa \cdot m^{1/2}$)	2.4-2.9	3.5	3.0-4.0	1.7
Bulk Modulus (GPa)	210	255	200	-
Shear Modulus (GPa)	125	150-170	130	110
Poisson's Ratio	0.25	0.23	0.23-0.24	0.26
Hugoniot Elastic Limit (GPa)	10.5-10.9	5-14	7.0-9.4	-
Longitudinal Sound Velocity (km/s)	10.2	9-11	10.7	-
Melting Temperature (°C)	2165	2050	Sublimes	2135
Coefficient of thermal expansion (K^{-1}) (25-1000^0C)	$7.6 \cdot 10^{-6}$	$8.1 \cdot 10^{-6}$	$5.6 \cdot 10^{-6}$	$8.0 \cdot 10^{-6}$
Thermal Conductivity (W/m°C)	10	33	180-220	15
Refractive Index (at 0.55 μm)	1.785	1.768	2.23	1.71
UV Cut Off (μm)	0.25	0.19	-	0.25
IR Cut Off (μm)	5.2	6	6.3	5.7
Electrical Band Gap (eV)	6.2	9.9	6	-
Dielectric Constant (1 MHz)	8.56	9.9	8.9	-
Dielectric Constant (7 GHz)	8.6	9.9	8.2	-
Dielectric Loss (1 MHz)	0.0005	0.002	0.001	-
Dielectric Loss (7 GHz)	0.0002	-	0.002	-

2.4.1 Mechanical Properties

As can be seen in Table 2.4, the representative mechanical properties of AlON are quite similar to those of Al_2O_3 and AlN. Mechanical properties were found to change only slightly up to 1100°C.[54] However, this temperature seems to be the upper limit for AlON, because oxidation then impairs the transparency, creates microcracks and significantly degrades the bending strength.

Dynamic experiments made with transparent AlON showed that it is substantially stronger than 99.5% polycrystalline alumina, but more brittle.[80,81] Its very high σ_{HEL} was found to be more similar to that of sapphire than to polycrystalline alumina. Therefore, AlON can also be appropriate for applications were dynamic loads are involved.

2.4.2 Optical Properties

The optical properties of AlON are summarized in several papers in the literature.[38,50,73,74] Here only the most important relevant optical properties of AlON will be discussed. An in-line transmittance curve of a 2.6 mm thick AlON sample fabricated by Raytheon is shown in Figure 2.8. It should be noticed that this curve is from 1989 and is not the state of the art, but the most recent one published. Of course, the transmittance depends upon the sample thickness as given by equation (2.9).

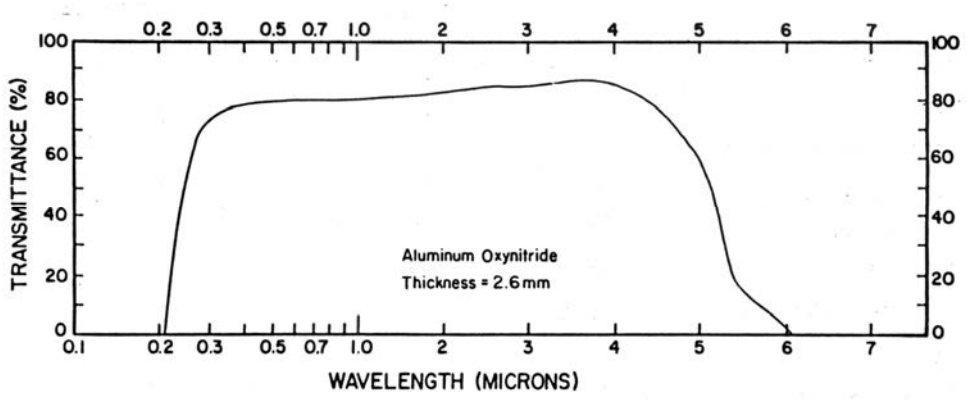

Figure 2.8. In-line transmittance of AlON in UV, visible and IR wavelengths.[50]

The practicable transmission range of AlON extends from ~0.25 μm in the ultraviolet (UV) through the visible to ~5.2 μm in the IR. It is quite similar to the transmission range of sapphire and $MgAl_2O_4$. Thus, AlON may be used as a substitute for sapphire, which is a single crystal that is produced by expensive crystal growth techniques.

A relatively large AlON window fabricated by Raytheon in 1986 is shown in Figure 2.9. In the meantime larger (12"x12") windows were manufactured by Raytheon.[82]

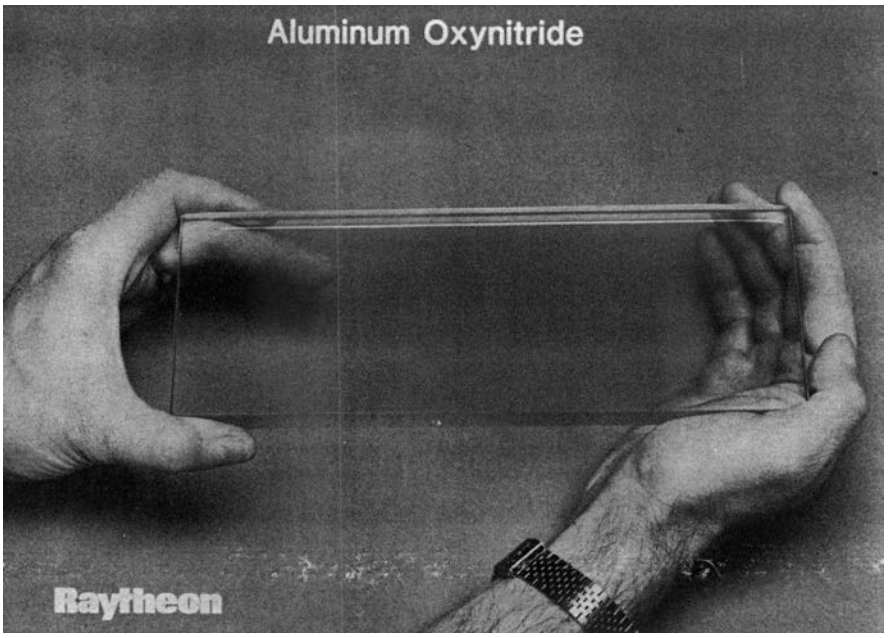

Figure 2.9. AlON window fabricated by Raytheon in 1986.[50]

2.4.3 Oxidation Resistance

The AlON phase is thermodynamically unstable below ~1640°C. AlON has good oxidation resistance in air up to elevated temperatures, due to a protective oxide or oxynitride layer which forms on the surface. Nevertheless, when heated to temperatures above ~1200°C even a very low oxygen content in the nitrogen gas may cause decomposition into Al_2O_3 and AlN.[18] Figure 2.10 depicts the oxidation behavior of AlON at various temperatures as a function of time in air.

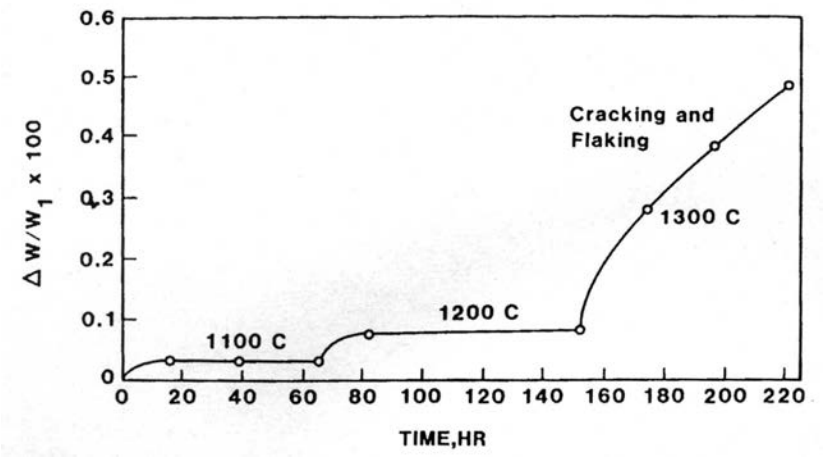

Figure 2.10. Oxidation of AlON at various temperatures as a function of time in air.[73]

When graphite is present, the result is a complete conversion into Al_2O_3. This occurs because the decomposition of AlON is faster than the reduction of Al_2O_3 by graphite. However, after heating an AlON sample at 1400°C for 100 hrs in a vacuum furnace under a pressure of 10^{-9} bar, AlON still remained the main phase, along with some alumina on the surface.[17]

Significant oxidation of AlON powder in air was found to occur above 1000°C.[83,84] When heated in Ar, N_2 or N_2+10%CO atmospheres at 1330°C<T<1630°C, the powder underwent measurable decomposition, accompanied by compositional change in AlON towards AlN.

It has been shown by Willems *et al.*[85] that MgO can stabilize AlON below the lowest reaction temperature (~1640°C). For instance, about 25 mol% of MgO has to be added to AlON in order to stabilize it at 1400°C. The resultant material is an intermediate phase between AlON and $MgAl_2O_4$ spinels.

2.4.4 Chemical Stability

AlON has excellent chemical stability. According to Goursat *et al.*[29], its resistance to acids, bases and water is very good and it can only be dissolved with a molten

Li_2CO_3/B_2O_3 mixture. For these reasons, AlON is appropriate to applications in the metallurgical industry.

2.5 Transparency

Transparent materials allow objects on the other side be distinctly seen. Translucent materials are different in a sense that they allow light to pass, but are not clear (in other words, diffuse). Polished translucent plates can provide a clear image of a print when placed immediately on the printed matter, but the image disappears when the plates are brought into a more distant position because of light scattering. Figure 2.11 illustrates the difference between transparent and translucent materials.

Figure 2.11. Illustration of the light transmission of (a) translucent material with a high diffuse transmission and a low in-line transmission and (b) transparent material with a low diffuse transmission and a high in-line transmission.[86]

In order to better understand the factors affecting the transparency of materials, the manner by which light interacts with matter will be reviewed. Afterwards, the influence of microstructural features on transparency will be described.

2.5.1 Light-Matter Interaction[77,87]

There are several ways by which light can interact with a transparent material:

a. Reflection of the incident light at any surface (R).

b. Scattering of the light entering the material (S).

c. Absorption of the light inside the material bulk (A).

The interactions are related by the following expression:

$$I_0 = I_R + I_S + I_A + I_T \qquad (2.4)$$

where I is the light intensity and the indices indicate the various interactions, and I_T is the intensity of the transmitted light, which leaves the material through the opposite side. Figure 2.12 depicts a summarizing scheme of the various interactions. The light beam bending at interfaces is due to refraction, as explained hereinafter.

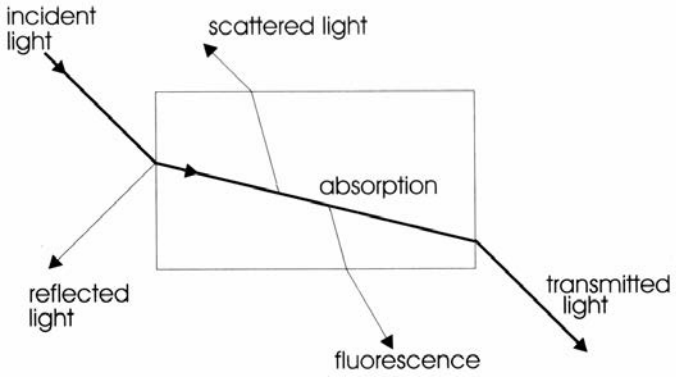

Figure 2.12. The interaction of light with a transparent material.[87]

When light passes from one medium to another, it changes its velocity and direction, which is called refraction. The refractive index, n, of a material is defined as the ratio between the velocity of light in vacuum, c, and the velocity of light in the material:

$$n = \frac{c}{\mathrm{v}} \qquad (2.5)$$

The refractive index depends on wavelength and crystallographic direction. We will narrow the discussion to materials with cubic symmetry, for which n does not significantly change with crystal direction.

A light beam changes its direction when refracting, according to Snell's law:

$$n_1 \sin\theta_1 = n_2 \sin\theta_2 \qquad (2.6)$$

where θ_1 is the incidence angle, θ_2 is the refraction angle, n_1 and n_2 are the refractive indices of the two media. If some of the absorbed light is re-emitted (most probably at a lower energy), it is called fluorescence. In our discussion we will ignore this phenomenon.

2.5.1.1 Reflection

Reflection is often dominated by surface roughness, which makes the material diffusive or specular. The cause for specular reflection is a difference in refractive indices. The fraction of reflected light, R, is determined by Fresnel's formula:

$$R = \frac{(n_2 - n_1)^2}{(n_2 + n_1)^2}. \qquad (2.7)$$

Air has n≈1 (a reasonable approximation). For γ-AlON spinel n=1.785 at a wavelength of 0.55 μm[79] and thus R=0.08 for one surface reflection from AlON in air. The total reflectance arises from light reflected from both entry and exit surfaces plus multiple internal reflections:[77]

$$r = \frac{2R}{1+R}. \qquad (2.8)$$

For an AlON window in air r=0.15. In other words, the maximal in-line light transmission through perfectly transparent AlON is 85% (without any anti-reflective coating).

The source for diffusive reflection is surface roughness. Light that meets a rough surface is reflected from it to different directions. These reflections can be reduced by a high degree of polishing.

2.5.1.2 Absorption

AlON is an electrical insulator. According to band theory, insulators have an empty conduction band and the valence band is completely filled by electrons. Moreover, the band gap is quite large (6.2 eV for AlON). This means that light photons are not energetic enough to excite an electron from the valence band to the conduction band and so are not absorbed. Therefore, the material will appear transparent to these wavelengths. The band gap determines the UV-cutoff of the material, which is 0.2 μm.

Impurities and defects can destroy the material transparency by creation of new energy levels within the band gap, which allow the absorption of photons inside the transparency wavelength range. These impurities, which might be for example small metal particles or ions, are known as absorption centers. When absorption centers are distributed uniformly throughout the bulk the amount of light absorbed in a plate is given by Lambert's law:

$$I = I_0 \exp(-\alpha_a l) \qquad (2.9)$$

where I is the intensity leaving the plate, I_0 is the incident intensity, l is the plate thickness and α_a is the linear absorption coefficient. The degree of absorption varies significantly with the light wavelength.

2.5.1.3 Scattering

Scattering can take place at different kinds of inhomogeneities in the bulk, called scattering centers, such as grain boundaries, inclusions, lattice defects or voids. Scattering centers in a transparent material cause the light intensity in the incident direction to gradually decrease while advancing through the medium. Instead, light is scattered into other directions. Scatter can occur on both surfaces of a window and inside the bulk.

The reduction in the intensity of a light beam which has traversed a medium containing scattering centers can be written as

$$I = I_0 \exp(-\alpha_s l) \qquad (2.10)$$

where I_0 is the incident beam intensity, I the intensity after traveling a distance l in the material and α_s is an experimentally determined linear scattering coefficient, measured in m^{-1}. The form of this equation is identical to that of Lambert's law for absorption, but here scattering centers are the reason for intensity reduction.

The effect of different plate thicknesses l_1 and l_2 on the real in-line transmission T, is described for materials with grain scattering by

$$T_2 = (1-R) \cdot \left(\frac{T_1}{1-R} \right)^{l_2 / l_1} \qquad (2.11)$$

where R is the reflection loss for two surfaces (for example, R=0.14 for alumina).[67]

The scattering coefficient was found to depend upon:

1. the number of scattering centers in the material;
2. the ratio of the particle diameter to the wavelength of the light;
3. the ratio of the refractive indices of the particle and the surrounding medium;
4. the particle shape.

The influence of particle size (factor 2) on scattering, when all other parameters remain constant, is illustrated schematically in Figure 2.13. Maximum scattering occurs when the particle size is around half the light wavelength,[87] about 200 nm for visible light.

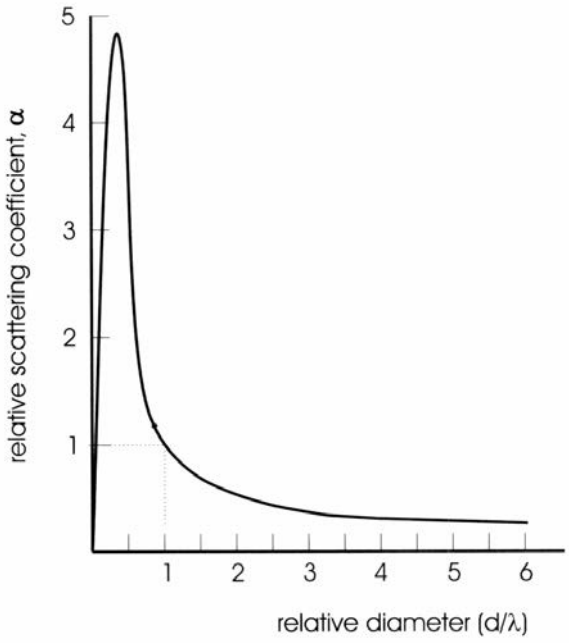

Figure 2.13. The effect of particle size on the relative scattering coefficient.[87]

It is difficult to distinguish bulk scatter from absorption, because both processes decrease the intensity of light transmitted through the sample. The effective absorption coefficient for a sample is therefore:

$$\alpha = \alpha_a + \alpha_s . \qquad (2.11)$$

If there is bulk scatter, the transmittance turns out to be

$$\frac{I}{I_0} = \frac{(1-R)^2 e^{-\alpha d}}{1-R^2 e^{-2\alpha d}} . \qquad (2.12)$$

If we take, for example, a reasonable value of α=0.13 cm^{-1} for AlON at λ=0.55 μm[38] then the transmittance through a non-scatter 1 cm thick window will be 74%.

2.5.2 Microstructural Sources of Light Scattering and the Influence on Transparency[38]

If light passes inside a polycrystalline anisotropic material from one randomly oriented grain to another, it is refracted at each grain boundary (see Figure 2.14) because the refractive index depends on the direction through the crystal. The result is light scattering. In cubic materials, the refractive index is constant and ideally no scatter occurs (assuming a very thin grain boundary). Polycrystalline cubic materials are subject to other scattering mechanisms.

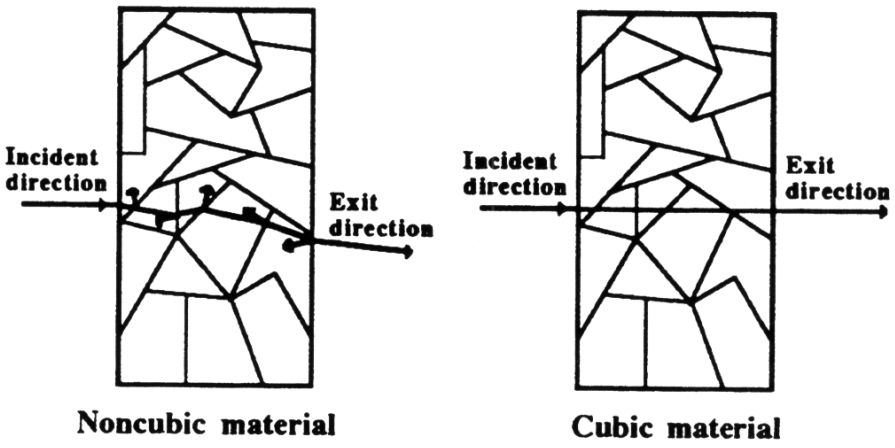

Figure 2.14. Light scattering at grain boundaries occurs only in anisotropic materials.[77]

In general scatter is caused by variations in refractive index as light passes through a material. The reasons for such index variations, or the sources of scatter, may be:

1. Foreign particles: impurities, inclusions of non-cubic AlON phases, AlN crystals or residual porosity (the first ones can also cause absorption).
2. Second phases at grain boundaries.
3. Gradual changes in composition.
4. Structural defects within grains such as dislocations and twins.
5. Strains in the material.
6. Surface scattering (can be reduced by appropriate polishing).

2.5.2.1 Light Scattering from Porosity

The large difference in refractive indices between the gas-filled pores and the ceramic material ($n_{pore}\approx1$, $n_{AlON}\approx1.79$) causes the pores to scatter light very effectively. A residual porosity of ~0.5% usually can be tolerated for a high hardness ceramic such as alumina, but it has to be decreased to <0.05% to obtain a high transmission of light. Coarse grained cubic materials, such as magnesium aluminate spinel or AlON, can be sintered to transparency. In alumina, however, coarse grained materials cannot be sintered to real transparency because of their rhombohedral structure.

Peerlen and Metselaar[88] calculated the scattering caused by porosity with different fixed radii in a thin (0.5 mm) high density alumina sample with a total porosity of 0.2%. The calculated transmission curves as a function of wavelength are shown in Figure 2.15. In reality pore size is not uniform but has some kind of a distribution. After assuming a log-normal pore size distribution, the curves changed and the amplitude of the oscillations for r>0.2 μm (at relatively small wavelengths) decreased.

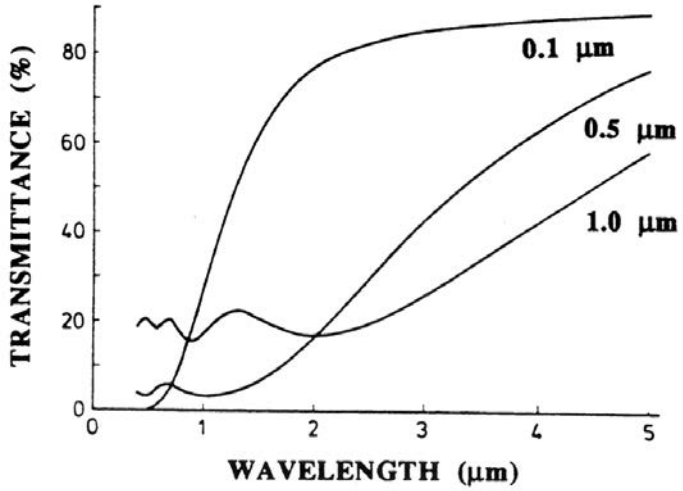

Figure 2.15. Calculated transmission curves for an alumina sample of 0.5 mm thickness with 0.2% porosity of different uniform sizes r, as a function of wavelength.[88]

Apetz and van Bruggen[86] applied a classical Rayleigh-Gans-Debye light scattering model and calculated the transmission reduction caused by pores of different sizes (but fixed total porosity) at a specific wavelength (see Figure 2.16). The pores were assumed to have constant size and be randomly distributed in a homogeneous ceramic matrix. A minimum in the in-line transmission was found to exist when the pores are approximately as large as the wavelength of the incident light. The effect of porosity is extremely strong: even for a porosity of only 0.1%, the real in-line transmission decreases from 85% to 1% in this region of pore sizes. The dependence of transmission T on total porosity p can be written as:

$$T(p_2) = (1-R)\left(\frac{T(p_1)}{1-R}\right)^{p_2/p_1}. \qquad (2.13)$$

Therefore, even at 0.01% porosity, the real in-line transmission decreases significantly to ~55%.

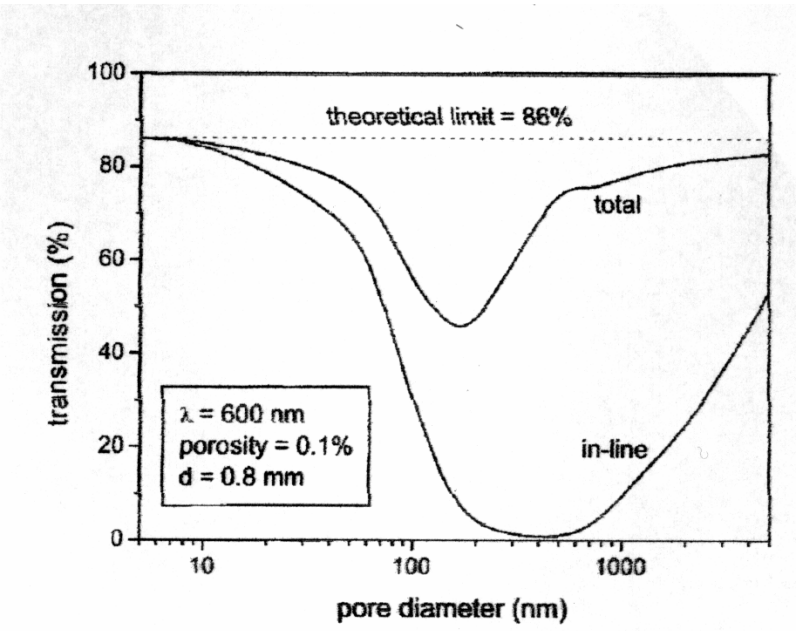

Figure 2.16. Calculated in-line and total (including forward scattering) transmission at 600 nm, 0.1% porosity and 0.8 mm thickness, assuming that the pores are monodispersed and randomly divided over a homogeneous matrix with n=1.76 (for alumina).[86]

2.5.2.2 Influence of Grain Size on Scattering

The influence of grain size on scattering was studied using several translucent polycrystalline materials by Schroeder and Rosolowski[89]. For Lucalox (transparent alumina) samples, which are weak scatterers, it was found that the scattering angle decreased with increasing grain size. The reason is that, in this case, birefringent grain boundary scattering is the dominant mechanism. However, a grain size reduction may be a way of reducing the scattering if second phase or pore formation occurs. Keeping the grain size small can inhibit the growth of the other scattering centers. In a recent work by Krell *et al.*[67], thin polished alumina plates with submicron grains showed real in-line transmission of 55-65%.

Still, porosity is the critical microstructural feature to achieve transparent AlON. The main reasons are that its refractive index (~1) is the furthest possible from that of AlON, and its percentage in the sintered ceramic material is normally much more than 0.05%. Thus, one must sinter AlON to almost 100% TD to obtain transparency.

2.6 Applications

Transparent AlON windows suggest a combination of excellent mechanical, optical, high temperature and chemical resistant properties. AlON is manufactured by conventional powder processing techniques, which are cheaper than single crystal growth techniques that are used to grow sapphire. Also, it can be fabricated in large sizes and to near final size and shape. Its potential applications are derived from its good properties and relatively low costs.

AlON fabrication processes were developed at Raytheon from the beginning of the 1980's, and were scaled up during recent years up to the size of 12x12" and even larger[82] (see for example an old picture of a relatively large window in Figure 2.9).
The potential applications of AlON are:

1. Transparent armor – Commercial transparent armor is composed of glass and plastic laminates. A front hard transparent ceramic layer, such as in opaque ceramic armor, can significantly increase the ballistic performance of the armor. Excellent performance of ballistic laminates, containing Raytheon AlON layers, against armor piercing rounds have been demonstrated.[76,82,90] In comparison to conventional glass/polycarbonate laminates, the same performance was demonstrated at half the areal density and half the thickness. The ballistic AlON optical laminate design was demonstrated in 10"x10" transparent armor window having a single axis of curvature. Multi-hit tests were conducted on 12"x12" AlON tiles as part of transparent laminates, which stopped 4 shots of 0.3" AP M2 bullets.[82] Applications for advanced transparent armor systems include face shields, ground vehicles windows and aircraft windows.[91]
2. Missile domes – High velocity and acceleration missiles which have multimode system of electromagnetic guidance need a transparent dome that can withstand the high temperatures and temperature gradient induced stresses. The dome material should also be abrasion resistant because of water droplets and sand particle erosion during flight. The high durability of AlON makes it a good candidate to replace the current dome materials.[74-75,82] Furthermore, AlON can be formed into a hemispherical dome shape close to final tolerances, and as a consequence it is cheaper than single crystals.

3. Other applications – Laser igniter windows for cannon applications, missile warning windows, underwater applications, advanced refractories in the metallurgical industry, optical materials at high temperatures (such as for lamp envelopes[26]) and other military and commercial applications.[20,82,91,92]

3. Research Goals

1. Synthesis and processing of single phase γ-AlON by reactive sintering of an AlN and α-Al_2O_3 powder mixture.
2. Characterization of the influence of sintering temperature and time on the density of AlON.
3. Characterization of the influence of MgO, La_2O_3 and Y_2O_3 additives on the microstructure and optical transmission of AlON.

4. Experimental Methods

4.1 Process Description

In this chapter the processing, experimental and characterization methods used in the research are described. The process used to prepare AlON samples was generally described in section 2.2.1. In order to allow for maximum transparency the raw materials must be as pure and fine as possible. Purity is needed because impurities may scatter light. Fine particles are needed to enhance mixing and reactivity of the powders, and to avoid inhomogeneous sintering. According to these guidelines three commercially available Al_2O_3 powders and one type of AlN powder were chosen (see Table 4.1).

Table 4.1. Raw materials (α-Al_2O_3, AlN) used to synthesize AlON.

	Source & grade	**Purity**	**Trace impurities**	**Average perticle size [μm]**
AlN	Starck grade C	98.5%	O – 1.43 wt.% C – 500 ppm Fe – <20 ppm	2.34
α-Al_2O_3	Alcoa A16 SG	99.7%	Maximum: Na_2O – 1000 ppm MgO – 600 ppm SiO_2 – 500 ppm CaO – 500 ppm Fe_2O_3 – 300 ppm	0.2-0.62
α-Al_2O_3	Ceralox SPA-0.5	99.995%	Si – 15 ppm Na – 10 ppm Mg – 8 ppm Fe – 6 ppm Ca – 3 ppm	0.52
α-Al_2O_3	Taimei TM-100D	99.99%	-	0.01

In stoichiometric AlON there is a molar ratio of 9:5 between Al_2O_3 and AlN. However, as seen in Figure 2.1, nonstoichiometric compositions may also be used to produce AlON. Therefore, two molar ratios were used in the research: 35.7 mol% AlN (stoichiometric) and 30 mol% AlN (nonstoichiometric). Several mixtures of Al_2O_3 and AlN were ball milled with Teflon balls (to obtain polymeric erosion products only) and iso-propanol (IPA) as a grinding medium. Powder mixtures were

ball milled for 24 hrs and then dried at 75^0C for 24 hrs. The dried powder was sieved through 400 mesh and pressed into samples of 30 mm diameter and varying thickness. The uniaxially applied pressure was 100 MPa. The green density was in the range of 55-60% of the theoretical density, except for powder mixtures with the Taimei alumina powder which is very fine and thus yielded only a green density of ~40%.

Additives were introduced into some of the mixtures in the form of metal oxide powders or hydrate salts (see Table 4.2), in the ball milling stage. All the salts dissolved in the alcohol medium. The role of the additives is to enhance densification during the sintering stage.

Table 4.2. Additive substances used in the synthesis of AlON.

	Source & grade	Purity	Main impurities (ppm)
$C_4H_6MgO_4 \cdot 4H_2O$	Fluka 63051	99.5%	-
La_2O_3	Merck 12220	-	-
$La(NO_3)_3 \cdot 6H_2O$	Aldrich 33193-7	99.999%	Si – 2.1 ; Ba – 1.5 ; Al – 1.4 ; Ca – 1.3 ; Ce – 1.2 ; Na – 0.7
$Y(NO_3)_3 \cdot 6H_2O$	Aldrich 23795-7	99.999%	Na – 5.6 ; Ca – 1.7 ; Yb – 1.1 ; Er – 1.0

The compositions of the various powder mixtures prepared are listed in Table 4.3. The pressed samples were sintered in a graphite furnace under flowing nitrogen at various conditions of temperature and time. Sintering was performed in a graphite crucible with a powder bed of h-BN (Carborundum SHP-40) or AlON (synthesized by Sienna Technologies). This AlON powder was also pressed and sintered as a reference sample. It was further characterized, as described in chapter 5.

Table 4.3. Compositions of powder mixtures prepared to sinter AlON.

Designation	Mol% AlN	Alumina type	Mg Additive	La Additive	Y Additive
E	30	Alcoa	-	-	-
F	35.7	Alcoa	-	-	-
G	35.7	Alcoa	-	-	-
H	35.7	Taimei	-	-	-
I	35.7	Ceralox	-	-	-
J	30	Ceralox	-	-	-
MA	30	Alcoa	0.3 wt.%	-	-
MB	30	Alcoa	0.6 wt.%	-	-
MC	30	Ceralox	0.3 wt.%	-	-
MD	30	Ceralox	0.05 wt.%	-	-
MLA	30	Alcoa	0.3 wt.%	0.02 wt.%	-
MLB	30	Alcoa	0.3 wt.%	0.1 wt.%	-
MLC	30	Ceralox	0.3 wt.%	0.1 wt.%	-
MLD	30	Ceralox	0.3 wt.%	0.2 wt.%	-
MLE	30	Ceralox	0.05 wt.%	0.02 wt.%	-
LA	30	Cerloax	-	0.1 wt.%	-
YA	35.7	Alcoa	-	-	0.08 wt.%
MYA	30	Ceralox	0.05 wt.%	-	0.08 wt.%
YLA	35.7	Alcoa	-	0.02 wt.%	0.08 wt.%
MLYA	30	Ceralox	0.05 wt.%	0.02 wt.%	0.08 wt.%

4.2 Characterization Methods

4.2.1 Density

Density measurements of sintered samples were conducted using the Archimedes method according to ASTM B311. The density of green samples was estimated by dividing their weight by their volume.

4.2.2 Hardness

Hardness was determined using a diamond knoop penetrator on a Buehler microhardness machine. Measurements were conducted using a 1 kg load according to ASTM E92. The lengths of the trace diagonals were translated into hardness units. The reported results are the average of at least 5 measurements.

4.2.3 Chemical Analysis

The composition of powders and sintered samples were analyzed by Dirats laboratories (Westfield, MA, USA). Oxygen and nitrogen contents were determined by IGF (inert gas fusion) method. The samples were fused, and the gaseous products were transported along with a noble gas to a gas chromatograph.

Metal contents were determined by ICP-OE (inductively coupled plasma optical emission spectroscopy). In this method the samples are ionized and radiate. Composition is an outcome of the emission spectrum. Carbon and sulfur were measured by combustion. The samples were heated until combustion occurred. The emitted gases were identified using infrared radiation or thermal conduction.

4.2.4 XRD

The XRD (X-Ray Diffraction) system used in this study was a Philips PW-3020 including CuKα X-Ray tube (λ=1.5406 nm), operating at 40 kV and 40 mA. Diffraction patterns were acquired routinely between 18 and 145° (2θ) at steps of 0.005-0.02° and 1-4 second/step exposure. Only polished samples were examined. The XRD results were used to identify the phases present in the samples: AlON, unreacted phases (Al_2O_3, AlN) and other secondary phases. Phase identification was done using JCPDS cards and results in the literature.[32]

4.2.5 SEM

SEM (Scanning Electron Microscopy) was conducted on a JEOL 840 JSM at an accelerating voltage of 20 kV. Both secondary electron (SE, for examination of microstructure and fracture surfaces) and backscattered electron (BSE, for phase discrimination) detectors were used. Specimens for Optical Light Microscopy and SEM were ground and polished, and chemically etched in boiling phosphoric acid (H_3PO_4)[74] for 20 minutes. A gold-palladium coating was applied to the specimens to avoid ionization under the electron beam in SEM.

4.2.6 EDS

EDS (energy dispersive spectroscopy) analysis was conducted on Philips XL-30 SEM using a LINK ISIS system (Oxford Instruments), in order to quantitatively identify the elements in the sample. An accelerating voltage of 10 kV, a working distance of 10.5 mm and a cobalt standard sample were used. Carbon coating was applied to the specimens.

4.2.7 WDS

WDS (wavelength dispersive spectroscopy) analysis was conducted on Philips XL-30 SEM in order to quantitatively measure low concentration elements in AlON (dopant concentrations).

4.2.8 TEM

TEM (transmission electron microscopy) was conducted on a JEOL FX 2000 microscope with an accelerating voltage of 200 kV. Thin electron-transparent specimens were prepared from a studied sample by mechanical thinning, followed by dimple grinding (Gatan Dimpler) and ion-milling (Gatan PIPS) at 5.0 kV. Electron diffraction was used to verify the crystallographic symmetry of the AlON crystal.

4.2.9 Spectrophotometer

Spectrophotometer systems were used to measure optical transmission through sintered samples: Perkin-Elmer Lambda-900 machine for the ultraviolet, visible and infrared regions (λ<2500 nm) and Perkin-Elmer 983G machine for the infrared region (λ>2500 nm). The spectrophotometers were calibrated using transparent sapphire.

5. Results

5.1 Process Development

In the beginning of the study an Astro furnace with metal heating elements was used. A few sintering experiments were conducted at its highest temperature (1800°C) under nitrogen. The resulted sintered samples were opaque (white) with densities of 85-90% TD. XRD runs of these sintered samples showed mostly AlON phase with AlN traces.

Using a graphite furnace (CENTORR) which can reach up to 2400°C made it possible to achieve sample densities very close to the theoretical density. Various sintering experiments were conducted at temperatures between 1800°C and 2025°C. In each experiment up to 14 samples were sintered in three separate graphite crucibles that were put one on the top of another, with a slight shift to allow the flow of gas. This allowed co-sintering of samples with different compositions at the same time. Thus, a comparison between samples could be performed on the basis of processing parameters (sintering temperature and time) and composition (Al_2O_3/AlN ratio and dopants content).

Samples made of both 30 and 35.7 mol% AlN were sintered by various sintering routes (temperatures and times). The color of the sintered samples was usually white or gray. A layer of powder bed material adhered to the lower side of part of the samples. In some cases (in different sintering processes) long and thin needles formed on the upper side of the samples. This phenomenon was not investigated in the current study, but should be studied in the future.

5.2 Dilatometric Analysis

Dilatometry experiments were conducted on two specimens, the first being a pure AlON specimen and the second being a doped one with both Mg and La additives. The two goals of these experiments were:

a) to see at which temperature region most of the densification takes place;

b) to learn about the difference in sintering rate between pure and doped specimens.

The specimens were prepared from two pressed samples (see section 4.1). The "pure" sample contained 35.7 mol.% AlN (G mixture), while the "doped" sample contained 30 wt.% AlN and 0.3 wt.% Mg and 0.02 wt.% La (MLA mixture). The dilatometry specimens were approximately 3.5x3.5x10 mm. Temperature profile included heating to 2000°C at a rate of 300°C/hr, soaking time of 15 hrs and cooling at a rate of 750°C/hr. The procedure was conducted under pure nitrogen by Anter Lab (Pittsburgh, PA, USA) on Unitherm 1252 machine. Molybdenum plates were used as separation layers between the specimen and the graphite heating elements, to avoid an undesirable reaction between them.

The sintered specimens were visually very different from each other: the pure one had a white color, while the doped one was translucent. The dilatometry results, which are presented in Figures 5.1 and 5.2, show that the sintering (shrinkage) commences at approximately 1100°C, when the material is still composed of two phases (AlN and Al_2O_3). A sudden expansion of the specimen begins after ~5.75 hrs of heating, or around 1760°C and 1720°C (for pure and doped specimen, respectively). This corresponds to the beginning of reaction between AlN and Al_2O_3, which occurs around 1650°C (see phase diagram in Figure 2.1). The volume increase is slightly delayed in the experiment because of the relatively high heating rate. The reason for the volume increase is the difference between unit cell volumes of AlON and the two reacting phases[93], according to reaction (2.2):

$V_{unit\ cell}\ (Al_2O_3) = \sqrt{3}/2 \cdot 4.759^2 \cdot 12.989/6 = 42.46\ Å^3$.

$V_{unit\ cell}\ (AlN) = \sqrt{3}/2 \cdot 3.1127^2 \cdot 4.9816/2 = 20.90\ Å^3$.

$9 \cdot V_{unit\ cell}\ (Al_2O_3) + 5 \cdot V_{unit\ cell}\ (AlN) = 9 \cdot 42.46 + 5 \cdot 20.90 = 486.6\ Å^3$.

$V_{unit\ cell}\ (AlON) \approx 7.948^3 = 502.1\ Å^3$.

This calculation shows a ~3.2% volume increase due to the reaction. However, the nature of the experiment is such that reaction and sintering (densification) occur at the same time, so the volume increase may be less than the calculated value.

As presented in Figures 5.1 and 5.2, the expansion is much more extensive for pure AlON than for doped AlON (6% vs. 0.5%). Furthermore, it lasts for a longer time and ends at 1850°C, while the doped specimen continues shrinking at 1770°C. The difference between the two behaviors can be the result of a liquid phase which forms at these temperatures, diminishes the volume increase, and pushes towards the continuation of densification.

The shrinkage rate significantly decreases when the temperature reaches 2000°C. However, shrinkage continues during the soaking period at 2000°C. This may be the result of Al-O-N species vaporization.

To summarize these results, there is a clear influence of the additives on the sintering rate. It is not fully understood why the ~1750°C expansion of the pure specimen is greater than expected by theory and what causes the large difference in the overall shrinkage. However, the appearance of the sintered specimens demonstrated that the doped sample was much closer to full density.

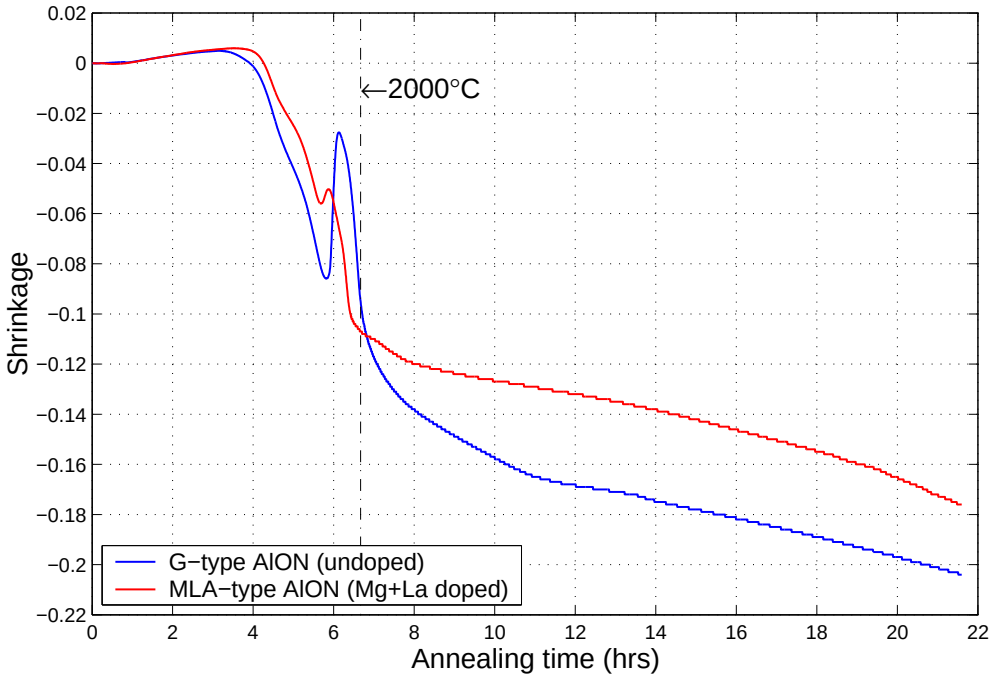

Figure 5.1. The relation between relative shrinkage and the sintering time of pure and doped AlON.

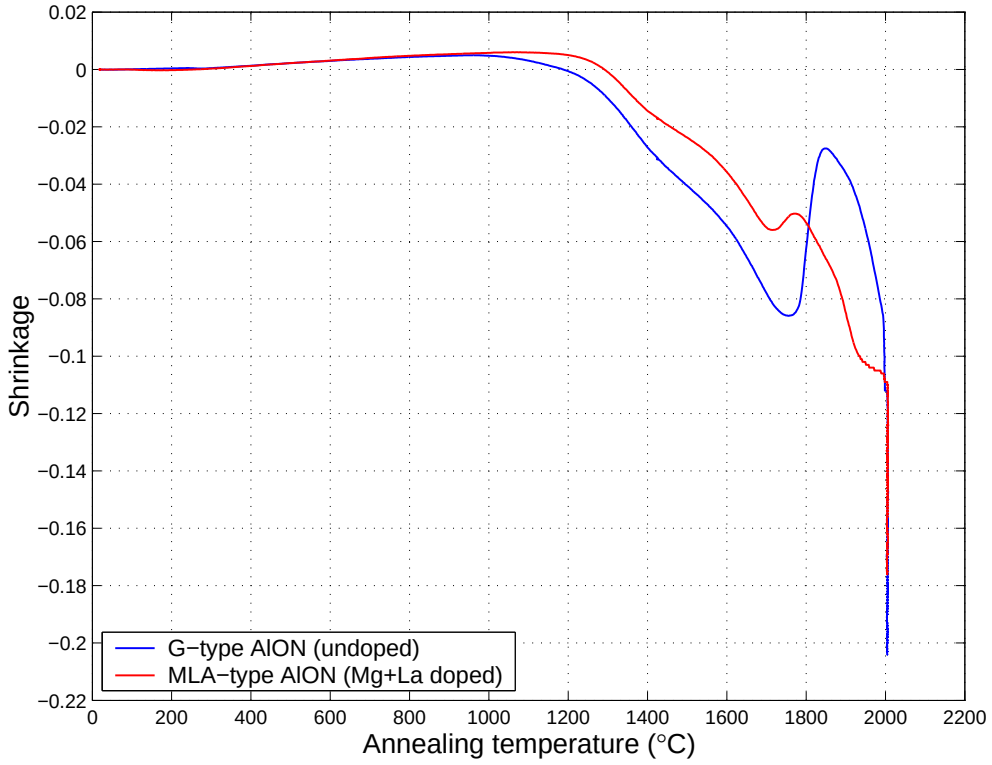

Figure 5.2. The relation between relative shrinkage and the sintering temperature of pure and doped AlON.

5.3 Phase Identification by XRD

5.3.1 XRD Patterns of AlON

A reaction experiment was conducted at 1750°C for 4 hrs. A loose I-type powder mixture (of 35.7 mol% AlN and Ceralox Al_2O_3) was heated in an alumina crucible. XRD of the produced powder showed that it is almost completely AlON, with some AlN traces. The results are shown in Figure 5.3, with a comparison to an AlON powder produced by Sienna, which contains Al_2O_3 traces in addition.

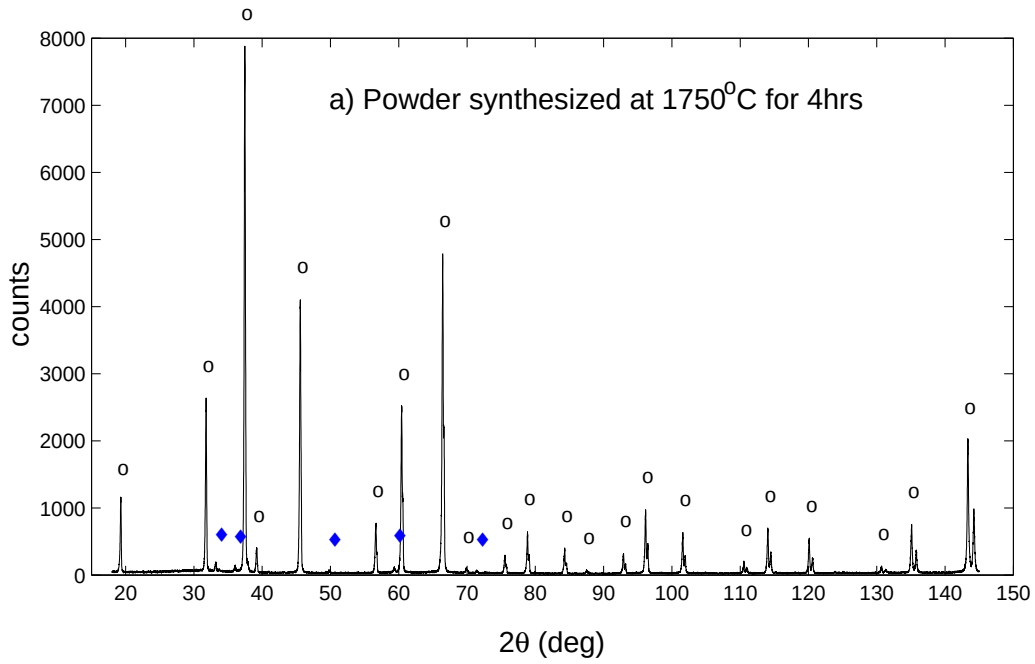

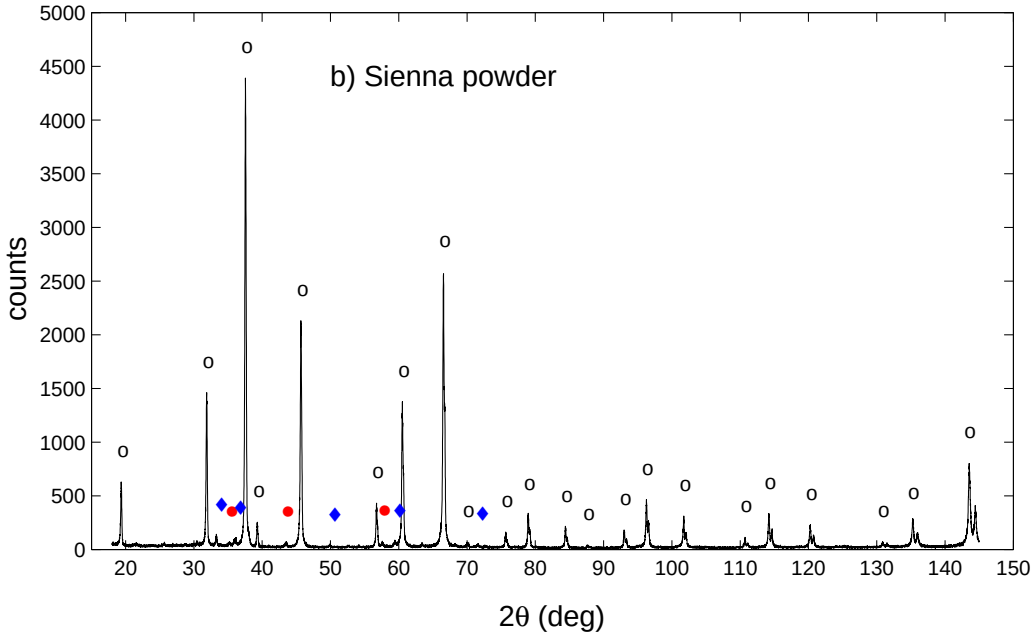

Figure 5.3. a) XRD of AlON powder synthesized at 1750°C for 4 hrs, b) XRD of AlON powder produced by Sienna; ○ - AlON , ♦ - AlN , ● - Al_2O_3.

The reflections attributed to AlON are summarized in Table 5.1. Those used for determining the lattice parameter (provided that they appeared in the XRD pattern) are marked with a 'yes' in the last column.

Table 5.1. Reflections attributed to AlON with lattice parameter of 0.7950 nm (Cu Kα radiation). The last column indicates whether the reflection was used while determining the lattice parameter.

{ h k l }	2θ (°)	d-value (nm)	used
111	19.32	0.45899	No
220	31.81	0.28107	No
311	37.49	0.23970	No
222	39.22	0.22950	No
400	45.61	0.19875	No
422	56.68	0.16228	No
511 & 333	60.46	0.15300	No
440	66.47	0.14054	No
531	69.95	0.13438	No
620	75.58	0.12570	Yes
533	78.89	0.12124	Yes
444	84.33	0.11475	Yes
711 & 551	87.57	0.11132	Yes
642	92.95	0.10624	Yes
731 & 553	96.19	0.10350	Yes
800	101.63	0.09938	Yes
733	104.93	0.09712	Yes
822 & 660	110.60	0.09369	Yes
751 & 555	114.09	0.09180	Yes
840	120.14	0.08888	Yes
911 & 753	123.94	0.08726	Yes
664	130.71	0.08475	Yes
931	135.12	0.08334	Yes
844	143.37	0.08114	Yes

The surface phase composition was found by XRD scans to be a mixture of AlON and AlN. After grinding the surface layer, the inner (bulk) part was found in most of the cases to be single phase AlON. This fits the result of Willems,[32] that AlN remains on the surface of the sintered AlON bulk when a graphite crucible is used. An example of the influence of grinding (from an E-type sample) is shown in Figure 5.4.

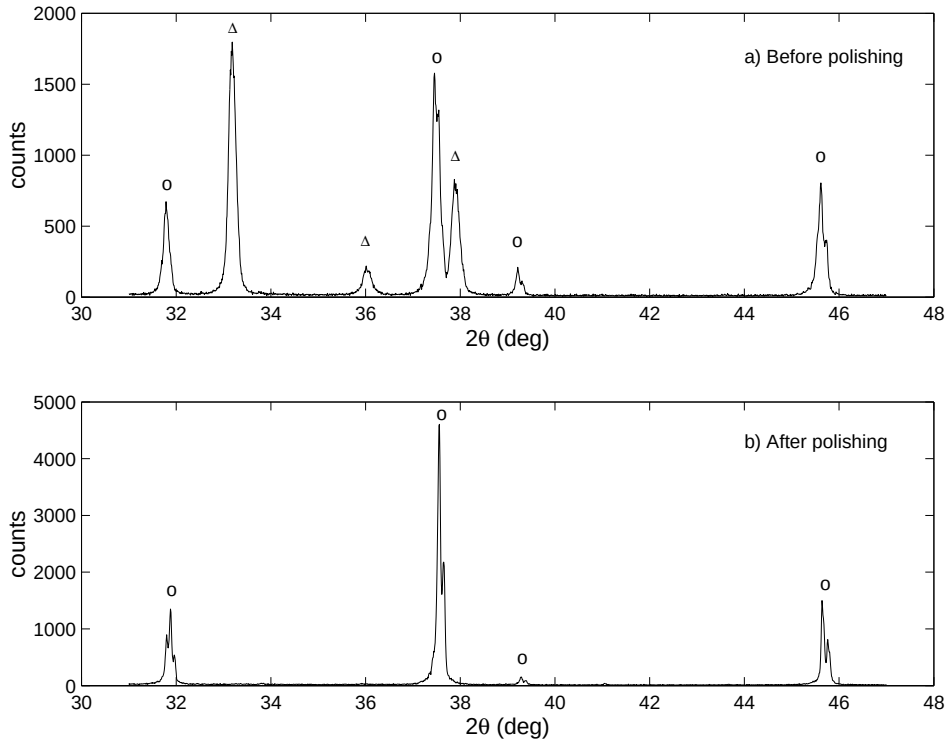

Figure 5.4. XRD of E-type AlON sample sintered at 1800°C for 2 hrs and then at 1950°C for 2 more hrs: a) as sintered, b) after polishing; ○ - AlON , Δ - AlN.

One characteristic of the XRD patterns is that even among single phase AlON samples, the ratios between peak intensities significantly differed from one sample to another. This can be explained by the relatively large grain sizes (as will be shown later). This means that the X-ray beam interacts with only a small number of grains, which causes an artificial effect of preferred orientation. Figure 5.5 demonstrates the significant difference in peak intensity ratios between XRD patterns for two different samples. This effect was also seen while running two XRD tests for the same AlON sample. All of the samples were ground before XRD tests to remove surface phases.

Another interesting phenomenon to mention is that a long dark mark was generated on the surface of the specimen where X-rays interacted with it. The reason for this is radiation damage caused by the interaction with color centers in AlON. Comparison between XRD patterns of various doped and undoped sintered AlON samples does not show any difference, except for the above mentioned irregular peak intensities as a result of the large grain size.

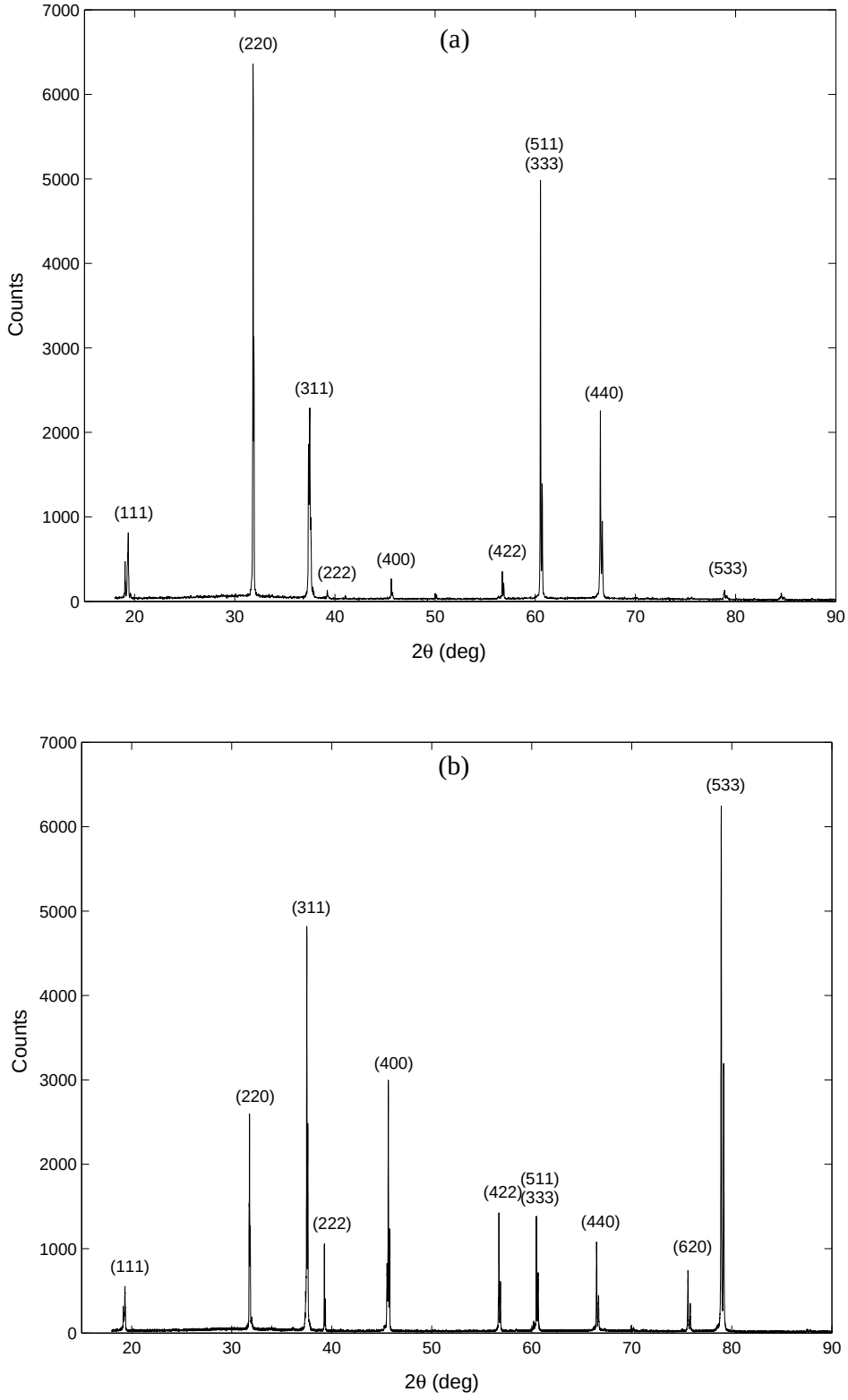

Figure 5.5. XRD patterns of: a) J-type sample, b) LA-type sample.

5.3.2 Lattice Parameter Calculations

XRD results were used to determine the lattice parameters of the different AlON samples. This was done by plotting the calculated lattice parameter from the position of each peak (according to Bragg's law), and plotting the results against a function f(θ), which is given by:

$$f(\theta) = \frac{\cos^2 \theta}{\sin \theta}. \qquad (5.1)$$

The lattice parameter was obtained by extrapolation of f(θ) to 0 (or θ to 90°). Only clearly observed and sharp AlON peaks between 75 and 145° (2θ) were used for this calculation (see e.g. Cullity[94] for more details of this procedure).

If we take into account only the AlN/Al_2O_3 ratio and ignore the various dopants added, we can compare samples with 30 mol% AlN to those with 35.7 mol% AlN. The average lattice parameter in the first case was a=0.7948±0.0002 nm, while in the latter was a=0.7954±0.0002 nm. Assuming a linear correlation between the lattice parameter of the material and its AlN content, it may be estimated as:

$$a\ (Å) = 7.922 + 0.0035x\ , \qquad (5.2)$$

where x is the atomic percent nitrogen content. This relation is depicted in Figure 5.6, along with a comparison to some other relations from the literature. The agreement between our results and those from other works is very good. The dopants seem to have no significant influence on the lattice parameter. The transparent sample from Surmet was found to have a=0.7947±0.0001 nm. This means that its composition is around 30 mol% AlN.

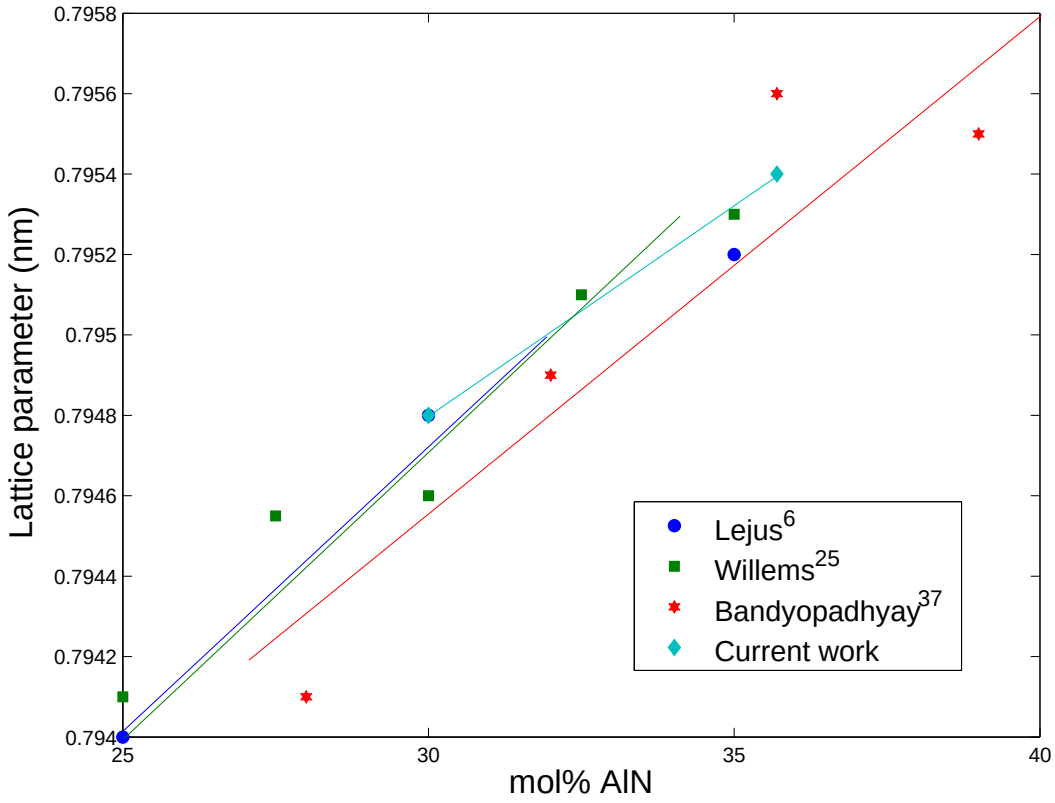

Figure 5.6. Lattice parameters determined for various AlON samples (doped and undoped) with different Al_2O_3/AlN ratios, with a comparison to some results from the literature.

5.4 Quantitative Elemental Analysis

Three methods were used to analyze the chemical composition (main elements, doping substances and impurities) of ball milled powders and sintered samples: chemical analysis, EDS and WDS.

5.4.1 Chemical Analysis

The compositions of several ball milled powder samples and of a transparent AlON sample of Surmet were measured by chemical analysis. The results are given in Table 5.2.

Table 5.2. Compositions of powder mixtures and Surmet transparent AlON plate. In parentheses are the concentrations of dopants added to the mixtures.

	J powder	YLA powder	MLYA powder	Surmet plate
Al (%)	55.96	58.13	55.34	52.89
O (%)	39.50	36.61	39.69	40.84
N (%)	4.44	4.98	4.57	6.13
C (%)	0.062	0.065	0.14	<0.001
Mg (ppm)	11 (0)	210 (0)	800 (500)	100
La (ppm)	1 (0)	210 (200)	220 (200)	<100
Y (ppm)	24 (0)	820 (800)	840 (800)	<100
Na (ppm)	20	360	210	<100
Ca (ppm)	80	210	190	<100
Si (ppm)	35	110	90	<100
Fe (ppm)	8	16	26	100
Cr (ppm)	3	3	12	<100

It should be mentioned that powder J was prepared from the purer Ceralox alumina powder, while the two other powders were prepared from the Alcoa powder. The analysis results show this difference very well. There are less impurities (such as Na, Ca, Si and Fe) in powder J than in the two other powders. Moreover, the YLA powder mixture was prepared from 35.7 mol% AlN, while the other two were prepared from 30 mol% AlN. This difference can also be observed in the main elements part of Table 5.2. However, the nitrogen content is consistently lower than it should be, and the oxygen content is consistently higher than it should be. Although the magnesium concentration is consistently too high (apparently because of Mg impurities), the La and Y concentrations are very close to the expected values.

The Surmet plate is richer in anion elements (O,N) and poorer in cations (Al) than the powder mixtures. The Al content is as low as that of Al_2O_3, which is lower than AlN. This can be explained by the introduction of nitrogen atoms from the atmosphere into the material, which reduces the aluminum weight percentage. The very low carbon content is expected since the material is transparent, and this can be the result of firing the material before sintering to remove all the organic species. The tests that were conducted succeeded in detecting Mg and Fe impurities, which could be added deliberately or not deliberately. It can only be assumed that 0.01 wt.% Mg is a sintering aid, and 0.01 wt.% Fe is an impurity from one of the sample preparation

stages. Other impurities, even though found in other methods (see next section), were not detected by these methods.

5.4.2 EDS and WDS Analyses

The compositions of some sintered samples as well as the transparent AlON of Surmet were measured by SEM-EDS/WDS. The main elements (Al, O, N) were analyzed by EDS. The dopants were measured by WDS. The results are shown in Table 5.3.

Table 5.3. Compositions of sintered AlON samples measured by EDS and WDS.

	G	I	YA	MLC	YLA	Surmet
Al (wt.%)	57.2	56.7	57.0	58.0	57.7	56.9
O (wt.%)	37.5	38.9	40.5	37.6	38.6	38.11
N (wt.%)	5.2	4.4	2.5	4.4	3.7	5.0
Mg (wt.%)	-	-	-	0.30	-	0.0025
La (wt.%)	-	-	-	*	0.04	<0.0032
Y (wt.%)	-	-	0.067	-	0.076	<0.0080

* inhomogeneous distribution of intergranular $LaAl_{11}O_{18}$ phase, see section 5.5.2.

Table 5.3 lets us learn about the accuracy of the dopant concentrations. Whereas La measurements indicates that its concentration, which is the lowest, is larger than expected (0.04 instead of 0.02 wt.%), the Y and Mg concentrations are almost exactly what actually was added. This contradicts the chemical analysis results (for powders), and the explanation for this difference is unclear.

For the sample of Surmet a few more elements were measured by WDS, which are suspected to be impurities in the alumina raw powder. These are Ca, Na and Si. Whereas the Na content was found to be less than the detection limit (0.0016 wt.%), Si and Ca were identified to be present with 0.013 and 0.0013 wt.%, respectively. This relatively high amount of Si may hint that the raw powder was not very pure, or part of it was introduced intentionally.

5.5 Microstructure Characterization

5.5.1 Microstructure of Etched Samples

Chemically etched samples were examined using optical microscopy and SEM in order to investigate the microstructure, measure grain size and to find any kind of defects. Usually the grains can be easily distinguished by their color (brightness or darkness). The brightness contrast may be the result of the different reaction of acid etching on the different crystal planes exposed on the surface of each grain. The etching process also significantly emphasized many scratches, which could hardly be observed beforehand.

Figure 5.7 presents a SEM micrograph of undoped AlON sample.

Figures 5.8 and 5.9 show optical micrographs of Mg doped AlON samples (MC and MB, respectively). The difference between these two samples is their composition (MC has less Mg than MB). The microstructures suggest that increasing Mg concentration causes the grains to be less equiaxed and homogeneous.

Figure 5.10 show the microstructure of an MYA sample. The yttrium addition did not cause any noteworthy change in the general appearance of the microstructure, except for the smaller grain size, which is a result of the lower sintering temperature.

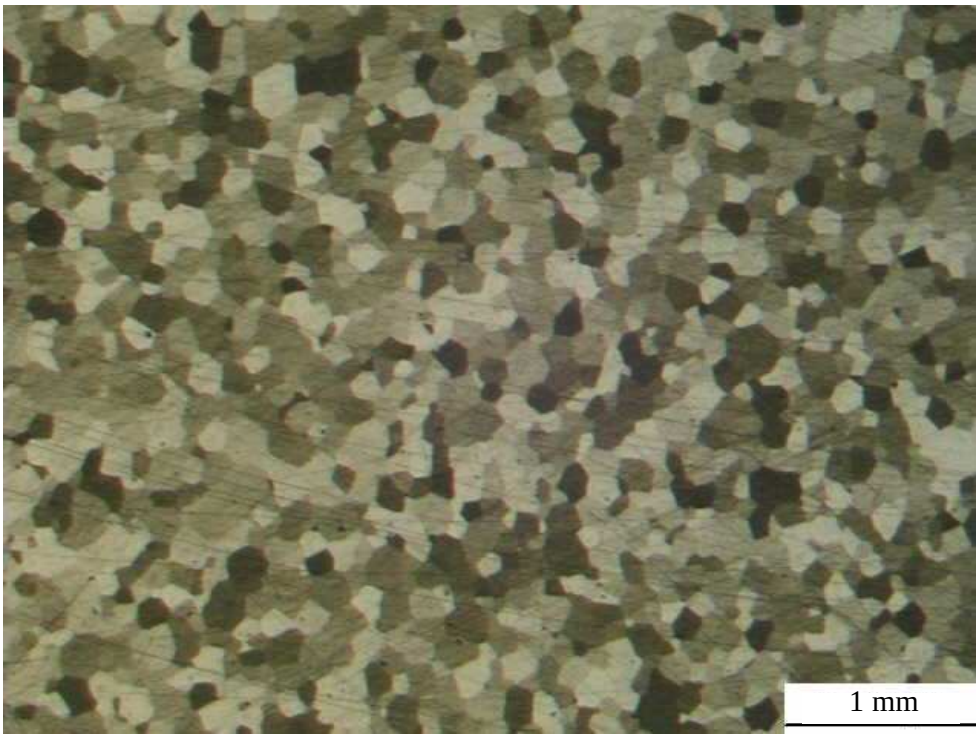

Figure 5.7. Optical micrograph of a J-type sample sintered at 2010°C for 12 hrs (originally x12.5).

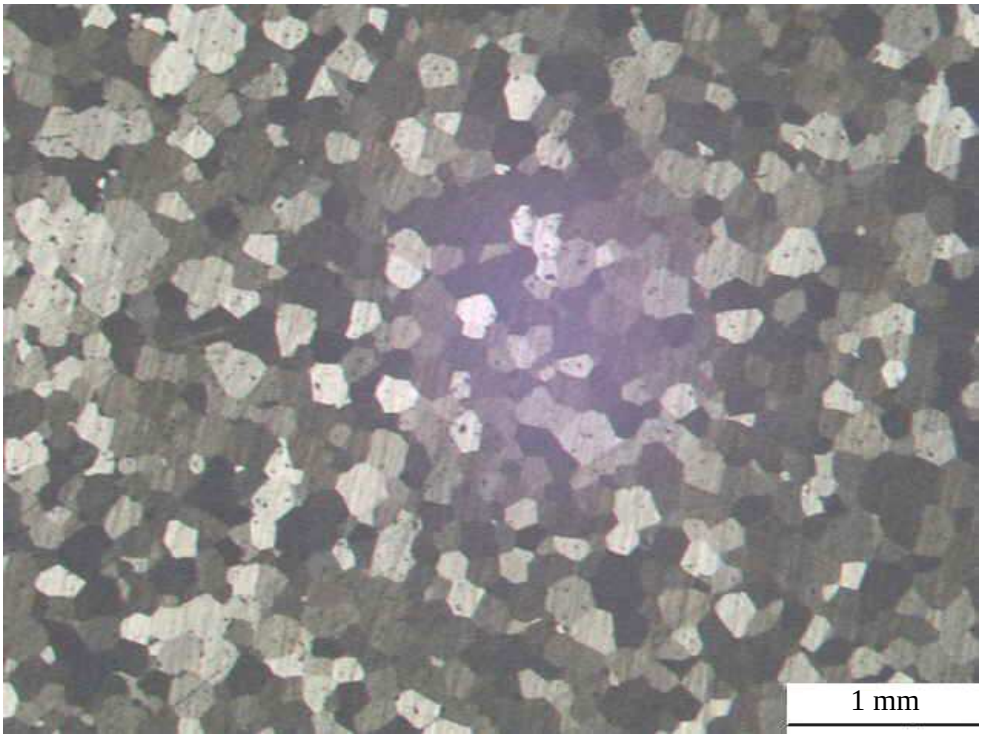

Figure 5.8. Optical micrograph of an MC-type sample sintered at 2010°C for 12 hrs (originally x12.5).

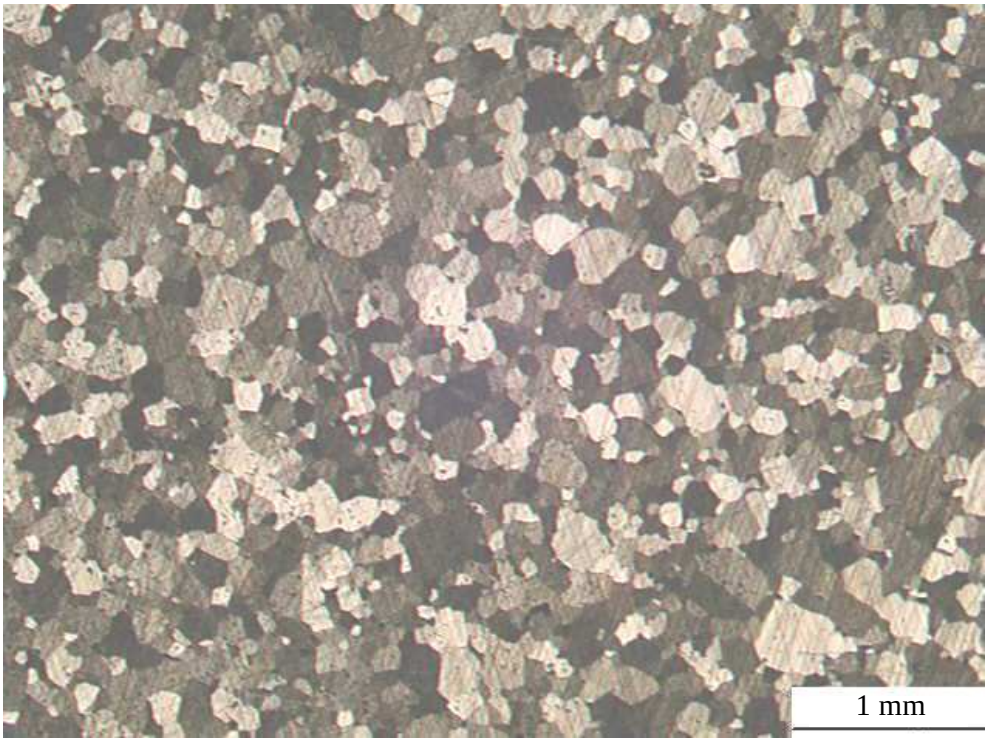

Figure 5.9. Optical micrograph of an MB-type sample sintered at 2010°C for 12 hrs (originally x12.5).

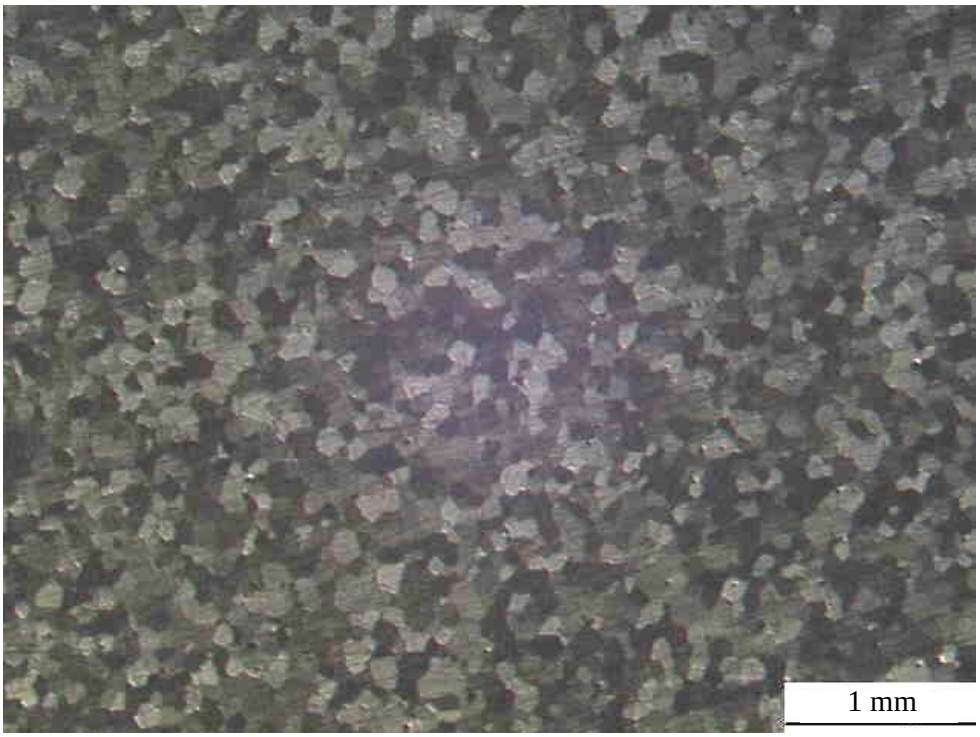

Figure 5.10. Optical micrograph of an MYA-type sample sintered at 1930°C for 12 hrs (originally x12.5).

Extensive twinning can be observed in the microstructures of LA, YLA and MLD samples (Figures 5.11-5.13). In fact, all the examined samples which were prepared with La had twinned grains.

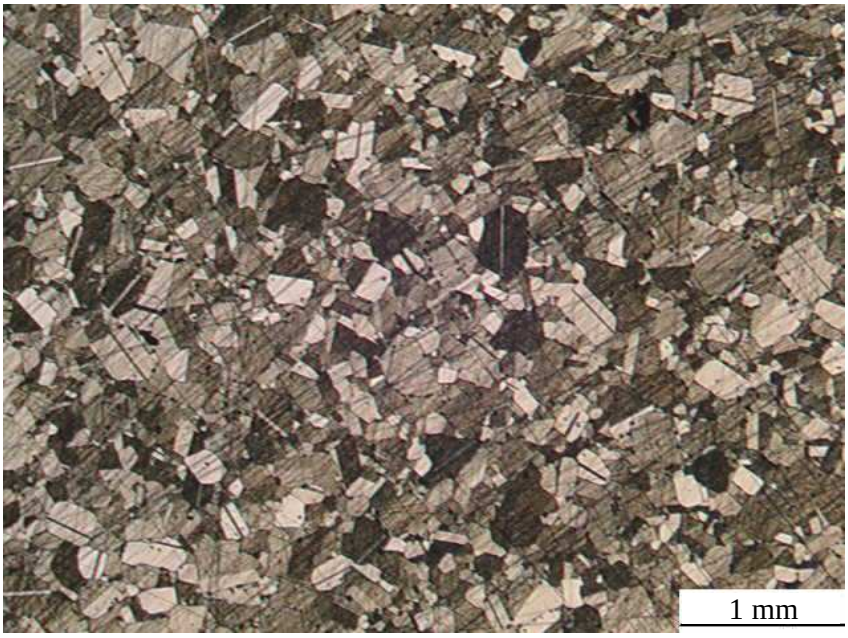

Figure 5.11. Optical micrograph of an LA-type sample sintered at 1930°C for 12 hrs (originally x12.5).

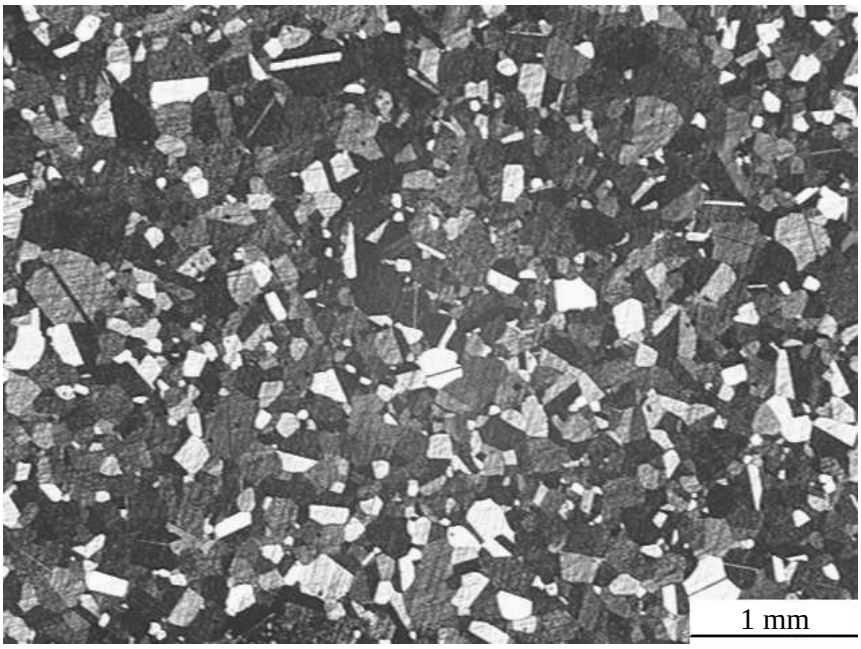

Figure 5.12. Optical micrograph of a YLA-type sample sintered at 1930°C for 12 hrs (originally x12.5).

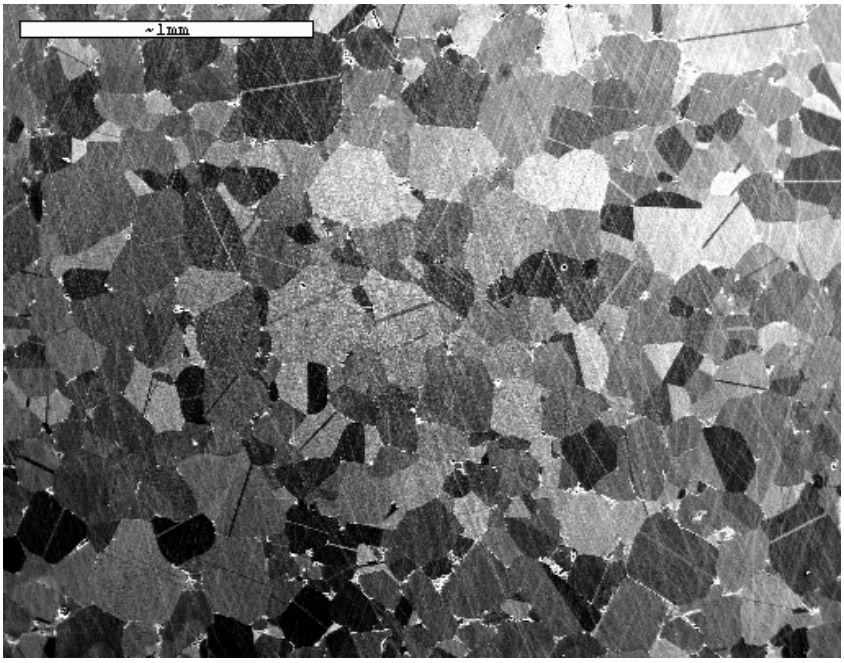

Figure 5.13. SEM microstructure of an MLD-type sample sintered at 2000°C for 12 hrs (originally x40).

Besides twinning, Figure 5.13 demonstrates another phenomenon. Careful examination of the microstructure reveals a white phase which is located at some of the grain boundaries. This MLD-type sample contains 0.2 wt.% La, which is a significantly higher La concentration than in the previous cases. More on this La enriched secondary phase can be found in section 5.5.2.

Finally, the microstructure of the etched transparent sample of Surmet is presented in Figure 5.14. Although etched in the same way as all other samples, this micrograph does not show colored grains, but grooved grain boundaries. It is interesting to mention that after heating the Surmet sample to 2000°C for 4 hrs, it exhibited a contrast similar to the other sintered samples, as described in section 5.7.

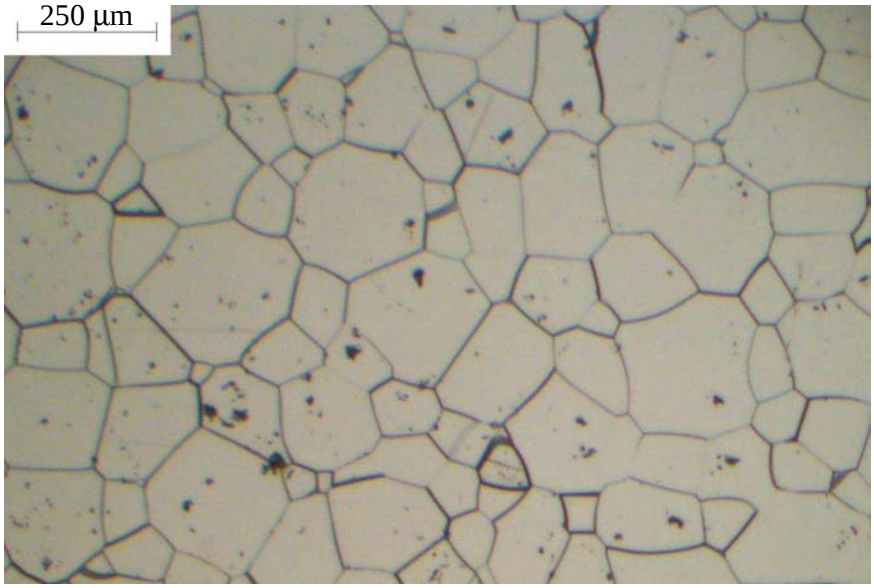

Figure 5.14. Optical micrograph of a transparent sample from Surmet (originally x25).

5.5.2 Fracture Surfaces

Fracture surfaces of various samples were examined using SEM, to look at the amount and distribution of porosity, and at the fracture mode.

Figure 5.15 shows the fracture surface of an E-type sample sintered in a two-step route: 2 hrs at 1800°C and then 2 hrs at 1950°C. The porosity which can be seen is occluded inside the grains or located at grain boundaries. The density measured for this sample was 96% of the theoretical density. A similar micrograph is presented in Figure 5.16, which shows the fracture surface of an F-type sample sintered at 1950°C for 4 hrs, with a density of 97%.

The sintering routes used for the two samples shown in Figures 5.15 and 5.16 included heating to the elevated temperature at a rate of 500 °C/hr. Figure 5.17 shows the fracture surface of an F-type sample which was sintered in the same sintering route as the previous one, but with a heating rate of 900 °C/hr. This change increased the density to 98%. From the comparison between Figures 5.16 and 5.17, one can conclude that the higher the heating rate, the smaller the remaining pores. All of the following samples were sintered with a heating rate of 900 °C/hr.

Figure 5.18 shows the fracture surface of an I-type AlON sample sintered at 2000°C for 12 hrs. The main difference in this micrograph compared with the previous ones, is the larger grain size. There is still a significant amount of porosity, and the density measurement indicates that it is 99.5% of the theoretical density.

It should be mentioned that all the undoped AlON samples mostly exhibited intragranular fracture mode, while the doped samples fractured either between or through grains.

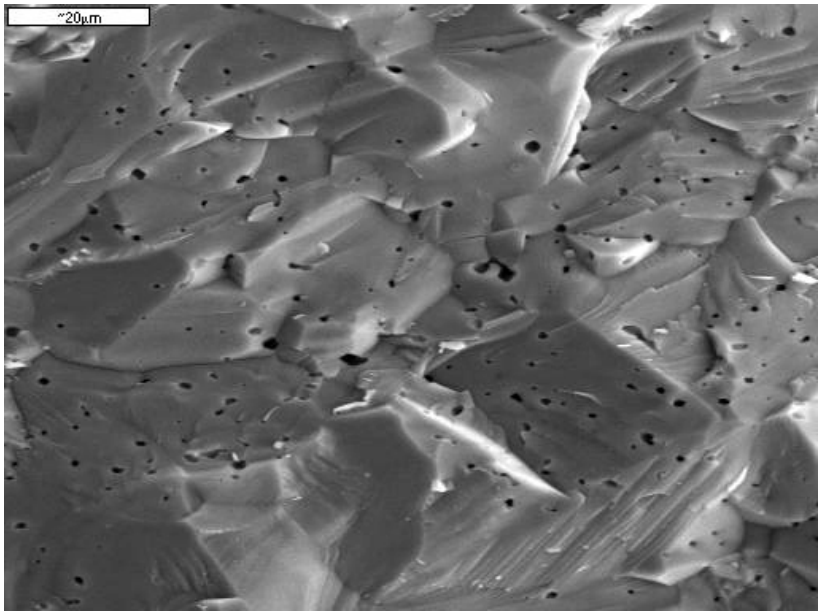

Figure 5.15. SEM fracture surface of an E-type sample sintered in two steps: 1800°C for 2 hrs and 1950°C for another 2 hrs (originally x1000).

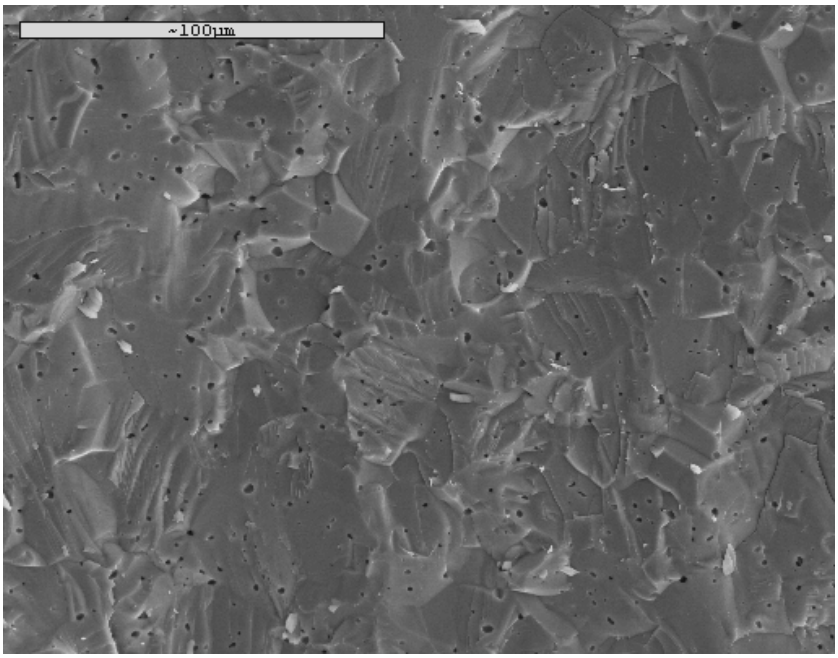

Figure 5.16. SEM fracture surface of an F-type sample sintered at 1950°C for 4 hrs (heating rate of 500 °C/hr, originally x500).

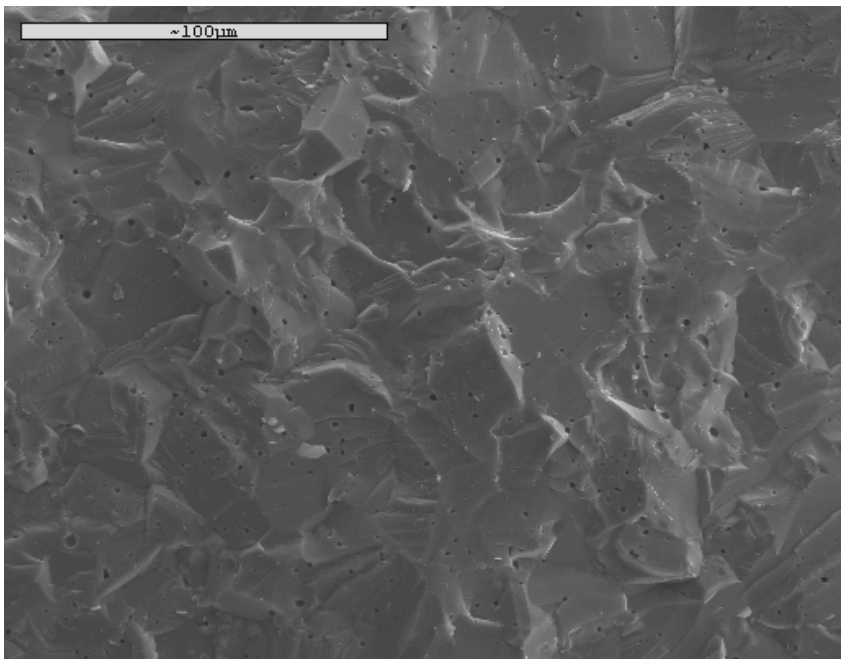

Figure 5.17. SEM fracture surface of an F-type sample sintered at 1950°C for 4 hrs (heating rate of 900 °C/hr, originally x500).

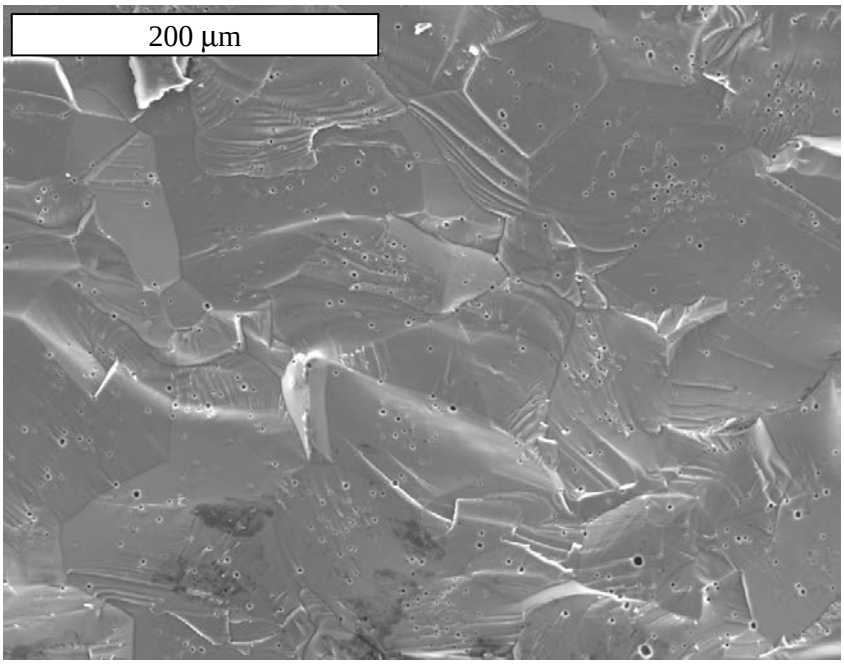

Figure 5.18. SEM fracture surface of an I-type sample sintered at 2000°C for 12 hrs (originally x250).

Adding Mg seems to affect the material: reduce porosity, increase grain size and cause intergranular fracture. Figure 5.19 depicts these effects on the doped AlON. The density of this MA-type sample was 98.5%, compared to 98% of the sample in Figure 5.17 which passed the same sintering route.

The lanthanum doped sample in Figure 5.20 has much larger grains and much less porosity. However, the few pores which are present are quite large and located both in the grains and at grain boundaries.

The fracture surface of an yttrium doped sample (in Figure 5.21) shows even larger pores, even though it was sintered at a higher temperature. Addition of lanthanum to the same composition (in the same sintering process) reduced the porosity abundance and size (see Figure 5.22).

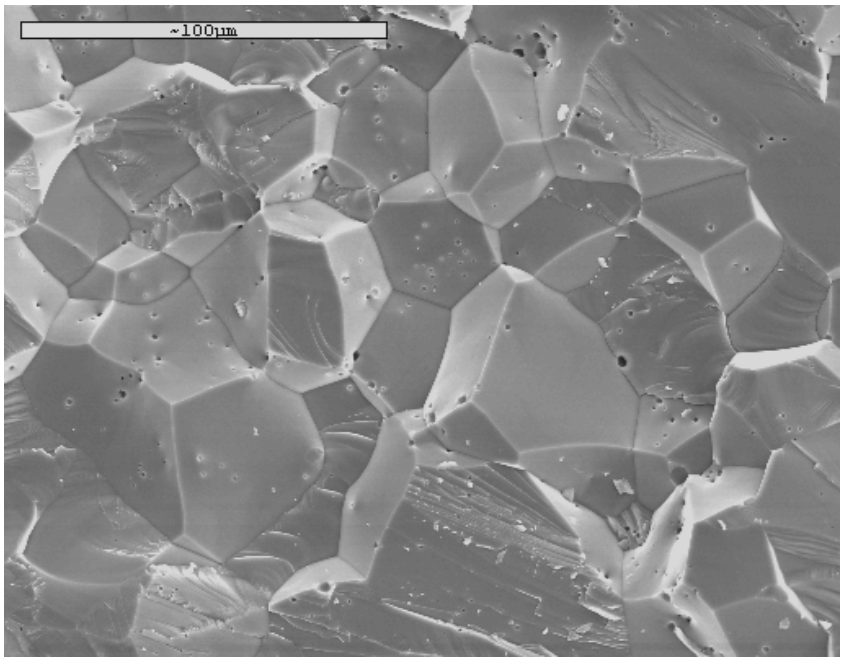

Figure 5.19. SEM fracture surface of an MA-type sample sintered at 1950°C for 4 hrs (originally x500).

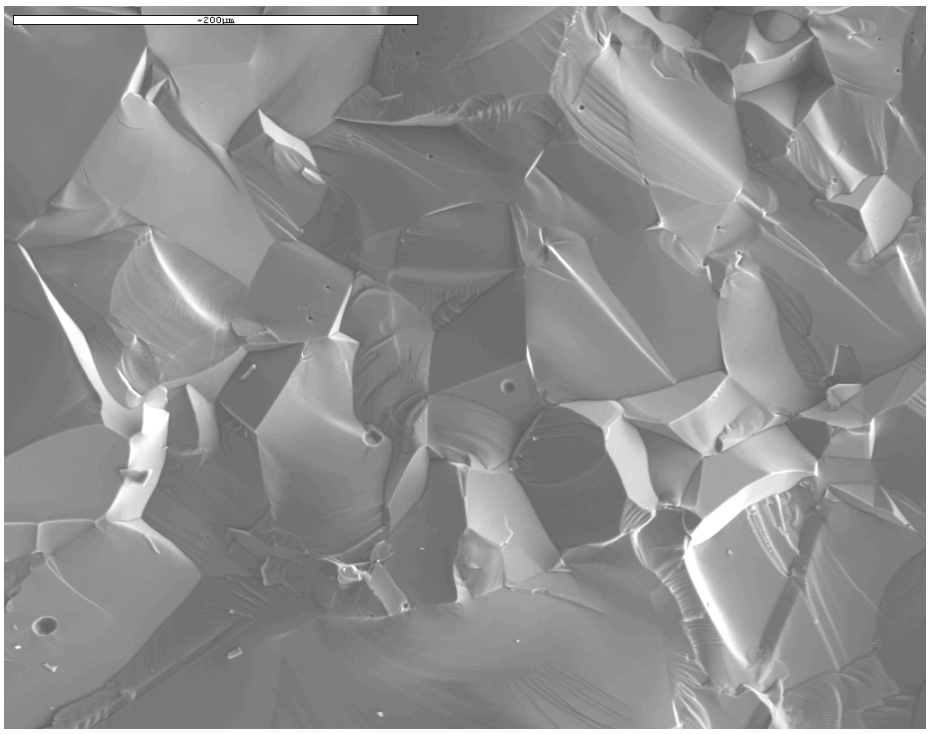

Figure 5.20. SEM fracture surface of an LA-type sample sintered at 1950°C for 12 hrs (originally x250).

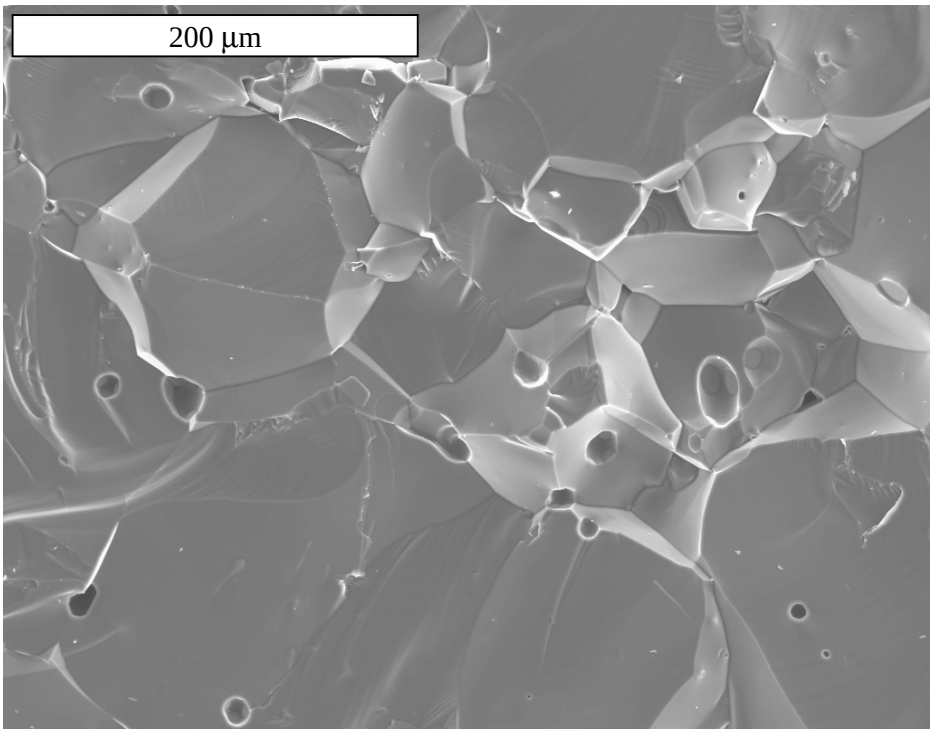

Figure 5.21. SEM fracture surface of a YA-type sample sintered at 2000°C for 12 hrs (originally x250).

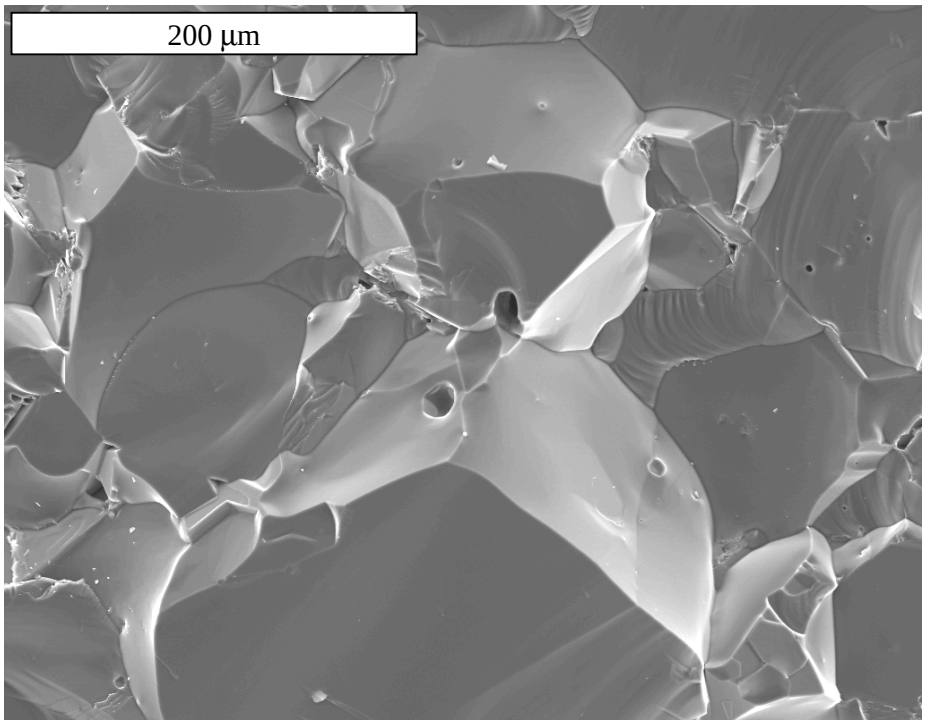

Figure 5.22. SEM fracture surface of a YLA-type sample sintered at 2000°C for 12 hrs (originally x250).

While all the previous micrographs showed homogeneous microstructures of single phase AlON, in the case of MLD samples a secondary phase was discovered both by SEM and XRD. MLD-type AlON contains the largest concentration of lanthanum dopant of all compositions (0.2 wt.%). Figure 5.23 is an elemental map of the fracture surface of an MLD sample sintered at 1950°C for 12 hrs, including secondary and backscattered electron micrographs. One can see a secondary phase at the grain boundaries, which is richer in La and poorer in Al than AlON.

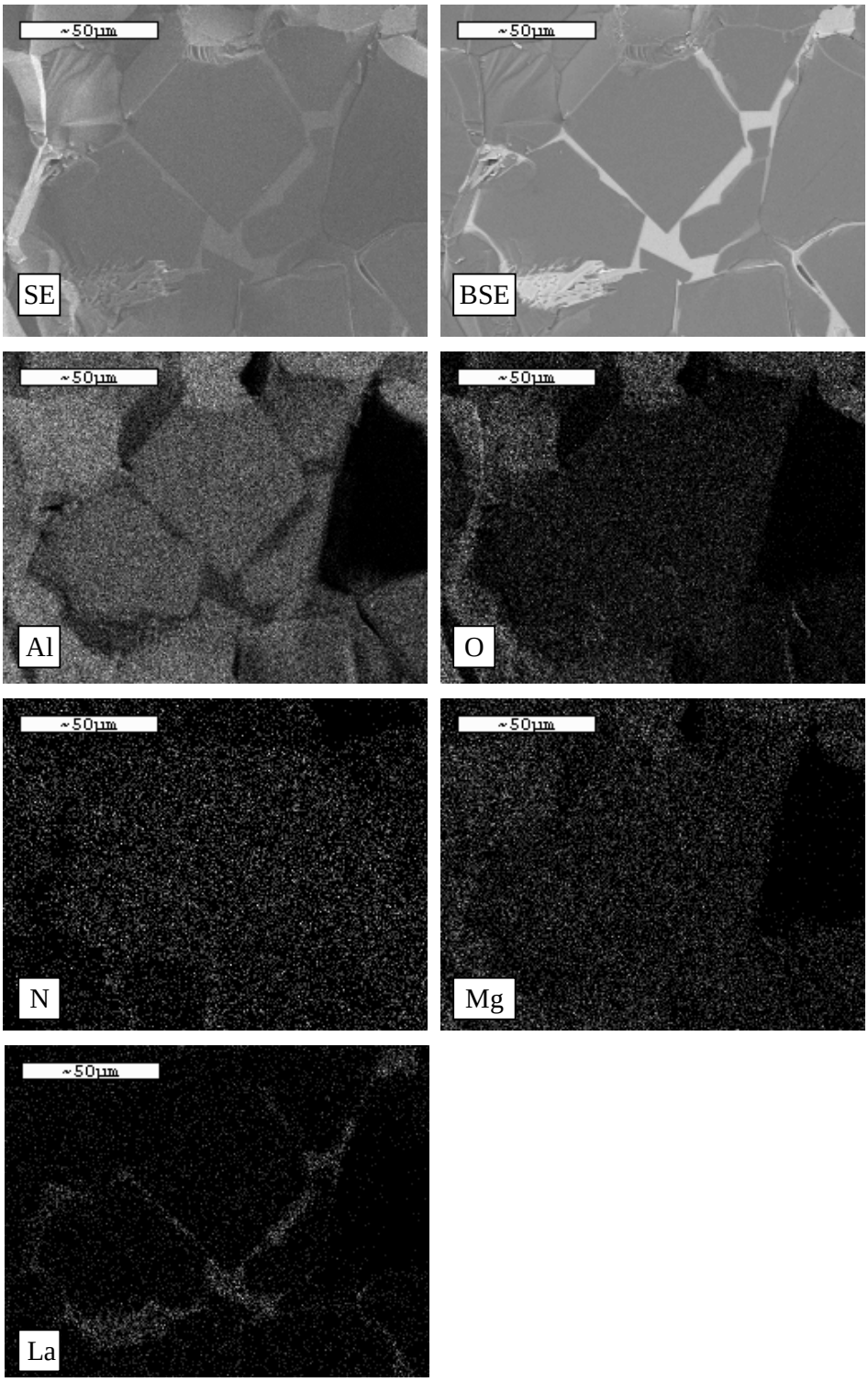

Figure 5.23. Elemental mapping SEM micrographs of a fracture surface of an MLD sample sintered at 1950°C for 12 hrs (originally x500).

XRD analysis of this sample reveals that the secondary phase is lanthanum hexaluminate, $LaAl_{11}O_{18}$ (see Figure 5.24). This explains the results of the element mapping analysis: more lanthanum, less aluminum and approximately the same oxygen content in the boundary as compared to the grains.

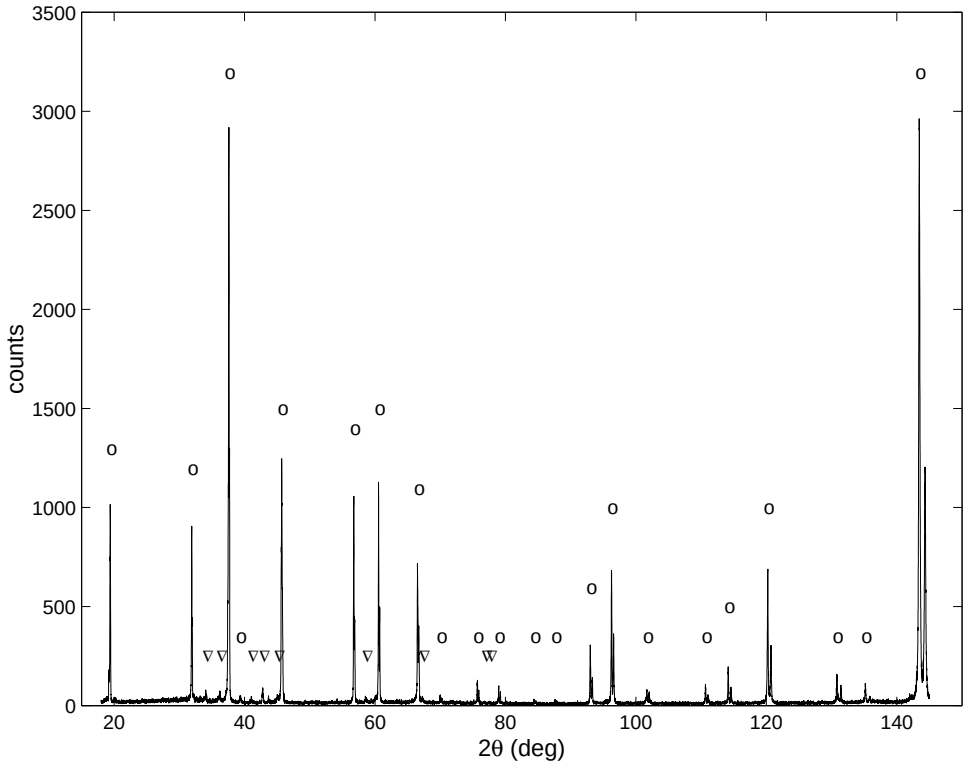

Figure 5.24. XRD of an MLD-type AlON sample sintered at 1950°C for 12 hrs; ○ - AlON , ∇ - $LaAl_{11}O_{18}$.

5.5.3 Grain Size Measurements

Grain size was measured for part of the samples, after they were polished and chemically etched. The measurements were conducted according to the linear intercept procedure described in ASTM E112. In most samples the grains were quite uniform in size, so the average grain size represented the microstructure. The results are given in Table 5.4, along with the type of material and sintering temperature and time. It should be noticed that the measurement errors are quite large (the grain sizes were rounded to tens of microns). This is because distinguishing between adjacent grains was not always easy. Also, counting only 50-100 grains (or practically intercepts) limits the precision of the results.

Table 5.4. Average grain sizes measured for various AlON samples, with different composition types and sintering temperatures and times.

AlON type	Sintering temperature [°C]	Sintering time [hrs]	Average grain size [μm]
F	2025	12	60
H	2025	12	100
I	1950	12	60
J	2000	12	90
J	2010	12	140
MA	1950	12	90
MB	1950	12	80
MB	2010	12	140
MC	2010	12	170
MD	1930	12	60
LA	1930	12	190
YA	2000	12	140
YA	2025	12	70
MLD	2000	12	130
YLA	2000	12	130
YLA	2010	12	170
YLA	2025	12	90
MYA	1930	12	70
MLYA	1930	12	90
Surmet	-	-	170

From the results one can reach the following conclusions:

1. The doped samples have larger grains than the undoped samples.
2. Higher sintering temperature yields larger grains.

While the latter conclusion is a well known characteristic of sintering processes, the first one is directly related to the influence of the dopants on the sintering of AlON. This behavior may indicate that liquid phase sintering is taking place, which enhances diffusion and grain growth. This issue will be further discussed in chapter 6.

5.5.4 TEM Characterization

A sintered sample of MLA-type AlON was examined by TEM, in order to investigate the grain boundaries for any secondary phases or other defects. Despite the relatively large grain size, a grain boundary could be located. Figure 5.25 shows that no secondary phase can be found at the grain boundary. An electron diffraction pattern from an AlON grain of this sample is shown in Figure 5.26. The zone axis is $[1\bar{1}\bar{1}]$. This is another authentication for the cubic symmetry of AlON.

As a comparison, a sample of transparent AlON of Surmet was examined as well. A triple point in this sample is shown in Figure 5.27. Again, the grain boundaries are free of secondary phases, and thus should not scatter light significantly. Figure 5.28 shows the electron diffraction pattern from this sample.

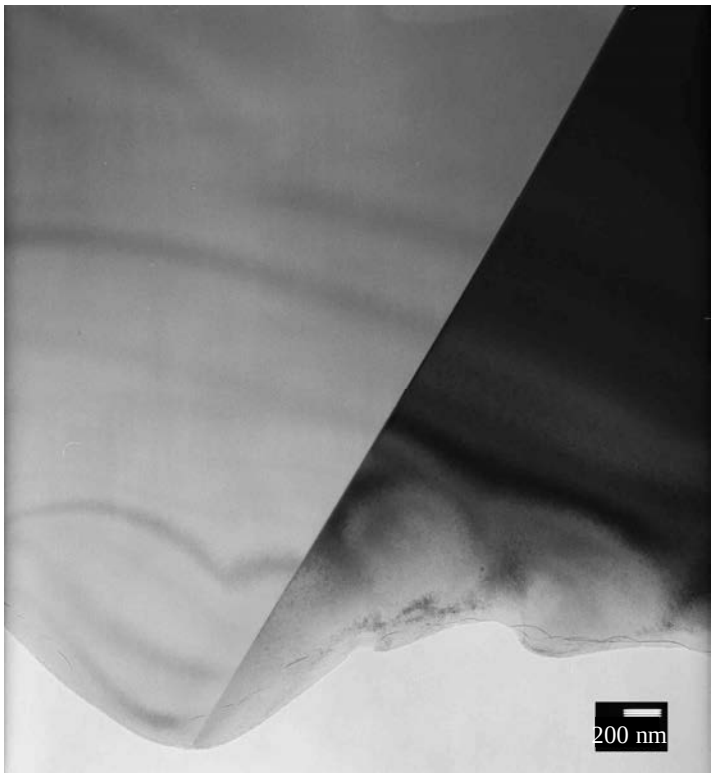

Figure 5.25. TEM micrograph of a grain boundary in an MLA-type sample.

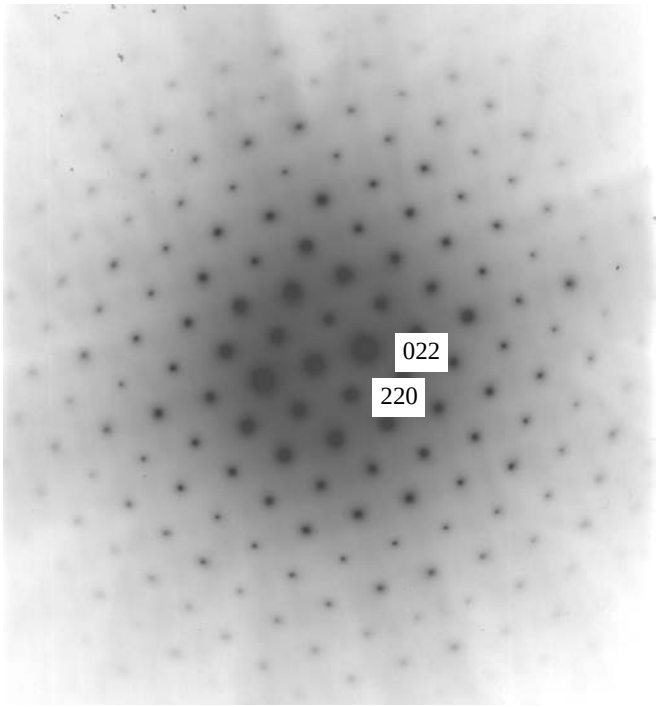

Figure 5.26. Electron diffraction pattern from an AlON grain in an MLA sample.

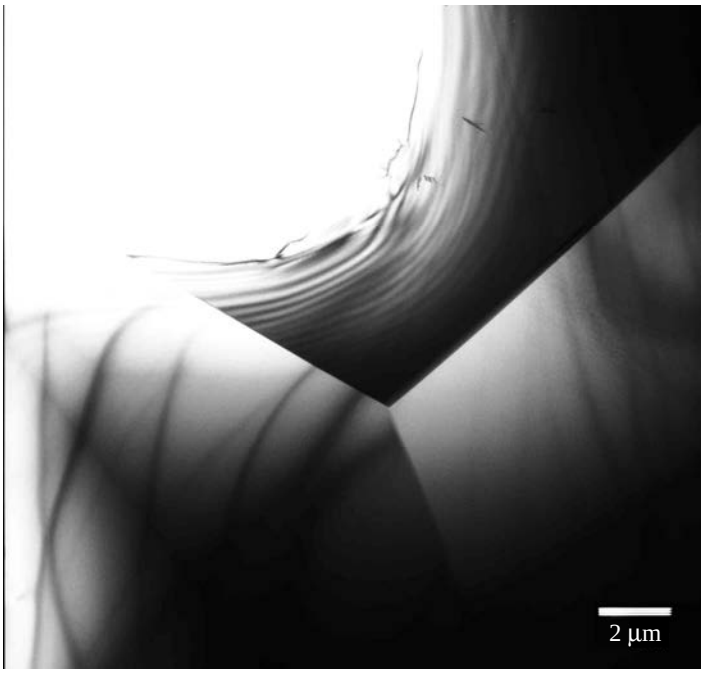

Figure 5.27. TEM micrograph of a triple point in a sample of transparent AlON from Surmet.

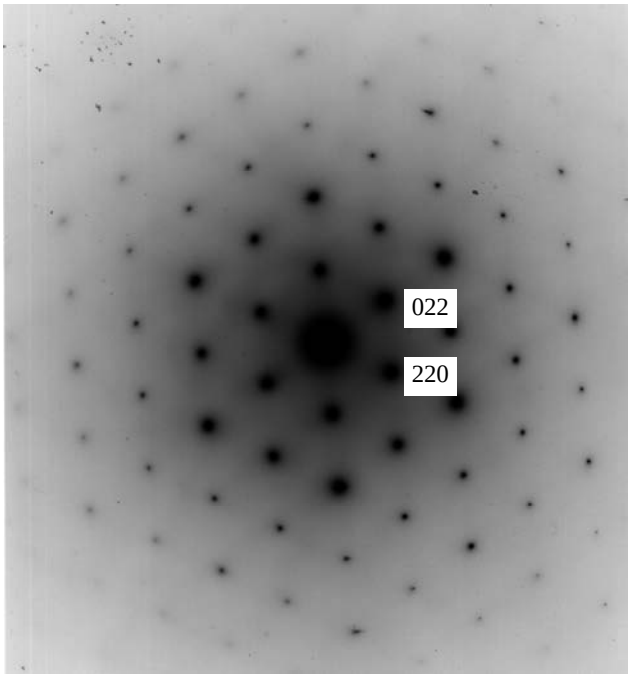

Figure 5.28. Electron diffraction pattern from an AlON grain in a transparent sample from Surmet.

5.6 Light Transmission

Light transmission of the most translucent AlON sample (as chosen by visual examination) was measured in both visible and infrared (IR) regions. The tested sample was MLA-type which was sintered at 2025°C for 12 hrs. A photograph of the AlON sample, lying on a paper where the word "ALON" is written, is shown in Figure 5.29b. Although the text is visible, the sample is only translucent. Figure 5.29a shows the best undoped (F-type) AlON sample prepared, concerning translucency. Looking carefully at these two samples, one can see that the F sample scatters the light more than the MLA sample: the word "ALON" is more blurred for F, and the edges of the letters are sharper for MLA.

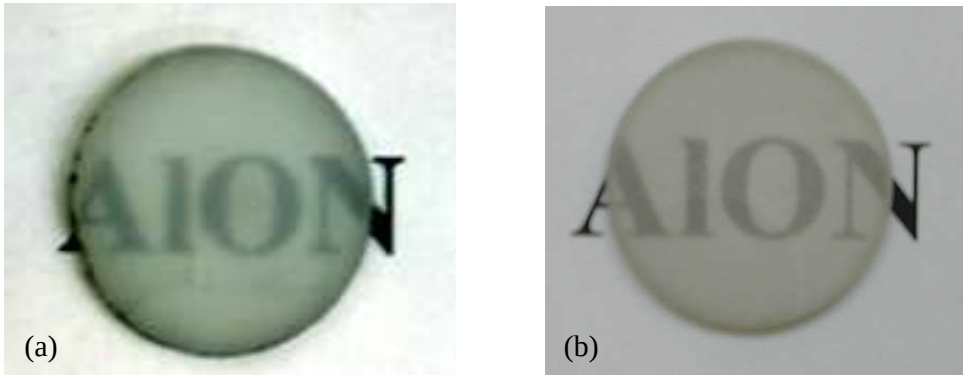

Figure 5.29. Photographs of AlON samples lying on a paper with the word "ALON": a) pure AlON (F-type), sintered at 2025°C for 4 hrs, 1.66 mm thick sample; b) doped AlON (MA-type), sintered at 2025°C for 12 hrs, 2.8 mm thick sample.

At the time the MA sample was tested (after grinding and polishing it to a level of 1 μm), its thickness was 2.8 mm. Figure 5.30 shows the transmission graphs for this MA-type sample, compared to a 6 mm thick transparent AlON plate produced by Surmet, in the UV, visible and IR regions. The transmission measured in the visible region (500 nm) was ~16%, while in the IR it increases up to 25% (at 4 μm).

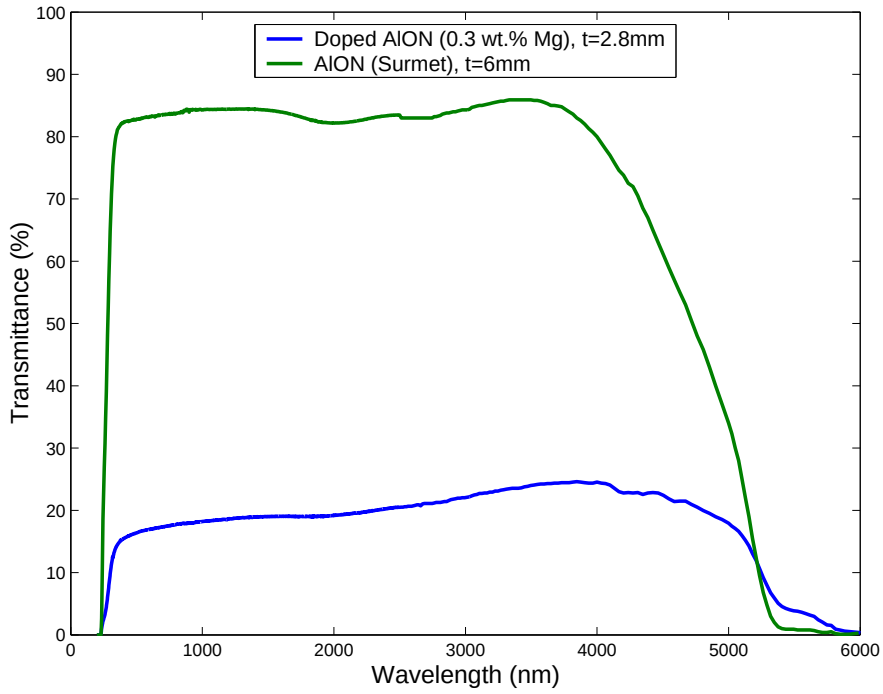

Figure 5.30. Transmission curves of an MA-type AlON sample and the transparent AlON produced by Surmet, in the UV, visible and IR regions.

5.7 Oxidation Resistance Experiment

The oxidation resistance of a transparent AlON sample of Surmet was examined by heating it to an elevated temperature. The experiment included heating the sample to 2000°C at a rate of 500 °C/hr, letting it stay at this temperature for 4 hrs and cooling at 400 °C/hr to room temperature. The sample, which was 6 mm thick, was placed on an AlON (Sienna) powder bed, in a graphite crucible. Flowing nitrogen was used during the whole experiment.

Following the experiment, the lower ~1.5 mm layer of the sample still seemed transparent, while the remainder of the sample turned to be opaque. XRD runs of the upper and lower surfaces of the sample revealed a phase transformation which occurred at the upper (opaque) part but left the lower (transparent) part almost unchanged. Figure 5.31 shows the difference between the diffraction patterns of these two regions. The phase transformation did not significantly alter the microstructure, which is shown in Figure 5.32.

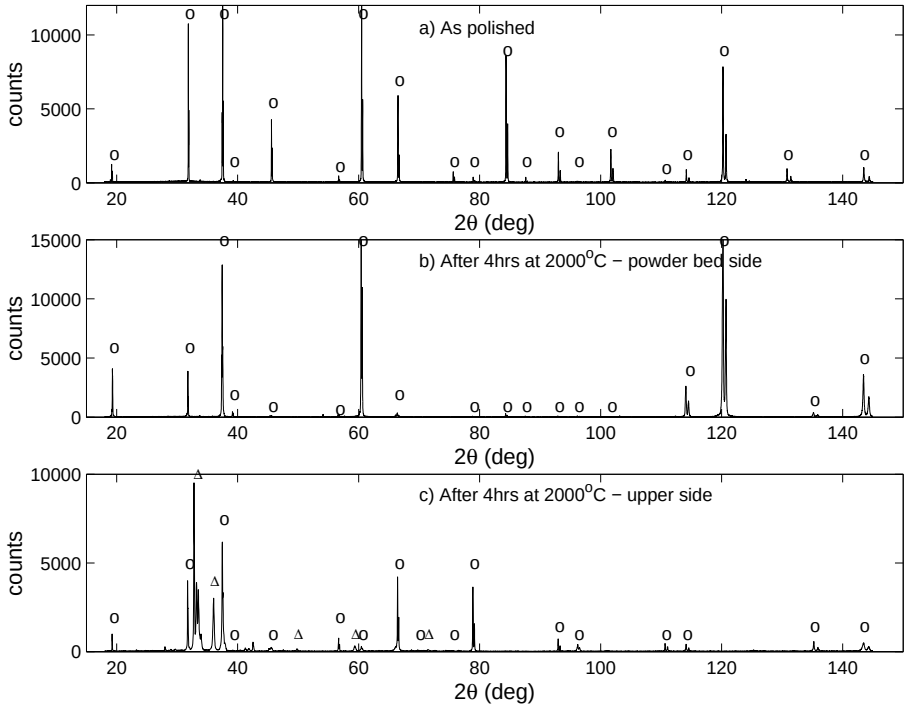

Figure 5.31. XRD runs of an AlON sample of Surmet (which was originally transparent) before and after an oxidation resistance experiment at 2000°C for 4 hrs: a) before the experiment, b) the lower (transparent) part after the experiment, c) the upper (opaque) part after the experiment; ○ - AlON , Δ - AlN.

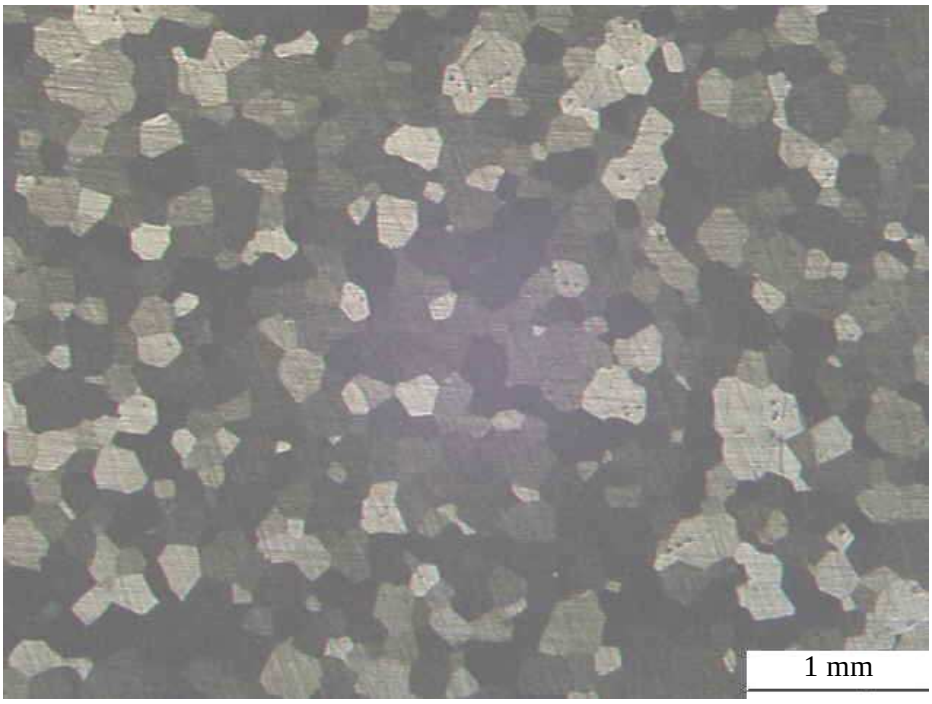

Figure 5.32. Optical micrograph of an etched AlON sample of Surmet after heating at 2000°C for 4 hrs.

5.8 Hardness Measurements

Since most of the possible applications of AlON require high hardness, the hardness of some samples was measured. The results are shown in Table 5.5.

Table 5.5. Knoop hardness measured for various AlON samples, with different composition types and sintering temperatures and times.

AlON type	Sintering temperature [°C]	Sintering time [hrs]	Knoop hardness, 1 kg load [kg/mm^2]
F	2025	12	1520±40
I	1950	12	1350±110
MA	1950	12	1480±70
MB	2000	12	1460±50
MB	2010	12	1420±80
MC	2010	12	1550±70
MD	2010	12	1430±70
LA	2010	12	1420±70
LA	1930	12	1480±70
MLA	2025	4	1540±100
MLA	2025	12	1620±130
YLA	2025	12	1570±30
YLA	2010	12	1530±40
MLYA	2010	12	1460±50
Surmet	-	-	1440±40

The results for the various samples were all concentrated around 1450-1500 kg/mm^2. This value is very close to the hardness measured for the Surmet transparent AlON. It means that the sintered AlON ceramics are hard enough to be used for advanced structural applications. The mixed results suggest that there is no clear influence of the composition and sintering parameters on the hardness.

6. Discussion

The influence of the dopants on the microstructure and transmittance was demonstrated in the previous chapter. One could see that introducing appropriate combination of dopants made it possible to sinter translucent samples, which could not be obtained otherwise. Furthermore, the sintering route should be properly chosen so that the dopants will be most effective. This chapter includes a discussion on the microstructural effects of the sintering process parameters and the various dopants.

6.1 Sintering Process

The pressed powder bodies are composed of Al_2O_3 and AlN powders, with dopants in part of them. Their green density was in most cases in the range of 55-60% of the theoretical density. The dilatometry results (see Figure 5.1) show that sintering begins around 1020-1050°C. This temperature is close to the correspondent one in alumina.[95] The AlON formation reaction was found to take place around 1750-1800°C. This fits the results of Bandyopadhyay *et al.*[51] (see Figure 2.3), which showed significant percents of reaction at sintering temperature of 1720°C, concerning the relatively rapid heating in the dilatometry runs. The results of the powder synthesis experiment conducted at 1750°C, which ended with almost 100% AlON phase, are in agreement with these reaction temperatures as well.

The dopants are added in the form of hydrate salts which are soluble in the ball milling medium (alcohol), to obtain a homogenous distribution. The composition of sintered samples was verified using EDS and WDS (see Table 5.3). No significant inhomogeneities could be observed, except for the samples where La enriched secondary phase was formed.

A very low dopant concentration in AlON can cause the formation of a liquid phase at a lower temperature than the liquidus of AlON. For example, Figure 6.1 shows the phase diagram of the La_2O_3-Al_2O_3 system. Assuming that the La poor side of the diagram is similar for Al_2O_3 and AlON, one can see that a liquid phase is formed already at 1930°C. Lacking the real phase diagrams of AlON with the dopants used,

only the final state of the samples can indicate whether there was a liquid phase or not.

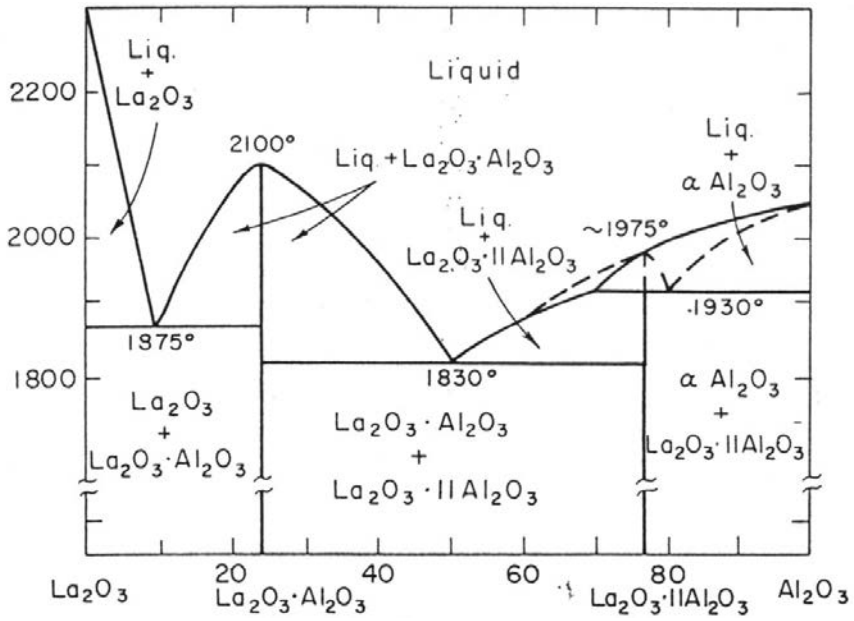

Figure 6.1. Phase diagram of the La_2O_3-Al_2O_3 quasi-binary system above 1800°C.

6.2 Description of the Dopant Effects

A liquid phase dopant for AlON must have a low viscosity for rapid diffusion kinetics, and good wetting on AlON to allow easy penetration between the AlON grains.[30] The liquid reaches the contacts between AlON particles and forms a meniscus. At this stage AlON particles can rearrange rapidly into a higher density packing configuration. This rearrangement may be the reason for the smaller expansion of AlON during its formation reaction, which was seen for the doped sample relative to the undoped one (see Figures 5.1 and 5.2). Further densification takes place by flattening of the liquid contacts under the compressive stress applied by capillary pressure. The thin liquid film then serves as a path of rapid transport, like grain boundaries. After some densification the grains may be mostly surrounded by liquid, the thickness of which is determined by the additive concentration.

The process of densification involves removing grain boundary pores by grain boundary or liquid phase diffusion of vacancies from the pore surface. Pores which are located within AlON grains cannot be removed because of the very low lattice diffusion rates. Thus, pore entrapment must be completely prevented in order to achieve transparency. The fracture surface micrographs showed that in doped samples most of the residual pores are located at grain boundaries, as opposed to undoped samples which contain both grain boundary and bulk porosity (see Figures 5.19 and 5.21, for example). The mechanism by which the dopants act may be similar to that of Mg in translucent alumina (Lucalox).[56] Although this mechanism is not fully understood, it apparently involves the reduction of grain boundary mobility because of the segregation of dopants to grain boundaries. This slows grain growth and allows the pores to remain attached to boundaries, from where they can be removed by grain boundary diffusion.

If this is the case, a very thin layer of dopants should be present at the grain boundaries. TEM examination of a grain boundary in one of the samples with low dopant concentration did not show any foreign materials. The WDS results shown in Table 5.3 indicated that almost all the dopant content went into solid solution with AlON and was uniformly distributed within the grains. Still, part of the dopants might remain at the grain boundaries, at segregation levels below the detection limit of EDS in conventional TEM. If we assume that all the grains are spherical with a diameter of 150 μm and every grain is surrounded by a dopant monolayer (say, 0.3 nm thick), the contribution of this monolayer to the total dopant concentration is of the order of ~0.001 wt.%. Only analytical high-resolution FEG-TEM can assist in determining whether this monolayer exists or not.

6.3 Influence of Dopants on the Microstructure

It was clearly shown that the denser the microstructure of AlON the more translucent is the sample. The improvement in transparency is mainly achieved by reduced porosity. This can be obtained by slowing down grain growth and letting the pores move rapidly, to remain attached to the moving grain boundaries. A pore which cannot catch up with the grain boundary will stay behind occluded within an AlON

grain, from where it is hard to remove. Thus, the desired role of the dopant is to make this scenario possible.

The typical microstructure of AlON samples sintered at high temperatures (>2000°C) for long times (12 hrs) contains relatively large grains (~150 μm). This is also the typical grain size reported in the literature.[38,74,78] The grain size was found to depend mainly on the sintering temperature, but also on the composition (doped or undoped AlON). In some cases the micrographs of etched samples showed small pits which were scattered throughout the fine ground surface. This phenomenon was seen before by Burns *et al.*,[96] who worked on adjusting grinding process parameters. In the fracture surface micrographs, evidences of cleavage planes can be seen (see Figures 5.20 and 5.22, for example), which were also reported elsewhere for the AlON from Raytheon.[78] In general, the doped samples fractured more intergranularly than the undoped sample, which is an indication for weaker grain boundaries in doped AlON. This can be related to dopants which remained at the grain boundaries.

The optical and SEM micrographs showed that all three dopants significantly reduced porosity. Moreover, the residual porosity tended to be at the grain boundaries rather than within grains, which means that longer sintering time could assist in removing the pores by grain boundary diffusion. However, each dopant had a further different effect on the microstructure of AlON.

It was observed that Y leaves behind very large pores, some of them even tens of microns sized. This characterized the fracture surfaces of samples doped with Y alone or with Y and La. This may be the crucial factor which made these samples opaque. On the other hand, Mg and La dopants, which yielded the most porosity-free microstructures, allowed AlON to be translucent. If one looks closely at the most translucent samples by the naked eye, many microscopic defects can be seen within them. These could not be attributed to any specific microstructural feature but were undoubtedly scattering centers with reduced transparency. The differences in the influence of Y and La, which are situated in the same column in the periodic table of the elements, are not clear. The explanation may be related to the higher Y concentration utilized or a smaller increase of the grain boundary diffusion rate,

which is the mechanism responsible for pore elimination, in the case of a Y liquid phase.

All samples which contained any amount of La, including those with only 0.02 wt.% La, showed extensive twinning in their etched optical micrographs. This phenomenon was not investigated, and the reason for it is still unknown. It may be the result of a reduction in the stacking fault energy caused for some reason by La.

All samples with at least 0.1 wt.% La were found to have a second phase, which was identified by XRD to be $LaAl_{11}O_{18}$. This phase was never observed in samples with only 0.02 wt.%. Thus, it can be concluded that the solubility limit of La in AlON is somewhere in the range of 0.02-0.1 wt.%. The secondary phase was found in the form of isolated islands situated distantly from each other, at grain boundaries. The presence of such islands increases light scattering, apparently because the refractive index of the secondary phase is different from that of AlON.

The dopants themselves may act as scattering centers, being foreign materials that were introduced, and thus play the opposite role of the original goal. However, it should be remembered that the dopant contents are relatively low. Also, the transparent samples sintered by Hartnett *et al.*[47] using Y and La contents of 0.08 and 0.02 wt.%, respectively, show that the scattering caused by the dopants is unimportant. This cannot be claimed for Mg, which was added in larger quantities (0.3 wt.%). Anyway, in the current study the light scattering due to porosity is undoubtedly much higher than any absorption or scattering caused by the dopant atoms.

The results suggest that dopants do not have a significant influence on the hardness. This is not surprising, because there were no large differences in the porosities and phase content. The hardness obtained was close to the reported values, such as in Table 2.4, and to transparent AlON, because it is the same phase.

7. Summary and Conclusions

The improvement of light transmittance of AlON due to sintering additives was demonstrated. The introduction of Mg and La dopants causes the formation of a liquid phase at the high sintering temperature. This promotes pores removal through grain boundary diffusion, which results in a material with almost 100% density. While the microstructure of undoped AlON samples is composed of many pores which are distributed everywhere in the material, doped AlON samples, sintered at the same conditions, contains much fewer pores which are mainly situated at the grain boundaries. Since porosity is the main scattering source in transparent ceramics in general, and particularly in AlON, its reduction turned the material from white colored to translucent. The highest transmission was achieved in a sample doped with 0.3 wt.% Mg (and optionally also 0.02 wt.% La), which was sintered at 2025°C for 12 hrs.

The sintering parameters were found to influence the microstructure and transparency. Even though single phase AlON was sintered at only 1800°C for 4 hrs, high temperatures (>2000°C) and long times (12 hrs) were required for sintering the best samples, in terms of transparency. This is the result of a more effective pore removal achieved with these conditions, and larger grain sizes (~150 μm).

The influence of Y dopant was also investigated, and it was found to form relatively large pores. This kind of microstructure does not allow for light transmission. However, it should be mentioned that only 0.08 wt. Y was added, thus the influence of higher concentrations should be checked in the future.

8. Recommendations for Future Work

Many issues in the research subject are still open. At least part of them will be listed in this chapter.

First of all, it is not clear that the dopants chosen for the current study are the only ones that can improve transparency. Other additives should be considered as well.
Second, the dopant concentrations used in this research could not map the whole relevant ranges (up to the solubility limit) of the three dopants. Thus, the optimal dopant concentrations can be other than used.

It was shown that the longer the sintering process was, the closer the AlON was to 100% density. Thus, a very long (24-48 hrs) sintering route should be utilized to let all the porosity diffuse outward from the AlON. Another potentially useful way to close the residual porosity is to hot isostatic press (HIP) the sintered AlON.

The process chosen for this study, reaction sintering, involves alumina and AlN raw powders. Since there is no available ultrapure submicron AlN powder, the reaction between the powders is not optimal. Other processes, such as carbothermal nitridation of alumina, do not need AlN as one of the raw materials, thus may yield better results. Additionally, microwave processing has shown encouraging results in other works reported in the literature, and it may be considered too.

In order to achieve a better understanding on the process of AlON liquid phase sintering, a high resolution TEM study of the grain boundaries and especially the triple points should be conducted. This will reveal where the dopants are located at the end of the process, and give more indications on the role of the dopants during sintering stage.

9. References

1. Yamaguchi, G. & Yanagida, H., Study on the reductive spinel - a new spinel formula $AlN\text{-}Al_2O_3$ instead of the previous one Al_3O_4, *J. Chem. Soc. Japan*, **32** (1959) 1264-1265.
2. Long, G. & Foster, L. M., Crystal phases in the system Al_2O_3-AlN, *J. Am. Ceram. Soc.*, **44** (1961) 255-258.
3. Collongues, R., Gilles, J. C. & Lejus, A.M., Action de l' ammoniac sur différents oxides super-réfractaires, *Bull. Soc. Chim. Fr.*, **11-12** (1962) 2113-2117.
4. Adams, I., AuCoin, T. R. & wolff, G. A., Luminescence in the system Al_2O_3-AlN, *J. Electrochem. Soc.*, **109** (1962) 1050-1054.
5. Lejus, A. M., Préparation par réaction à l'etat solide et principales propriétés des oxynitrures d'aluminium, *Bull. Soc. Chim, Fr.*, **11-12** (1962) 2123-2126.
6. Lejus, A. M., Formation at high temperature of nonstoichiometric spinels and of derived phases in several oxide systems based on alumina and in the system alumina-aluminum nitride, *Rev. Int. Hautes Tempér et Réfract*, **1** (1964) 53-95.
7. Gilles, J. D., Formation d'owynitrures a partir des oxides réfractaires, *Rev. Hautes Tempér et Réfract*, **2** (1965) 237-262.
8. Collongues, R., Gilles, J. C., Lejus, A. M., Perez y Jorba, M. & Michel, D., Recherches sur les oxynitrures metalliques, *Mat. Res. Bull.*, **2** (1967) 837-848.
9. Michel, D. & Huber, M., Étude sur monocristaux de l'ordonnancement des defaults dans l'oxynitrure d'aluminium δ, *Rev. Hautes Tempér et Réfract*, **7** (1970) 145-150.
10. Michel, D., Contribution a l'étude de phénomènes d'ordonnancement de defaults dans des monocristaux de matériaux réfractaires a base d'alumine et de zircone, *Rev. Hautes Tempér et Réfract*, **9** (1972) 225-242.
11. Lefebre, A., Gilles, J. C. & Collongues, R., Antiphases périodiques dans un spinelle non-stoechiometrique ($9Al_2O_3$-AlN) prepare a haute temperature, *Mat. Res. Bull.*, **7** (1972) 557-566.
12. Gauckler, L. J. & Petzow, G., Representation of multicomponent silicon nitride based systems, In Nitrogen Ceramics, The Netherlands: Noordhoff Publishing Co., edited by F. L. Riley, 1977, p. 41-60.
13. Sakai, T., Hot pressing of the $AlN\text{-}Al_2O_3$ system, *J. Ceram. Assoc. Japan (Yogyo-Kyokai-shi)*, **86** (1978) 125-130.
14. Sakai, T., High temperature strength of AlN hot-pressed with Al_2O_3 additions, *J. Am. Ceram. Soc.*, **64** (1981) 135-137.
15. McCauley, J. W. & Corbin, N. D., Phase relations and reaction sintering of transparent cubic aluminum oxynitride spinel (ALON), *J. Am. Ceram. Soc.*, **62** (1979) 476-479.
16. McCauley , J. W. & Corbin, N. D., High temperature reactions and microstructure in the Al_2O_3-AlN system, In *Progress in Nitrogen Ceramics*, edited by F. L. Riley (Martinus Nijhoff, The Netherlands, 1983), p. 111-118.
17. Willems, H. X., Hendrix, M. M. R. M., Metselaar, R. & de With, G., Thermodynamics of Alon I: stability at lower temperatures, *J. Eur. Ceram. Soc.*, **10** (1992) 327-337.
18. Tabary, P. & Servant, C., Thermodynamic reassessment of the $AlN\text{-}Al_2O_3$ system, *Calphad*, **22** [2] (1998) 179-201.
19. Wang, X., Li, W. & Seetharaman, S., Thermodynamic study and synthesis of γ-aluminum oxynitride, *Scandinavian Journal of Metallurgy*, **31** (2002) 1-6.
20. Nakao, W., Fukuyama, H. & Nagata, K., Thermodynamic stability of γ-aluminum oxynitride, *J. Electrochem. Soc.*, **150** (2003) J1-J7.
21. Takebe, H., Kameda, T., Komatsu, M., Komeya, K. & Morinaga, K., Fabrication of translucent sintered aluminum oxynitride spinel (AlON), *J. Ceram. Soc. Jpn. Inter. Edn.*, **97** (1989) 166-173.

22. Tabary, P., Servant, C. & Alary, J. A., Microstructure and phase transformations in the AlN-Al_2O_3 pseudo-binary system, *J. Eur. Ceram. Soc.*, **20** (2000) 913-926.
23. Sappei, J., Goeuriot, P., Thévenot, F., Laurent, Y., Guyader, J. & L'Harridon, P., Alumina-γ-aluminum oxynitride composites from alumina nitrided by ammonia, *J. Eur. Ceram. Soc.*, **8** (1991) 257-262.
24. Irene, E. A., Silvestri, V. J. & Woolhouse, G. R., Some properties of chemically vapor deposited films of $Al_xO_yN_z$ on silicon, *J. Electronic Mat.*, **4** (1975) 409.
25. Silvestri, V. J., Irene, E. A., Zirinsky, S. & Kuptsis, J. D., Chemical vapor deposition of $Al_xO_yN_z$ films, *J. Electronic Mat.*, **4** (1975) 429-444.
26. Corbin, N. D., Aluminum oxynitride spinel: a review, *J. Eur. Ceram. Soc.*, **5** (1989) 143-154.
27. Tabary, P. & Servant, C., Crystalline and microstructure study of the AlN-Al_2O_3 section in the Al-N-O system, I. Polytypes and γ-Alon spinel phase, *J. Appl. Cryst.*, **32** (1999) 241-252.
28. Goursat, P., Billey, M. Goeuriot, P., Labbe, J. C., Villechenoux, J. M., Roult, G. & Bardolle, J., Contribution a l'etude du systeme AL/O/N II – retention d'azote dans les produits d'oxynitrure d'aluminum-γ, *Mat. Chem.*, **6** (1981) 81-94.
29. Goursat, P., Goeuriot, P. & Billy, M., Contribution a l'etude du systeme AL/O/N I – rèactivite de l'oxynitrure d'aluminum-γ, *Mat. Chem.*, **1** (1976) 131-149.
30. Chiang, Y-M, Birnie, D. III & Kingery, W. D., Physical Ceramics – principles for ceramic science and engineering, The MIT series in materials science & engineering, John Wiley & Sons, Inc., 1997.
31. Sickafus, K. E., Wills, J. M. and Grimes, N. W., Structure of spinel, *J. Am. Ceram. Soc.*, **82** (1999) 3279-3292.
32. Willems, H. X., Translucent γ-aluminium oxynitride, PhD Thesis Technische Universiteit Eindhoven, The Netherlands, 1992.
33. McCauley, J. W., A simple model for aluminum oxynitride spinels, *J. Am. Ceram. Soc.*, **61** (1978) 372-373.
34. Dravid, V. P., Sutliff, J. A., Westwood, A. D., Notis, M. R. & Lyman, C. E., On the space group of aluminium oxynitride spinel, *Phil. Mag. A*, **61** (1990) 417-434.
35. Willems, H. X., De With, G., Metselaar, R., Helmholdt, R. B. & Petersen, K. K., Neutron diffraction of γ-aluminium oxynitride, *J. Mater. Sci. Lett.*, **12** (1993) 1470-1472.
36. Fang, C. M., Metselaar, R., Hintzen, H. T. & de With, G., Structure models for γ-aluminum oxynitride from ab initio calculations, *J. Am. Ceram. Soc.*, **84** (2001) 2633-2637.
37. Willems, H. X., Hendrix, M. M. R. M., de With, G. & Metselaar, R., Thermodynamics of Alon II: phase relations, *J. Eur. Ceram. Soc.*, **10** (1992) 339-346.
38. Hartnett, T. M., Bernstein, S. D., Maguire, E. A. & Tustison, R. W., Optical properties of ALON (aluminum oxynitride), *Proc. SPIE*, **3060** (1997) 284-295.
39. Chen, C. F., Savrun, E. & Ramirez, A. F., Densification and phase transformation of pressureless reactive sintered ALON ceramics, In *Ceramics Today – Tomorrow's Ceramics*, edited by P. Vincenzini (Elsevier, Amsterdam, 1991), p. 1295-1309.
40. Corbin, N. D. & McCauley, J. W., Nitrogen-stabilized aluminum oxide spinel (ALON), *Proc. SPIE*, **297** (1981) 19-23.
41. Rafaniello, W. & Cutler, I. B., Preparation of sinterable cubic aluminum oxynitride by the carbothermal nitridation of aluminum oxide, *Comm. Am. Ceram. Soc.*, **64** (1981) C-128.
42. Ish-Shalom, M., Formation of aluminium oxynitride by carbothermal reduction of aluminium oxide in nitrogen, *J. Mater. Sci. Lett.*, **1** (1982) 147-149.
43. Zheng, J. & Forslund, B., Carbothermal synthesis of aluminum oxynitride (ALON) powder: influence of starting materials and synthesis parameters, *J. Eur. Ceram. Soc.*, **15** (1995) 1087-1100.

44. Yawei, L., Nan, L. & Runzhang, Y., The formation and stability of γ-aluminium oxynitride spinel in the carbothermal reduction and reaction sintering processes, *J. Mater. Sci.*, **32** (1997) 979-982.
45. Yawei, L., Nan, L. & Runzhang, Y., Carbothermal synthesis of aluminium oxynitride spinel powders at low temperatures, *J. Mater. Sci. Lett.*, **16** (1997) 185-186.
46. Yawei, L., Nan, L. & Runzhang, Y., Effect of raw materials on carbothermal reduction synthesis of γ-aluminum oxynitride spinel powder, *J. Mater. Sci.*, **34** (1999) 2547-2552.
47. Hartnett, T. M., Gentilman, R. L. & Maguire, E. A., Aluminum oxynitride having improved optical characteristics and method of manufacture, US Patent No. 4481300 (1984).
48. Maguire, E. A., Hartnett, T. M. & Gentilman, R. L., Method of producing aluminum oxynitride having improved optical characteristics, US Patent No. 4686070 (1987).
49. Turpin-Launay, D., Thevenot, F., Delvoye, F. & Boch, P., Reactive hot-pressing of γ aluminum oxynitride, *Mat. Sci. Monogr.*, **16** (1983) 891-897.
50. Gentilman, R., Maguire, E., Kohane, T. & Valentine, D. B., Comparison of large ALON and sapphire windows, *Proc. SPIE*, **1112** (1989) 31-39.
51. Bandyopadhyay, S., Rixecker, G., Aldinger, F., Pal, S., Mukherjee, K. & Maiti, S., Effect of reaction parameters on γ-AlON formation from Al_2O_3 and AlN, *J. Am. Ceram. Soc.*, **85** (2002) 1010-1012.
52. Gentilman, R. L., Maguire, E. A. & Dolhert, L. E., Transparent aluminum oxynitride and method of manufacture, US Patent No. 4520116 (1985).
53. Martin, C. & Calès, B., Synthesis and hot pressing of transparent aluminum oxynitride, *Proc. SPIE*, **1112** (1989) 20-24.
54. Lefort, P., Ado, G. & Billy, M., High-temperature environmental effects on mechanical properties of transparent aluminium oxynitride, *Science of Ceramics*, **14** (1988) 697-702.
55. Cheng, J., Agrawal, D. & Roy, R., Microwave synthesis of aluminum oxynitride (ALON), *J. Mater. Sci. Lett.*, **18** (1999) 1989-1990.
56. Cheng, J., Agrawal, D., Zhang, Y., Drawl, B. & Roy, R., Fabricating transparent ceramics by microwave sintering, *Am. Ceram. Soc. Bull.*, **79** (2000) 71-74.
57. Cheng, J., Agrawal, D., Zhang, Y. & Roy, R., Microwave sintering to fully transparent aluminum oxynitride (ALON) ceramics, *J. Mater. Sci. Lett.*, **20** (2001) 77-79.
58. Cai, K. F., McLachlan, D. S. & Sigalas, I., Preparation of Al_2O_3-AlON and Al_2O_3-AlN composites via reaction-bonding, *J. Mater. Sci. Lett.*, **20** (2001) 193-195.
59. Launay, D., Orange, G., Goeuriot, P., Thevenot, F. & Fantozzi, G., Reaction-sintering of an Al_2O_3-AlON composite determination of mechanical properties, *J. Mater. Sci. Lett.*, **3** (1984) 890-892.
60. Coble, R. L., Transparent alumina and method of preparation, US Patent No. 3026210 (1962).
61. Grimm, N., Scott, G. E. & Sibold, J. D., Infrared transmission properties of high density alumina, *Ceram. Bull.*, **50** (1971) 962-965.
62. Burke, J. E., Control of grain boundary mobility, In *Sintering of Advanced Ceramics*, vol. 7 (American Ceramic Society, Westerville, Ohio, 1990), p. 215-228.
63. Burke, J. E., Lucalox alumina: the ceramic that revolutionized outdoor lighting, *MRS bull.* (June 1996) 61-68.
64. Peelan, J. G. J., Influence of MgO on the evolution of the microstructure of Al_2O_3, *Mater. Sci. Res.*, **10** (1975) 443-453.
65. Wei, G. C. & Rhodes, W. H., Sintering of translucent alumina in a nitrogen-hydrogen gas atmosphere, *J. Am. Ceram. Soc.*, **83** (2000) 1641-1648.
66. Kaneno, M. & Oda, I., Effect of the properties of translucent alumina tube on lamp efficiency of high pressure sodium lamp, *Mat. Sci. Monogr.*, **6** (1979) 1114-1122.

67. Krell, A., Blank, P., Ma, H., Hutzler, T., van Bruggen, M. P. B. & Apetz, R., Transparent sintered corundum with high hardness and strength, *J. Am. Ceram. Soc.*, **86** (2003) 12-18.
68. Aurial, A. & Tritten, P., Process for the manufacture of articles of transparent alumina, US Patent No. 4031177 (1977).
69. Kobayashi, K. & Kaneno, M., Utilizing mixtures of yttria, magnesia, and lanthanum oxide in manufacture of transparent alumina, US Patent No. 3792142 (1974).
70. Quinn, G. D., Corbin, N. D. & McCauley, J. W., Thermomechanical properties of aluminum oxynitride spinel, *Ceram. Bull.*, **63** (1984) 723-729.
71. Graham, E. K., Munly, W. C., McCauley, J. W. & Corbin, N. D., Elastic properties of polycrystalline aluminum oxynitride spinel and their dependence on pressure, temperature, and composition, *J. Am. Ceram. Soc.*, **71** (1988) 807-812.
72. Willems, H. X., Van Hal, P. F., de With, G. & Metselaar, R., Mechanical properties of γ-aluminium oxynitride, *J. Mater. Sci.*, **28** (1993) 6185-6189.
73. Hartnett, T. M., Maguire, E. A., Gentilman, R. L., Corbin, N. D. & McCauley, J. W., Aluminum oxynitride spinel (ALON) – a new optical and multimode window material, *Ceram. Eng. Sci. Proc.*, **3** (1982) 67-76.
74. Hartnett, T. M. & Gentilman, R. L., Optical and mechanical properties of highly transparent spinel and ALON domes, *Proc. SPIE*, **505** (1984) 15-22.
75. Maguire, E. A., Rawson, J. K. & Tustison, R. W., Aluminum oxynitride's resistance to impact and erosion, *Proc. SPIE*, **2286** (1994) 26-32.
76. Swab, J., J., LaSalvia, J. C., Gilde, G. A., Patel, P. J. & Motyka, M. J., Transparent armor ceramics: AlON and spinel, *Ceram. Eng. Sci. Proc.*, **20** (1999) 79-84.
77. Harris, D. C., Infrared window and dome materials, SPIE Tutorial Texts Series, 1992.
78. Patel, P. J., Swab, J. J., Gilde, G., Fracture properties and behavior of transparent ceramics, *Proc. SPIE*, **4102** (2000) 15-23.
79. McCauley, J. W., Structure and properties of aluminum nitride and AlON ceramics, U.S. Army Research Laboratory, Aberdeen Proving Ground, MD 21005-5069, Report No. ARL-TR-2740, May 2002.
80. Cazamias, J. U., Bless, S. J., Simha, C. H. M. & Hartnett, T. M., Dynamic failure of a transparent polycrystalline ceramic, *Shock compression of condensed matter – 1999*, edited by M. D. Furnish, L. C. Chhabildas and R. S. Hixson (2000), p. 611-614.
81. Cazamias, J. U. & Bless, J., Bar experiments on transparent materials, 18th International Symposium on Ballistics (1999) 724-730.
82. Goldman, L. M., Hartnett, T. M., Wahl, J. M., Ondercin, R. J. & Olson, K., Recent advances in aluminum oxynitride (ALON) optical ceramic, *Proc. SPIE*, **4375** (2001) 71-78.
83. Zheng, J. & Forslund, B., On the thermal stability and oxidation behaviour of aluminium oxynitride (AlON) powder, *Chinese J. Mater. Res.*, **12** (1998) 497-506.
84. Wang, X., Sichen, D., Li, W. & Seetharaman, S., Kinetic studies of the oxidation of γ-aluminum oxynitride, *Metallurgical and Materials Transactions B*, **33** (2002) 201-207.
85. Willems, H. X., de With, G. & Metselaar, R., Thermodynamics of Alon III: stabilization of Alon with MgO, *J. Eur. Ceram. Soc.*, **12** (1993) 43-49.
86. Apetz, R. & van Bruggen, M. P. B., Transparent alumina: a light scattering model, *J. Am. Ceram. Soc.*, **86** (2003) 480-486.
87. Tilley, R., Colour and optical properties of materials, England: John Wiley & Sons, Ltd, 2000.
88. Peerlen, J. G. J. & Metselaar, R., Light scattering by pores in polycrystalline materials: transmission properties of alumina, *J. Appl. Phys.* **45** (1974) 216-220.
89. Schroeder, J. & Rosolowski, J. H., Light scattering in polycrystalline materials, *Proc. SPIE*, **297** (1981) 156-168.
90. Gilde, G., Patel, P. & Patterson, M., A comparison of hot-pressing, rate-controlled sintering, and microwave sintering of magnesium aluminate spinel for optical applications, *Proc. SPIE*, **3705** (1999) 94-104.

91. Patel, P. J., Gilde, G. A., Dehmer, P. G. & McCauley, J. W., Transparent ceramics for armor and EM window applications, *Proc. SPIE*, **4102** (2000) 1-14.
92. Beyer, R. A. & Kerwien, H., Evaluation of ALON for cannon window application, *Proc. SPIE*, **3705** (1999) 113-118.
93. Bass, M., editor in chief, Handbook of Optics – Volume II: Devices, Measurements & Properties, New York: McGraw-Hill, Inc., 1995.
94. Cullity, B. D., Elements of X-ray diffraction, Addison-Wesley Publishing Company, Inc., Reading, Massachusetts (1956) 324-343.
95. Aharon, O., HIP Processing of Metal-Alumina Nanocomposites, MSc Thesis, Technion – Israel Institute of Technology, Israel, 2001.
96. Burns, S. J., Funkenbusch, P. D., Gracewski, S. M., Lambropoulos, J. C. & Ruckman, J., Surface features and residual strains in AlON grinding, *Proc. SPIE*, **4451** (2001) 165-173.

השפעת תוספי סנטור על המיקרומבנה והתכונות של AlON

יחזקאל אשוח

השפעת תוספי סנטור על המיקרומבנה והתכונות של AlON

חיבור על מחקר
לשם מילוי חלקי של הדרישות לקבלת התואר
מגיסטר למדעים בהנדסת חומרים

יחזקאל אשוח

הוגש לסנט הטכניון – מכון טכנולוגי לישראל
טבת תשס״ד חיפה דצמבר 2003

מוקדש להוריי, מקור לתמיכה אינסופית.

המחקר נעשה בהנחיית פרופ׳ וויין קפלן בפקולטה להנדסת חומרים.

תודות

ברצוני להודות לפרופ׳ וויין קפלן על התמיכה, העזרה וההנחיה המסורה.

אני מודה ומעריך את תמיכת רפאל – חנ״ם בהשכלתי ובמחקר זה.

כמו כן ברצוני להודות לרפאל – שמחו״ת (מחלקת מטלורגיה וחומרים קרמיים) על החופש שניתן לי בשימוש בציוד המחלקה לצורך ביצוע העבודה המעשית.

אני אסיר תודה לדוד גורני, שמשון בר-זיו, שלומית זמיר, אורן אהרון, יצחק באום ויהושע חכמו משמחו״ת על עזרתם הרבה במהלך העבודה.

תודה לד״ר אלכס ברנר על הסיוע בביצוע אנליזה כמותית.

תודה לחדווה ציפין משמחו״ת על הסיוע במדידות העברת אור.

תודה למייק ליברטל ולחבריי בקבוצת הקרמיקה על תמיכתם.

תודה מיוחדת לד״ר שוקי ישורון על התמיכה בי לכל אורך הדרך.

תוכן העניינים

תקציר **1**

רשימת סמלים וקיצורים **3**

1. מבוא **5**

2. סקר ספרות **6**

2.1 הרכב ומבנה של AlON 6

2.2 ייצור 13

2.2.1 סנטור ריאקציה 14

2.2.2 חינקון קרבותרמלי של אלומינה 18

2.2.3 תהליכי ייצור אחרים 19

2.2.4 לחיצה חמה של AlON 20

2.2.5 סנטור במיקרוגל של AlON 21

2.2.6 חומרים מרוכבים של AlON 21

2.3 השפעת תוספים 22

2.3.1 תוספים לאלומינה שקופה למחצה 22

2.3.2 תוספים ל-AlON שקוף 26

2.4 תכונות 28

2.4.1 תכונות מכניות 29

2.4.2 תכונות אופטיות 30

2.4.3 עמידות בחמצון 31

2.4.4 עמידות כימית 32

2.5 שקיפות 33

2.5.1 אינטראקציה בין אור לחומר 33

2.5.1.1 החזרה 35

2.5.1.2 בליעה 35

2.5.1.3 פיזור 36

2.5.2 מקורות פיזור אור במיקרומבנה וההשפעה על השקיפות 38

2.5.2.1 פיזור אור מנקבוביות 39

2.5.2.2 השפעת גודל הגרעין על הפיזור 41

2.6 יישומים 42

תוכן העניינים (המשך)

3. מטרות המחקר **44**

4. שיטות ניסיוניות **45**

4.1 תיאור התהליך 45

4.2 שיטות אפיון 48

4.2.1 צפיפות 48

4.2.2 קשיות 48

4.2.3 בדיקת הרכב כימי 48

4.2.4 דיפרקצית קרני-X (XRD) 48

4.2.5 מיקרוסקופ אלקטרונים סורק (SEM) 49

4.2.6 EDS 49

4.2.7 WDS 49

4.2.8 מיקרוסקופ אלקטרונים חודר (TEM) 49

4.2.9 ספקטרופוטומטר 49

5. תוצאות **50**

5.1 פיתוח התהליך 50

5.2 בדיקה דילטומטרית 51

5.3 זיהוי פאזות באמצעות XRD 54

5.3.1 מרקמי דיפרקציית קרני-X של AlON 54

5.3.2 חישוב פרמטרי שריג 59

5.4 אנליזה כמותית של יסודות 60

5.4.1 בדיקת הרכב כימי 60

5.4.2 בדיקות באמצעות EDS ו-WDS 62

5.5 אפיון המיקרומבנה 63

5.5.1 מיקרומבנה של דגמים מאוכלים 63

5.5.2 פני שבר 68

5.5.3 מדידות גודל גרעין 77

5.5.4 אפיון באמצעות TEM 78

5.6 העברת אור 81

5.7 ניסוי עמידות בחמצון 82

5.8 מדידות קשיות 84

תוכן העניינים (המשך)

6. דיון **85**

6.1 דיון בתהליך

6.2 דיון בהשפעת התוספים

6.3 דיון בפאזה הנוזלית

7. סיכום **89**

8. הצעות להמשך המחקר **90**

9. מקורות **91**

רשימת ציורים

ציור 2.1. דיאגרמת פאזות של המערכת הפסאודו-בינארית $AlN\text{-}Al_2O_3$. 6

ציור 2.2. איור סכמטי של מבנה ספינל. 10

ציור 2.3. השפעת טמפרטורת הריאקציה על השבר הנפחי של Al_2O_3, AlN ו-AlON (זמן הריאקציה 2.5 שעות), מבוטאת כיחסים בין עוצמות פיקים של XRD. 16

ציור 2.4. השפעת זמן הריאקציה על השבר הנפחי של AlN שלא הגיב (טמפרטורת הריאקציה: □ 1820°C, ■ 1750°C). 16

ציור 2.5. תלות פרמטר השריג של AlON בריכוז ההתחלתי של Al_2O_3. 17

ציור 2.6. a) צפיפות סופית ו-b) גודל גרעין סופי, כתלות בריכוז ה-MgO בדגמי אלומינה מסונטרים. 24

ציור 2.7. דיאגרמת פאזות סכמטית המראה את תחום ההרכבים שבו מתקבלת העברת אור מקסימלית באלומינה עם תוספות MgO, Y_2O_3 ו-La_2O_3. 26

ציור 2.8. העברת אור דרך AlON בתחומי האור האולטרה-סגול, הנראה והאינפרא-אדום. 30

ציור 2.9. חלון AlON שיוצר ע"י Raytheon בשנת 1986. 31

ציור 2.10. התחמצנות AlON באוויר בטמפרטורות שונות כתלות בזמן. 32

ציור 2.11. תיאור של העברת האור של (a) חומר עכור עם העברה דיפוסיבית גבוהה והעברה ישירה נמוכה ו-(b) חומר שקוף עם העברה דיפוסיבית נמוכה והעברה ישירה גבוהה. 33

ציור 2.12. האינטראקציה של אור עם חומר שקוף. 34

ציור 2.13. השפעת גודל החלקיקים על מקדם הפיזור היחסי. 37

ציור 2.14. פיזור האור בגבולות גרעינים מתרחש רק בחומרים אנאיזוטרופיים. 38

ציור 2.15. עקומות העברה מחושבות עבור דגם אלומינה בעובי 0.5 מ"מ עם 0.2% נקבוביות בגדלים אחידים שונים, כתלות באורך הגל. 40

ציור 2.16. העברת אור בקו ישר וכללית (כולל פיזור קדימה) באורך גל 600 nm, נקבוביות כללית 0.1% ועובי 0.8 mm, בהנחה שהנקבוביות בגודל אחיד ומפוזרות באופן אחיד בתוך מטריצה הומוגנית עם n=1.76 (עבור אלומינה). 41

ציור 5.1. התכווצות יחסית כתלות בזמן הסנטור של AlON עם תוספים וללא תוספים. 53

ציור 5.2. התכווצות יחסית כתלות בטמפרטורת הסנטור של AlON עם תוספים וללא תוספים. 53

רשימת ציורים (המשך)

ציור 5.3. a) דיפרקציית קרני-X של אבקת AlON שהוכנה ב-1750°C למשך 4 שעות, b) XRD של אבקת AlON שיוצרה ע"י Sienna; ○ - AlON , ♦ - AlN , ● - Al_2O_3. 55

ציור 5.4. דיפרקציית קרני-X של דגם AlON מסוג E שסונטר ב-1800°C למשך שעתיים ואחרי כן ב-1950^0C למשך שעתיים: a) מייד לאחר הסנטור, b) אחרי ליטוש; ○ - AlON , Δ - AlN. 57

ציור 5.5. XRD של דגמי AlON שונים: a) מסוג J, b) מסוג LA. 58

ציור 5.6. פרמטרי שריג שחושבו לדגמי AlON שונים (עם תוספים וללא תוספים) עם ערכים שונים של היחס Al_2O_3\AlN, בהשוואה לתוצאות מהספרות. 60

ציור 5.7. תמונת מיקרוסקופ אופטי של דגם מסוג J שסונטר ב-2010°C למשך 12 שעות (במקור x12.5). 64

ציור 5.8. תמונת מיקרוסקופ אופטי של דגם מסוג MC שסונטר ב-2010°C למשך 12 שעות (במקור x12.5). 64

ציור 5.9. תמונת מיקרוסקופ אופטי של דגם מסוג MB שסונטר ב-2010°C למשך 12 שעות (במקור x12.5). 65

ציור 5.10. תמונת מיקרוסקופ אופטי של דגם מסוג MYA שסונטר ב-1930°C למשך 12 שעות (במקור x12.5). 65

ציור 5.11. תמונת מיקרוסקופ אופטי של דגם מסוג LA שסונטר ב-1930°C למשך 12 שעות (במקור x12.5). 66

ציור 5.12. תמונת מיקרוסקופ אופטי של דגם מסוג YLA שסונטר ב-1930°C למשך 12 שעות (במקור x12.5). 66

ציור 5.13. תמונת SEM של דגם מסוג MLD שסונטר ב-2000°C למשך 12 שעות (במקור x40). 67

ציור 5.14. תמונת מיקרוסקופ אופטי של דגם שקוף מתוצרת Surmet (במקור x25). 68

ציור 5.15. תמונת פני שבר ב-SEM של דגם AlON מסוג E, שסונטר בתהליך דו-שלבי: 1800°C למשך 2 שעות, ואחרי כן 1950°C למשך 2 שעות (במקור x1000). 69

ציור 5.16. תמונת פני שבר ב-SEM של דגם מסוג F, שסונטר ב-1950°C למשך 4 שעות (קצב חימום של 500 °C/hr, במקור x500). 70

ציור 5.17. תמונת פני שבר ב-SEM של דגם מסוג F, שסונטר ב-1950°C למשך 4 שעות (קצב חימום של 900 °C/hr, במקור x500). 70

רשימת ציורים (המשך)

ציור 5.18. תמונת פני שבר ב-SEM של דגם מסוג I, שסונטר ב-2000°C למשך 12 שעות (במקור x250). 71

ציור 5.19. תמונת פני שבר ב-SEM של דגם מסוג MA, שסונטר ב-1950°C למשך 4 שעות (במקור x500). 72

ציור 5.20. תמונת פני שבר ב-SEM של דגם מסוג LA, שסונטר ב-1950°C למשך 12 שעות (במקור x250). 72

ציור 5.22. תמונת פני שבר ב-SEM של דגם מסוג YLA, שסונטר ב-2000°C למשך 12 שעות (במקור x250). 73

ציור 5.23. תמונות פני שבר ב-SEM של מיפוי יסודות בדגם מסוג MLD, שסונטר ב-1950°C למשך 12 שעות (במקור x500). 75

ציור 5.24. דיפרקצית קרני-X של דגם מסוג MLD, שסונטר ב-1950°C למשך 12 שעות; ○ - AlON , ∇ - $LaAl_{11}O_{18}$. 76

ציור 5.25. תמונת TEM של גבול גרעין בדגם מסוג MLA. 79

ציור 5.26. מרקם דיפרקציית אלקטרונים מגרעין AlON בדגם MLA. 79

ציור 5.27. תמונת TEM של גבול גרעין משולש בדגם AlON שקוף מ-Surmet. 80

ציור 5.28. מרקם דיפרקציית אלקטרונים מגרעין AlON בדגם שקוף מ-Surmet. 80

ציור 5.29. צילומים של דגמי AlON המונחים על גבי דף שעליו רשומה המילה "ALON": a) דגם מסוג F בעובי 1.66 mm, שסונטר ב-2025°C למשך 4 שעות, b) דגם מסוג MA בעובי 2.8 mm, שסונטר ב-2025°C למשך 12 שעות. 81

ציור 5.30. עקומי העברת אור של דגם AlON מסוג MA ודגם AlON שקוף שיוצר ע"י Surmet, בתחומי האור האולטרה-סגול, הנראה והאינפרא-אדום. 82

ציור 5.31. מרקמי דיפרקציית קרני-X של דגם AlON מתוצרת Surmet, שהיה במקור שקוף, אחרי ניסוי עמידות בחמצון בטמפרטורה 2000°C למשך 4 שעות: a) החלק התחתון (השקוף), b) החלק העליון (האטום); ○ - AlON , Δ - AlN , ● - Al_2O_3. 83

ציור 5.32. תמונת מיקרוסקופ אופטי של דגם AlON מאוכל מתוצרת Surmet אחרי חימום ל-2000°C למשך 4 שעות. 83

ציור 6.1. דיאגרמת פאזות של המערכת הקוואזי-בינארית La_2O_3-Al_2O_3 מעל 1800°C. 86

רשימת טבלאות

טבלה 2.1. פאזות אלומיניום אוקסיניטריד שנצפו במערכת הפסאודו-בינארית $AlN\text{-}Al_2O_3$. 9

טבלה 2.2. הרכבים של אלומיניום אוקסיניטריד במודל האניונים הקבועים של McCauley. 12

טבלה 2.3. ריאקציות כימיות הידועות כיוצרות פאזות AlON. 13

טבלה 2.4. תכונות מייצגות של AlON בהשוואה לקרמיקות דומות אחרות: אלומינה ($\alpha\text{-}Al_2O_3$), אלומיניום ניטריד (AlN) וספינל ($MgAl_2O_4$) שקוף. 29

טבלה 4.1. חומרי גלם ($\alpha\text{-}Al_2O_3$, AlN) ששימשו לייצור AlON. 45

טבלה 4.2. תוספי סנטור ששימשו לייצור AlON. 46

טבלה 4.3. הרכבים של תערובות אבקות שהוכנו לצורך סנטור AlON. 47

טבלה 5.1. החזרות המשויכות ל-AlON עם פרמטר שריג של 0.7950 nm (בקרינת Cu Kα). העמודה האחרונה מציינת האם נעשה שימוש בהחזרה לצורך חישוב פרמטר השריג. 56

טבלה 5.2. ההרכב של תערובות אבקות ושל אריח AlON שקוף מתוצרת Surmet. בסוגריים ריכוזי התוספים שהוספו לתערובות. 61

טבלה 5.3. ההרכב של דגמים מסונטרים של AlON שנמדד ע"י EDS ו-WDS. 62

טבלה 5.4. גודל גרעין ממוצע שנמדד עבור דגמים בהרכבים שונים, שסונטרו בטמפרטורות וזמנים שונים. 77

טבלה 5.5. קשיות Knoop שנמדדה עבור דגמים בהרכבים שונים, שסונטרו בטמפרטורות וזמנים שונים. 84

תקציר

γ-אלומיניום אוקסיניטריד (AlON) הוא חומר קרמי שקוף בעל קשיות גבוהה יחסית. כמו חומרים קרמיים רבים אחרים, הוא בעל עמידות כימית ותרמית טובה. הצירוף הייחודי הזה של תכונות ה-AlON גורם לחומר להיות מועמד אטרקטיבי למגוון של יישומים הדורשים קושי גבוה ושקיפות בתחום אורכי הגל 0.2-5.5 μm. היישומים הבולטים לחומר כזה הם: מיגון שקוף וכיפות לטילים. חומר אחר בעל תכונות דומות הוא ספיר, אך בהיותו חד-גבישי שיטות הייצור שלו יקרות יחסית. מכיוון ש-AlON הוא רב-גבישי, הוא מיוצר בסנטור רגיל ולכן יכול להוות אלטרנטיבה זולה לספיר לצורך יישומים שונים.

AlON הוא תמיסה מוצקה במערכת הפסאודו-בינארית Al_2O_3-AlN, שעל פי המודל המקובל, הנוסחה הסטויכיומטרית שלו היא $Al_{23}O_{27}N_5$. הוא יציב תרמודינמית רק בטמפרטורות מעל 1640°C~, וניתך מעל 2100°C. המבנה הקריסטלוגרפי של AlON הוא מבנה ספינל (קובי), ולכן תכונותיו האופטיות הן איזוטרופיות. שתי שיטות הייצור העיקריות שלו הן מתערובות של אבקות אלומינה ו-AlN או אלומינה וגרפיט, באווירת חנקן. בעבודות בספרות הסנטור מתבצע בדרך כלל ללא לחץ, אם כי בוצעו גם עבודות שכללו תהליכי כבישה חמה. תהליך נוסף שדווחו עבורו תוצאות מעודדות מבחינת השקיפות הוא סנטור במיקרוגל, שלו יתרון של קצב סנטור גבוה במיוחד.

בסנטור ללא לחץ של תערובות האבקות מתקבל בדרך כלל AlON חד-פאזי בצבע לבן, כתוצאה מפיזור האור ע״י גורמים שונים בחומר. גורמי הפיזור החשובים ביותר הן הנקבוביות, מכיוון שמקדם השבירה שלהן שונה במידה רבה מזה של AlON, ומכיוון שהן מצויות בחומר בכמות גדולה יחסית. הייצור של AlON שקוף הוא אתגר גדול מאוד, מכיוון שיש להקטין את הנקבוביות השיורית למינימום מוחלט, הרבה מעבר למה שנדרש בתהליכי סנטור רגילים. מרכזי פיזור נוספים בחומר הם כל הגורמים שמקדם השבירה שלהם שונה מזה של AlON: זיהומים, מתבדלים, פאזות משניות, גבולות גרעין ואזורים של הרכב אי-הומוגני. לכן, חומרי הגלם המשמשים להכנת AlON צריכים להיות טהורים ועדינים ככל שניתן. כמו כן, ככל שהגרעינים של החומר המסונטר יהיו גדולים יותר, כך יתקבל פחות פיזור אור מגבולות הגרעינים.

אחת הדרכים להשגת צפיפות קרובה ל-100% היא באמצעות תוספי סנטור, המסייעים לציפוף ע״י יצירת פאזה נוזלית. המטרה העיקרית של המחקר הנוכחי הייתה לחקור את ההשפעה של תוספי סנטור (מגנזיום, לנתנום ואיטריום) על המיקרומבנה והעברת האור

של AlON. כשלב ראשון להשגת מטרה זו, פותח תהליך סנטור-ריאקציה בטמפרטורות גבוהות (~2000°C), בתנור עם אלמנטי חימום מגרפיט. דגמי AlON הוכנו מתערובות של Al_2O_3 ו-AlN, שלחלקן הוספו תוספי סנטור בריכוזים ובצירופים שונים. המיקרומבנה של החומר המסונטר נחקר כתלות בריכוז התוספים ובפרמטרי הסנטור (טמפרטורה וזמן).

בבדיקה דילטומטרית שבוצעה לדגם עם תוספים בהשוואה לדגם AlON טהור, נמצא הבדל בין פרופילי הציפוף כתלות בטמפרטורה עבור שני הדגמים. בשלב הריאקציה של תערובת האבקות ליצירת AlON, המתרחש בסביבות $1750\text{-}1800^0C$, מתרחשת עלייה ניכרת בנפח כתוצאה מהפרש בין נפח תא היחידה של AlON לסכום הנפחים של תאי היחידה של Al_2O_3 ו-AlN (ביחסים המתאימים). עלייה זו קטנה באופן ניכר בפרופיל של הדגם עם התוספים לעומת הדגם הטהור, ככל הנראה כתוצאה מסידור מחדש של הגרגרים המתרחש במקביל לריאקציה, בקלות יחסית, בנוכחות פאזה נוזלית.

אנליזות הרכב שבוצעו הראו שריכוז יסודות התוספים בתוך גרעיני ה-AlON הוא קרוב לריכוז התוספים שהוכנס בשלב ערבוב האבקה. משמעותה של תוצאה זו היא שקיימת מסיסות של יסודות אלה בתוך AlON, בריכוזים הנמוכים שנבדקו. אולם, בחומר עם ריכוז La של 0.2 wt.%, נמצא שהתוסף מפוזר באופן לא הומוגני וקיים בעיקר באזורים מסוימים. זוהי עדות לכך שריכוז זה הוא מעל לגבול המסיסות של La ב-AlON.

בדיקות דיפרקציית קרני-X הראו שבפני השטח של הדגמים המסונטרים קיימות הפאזות AlON ו-AlN, ואילו רוב החומר הוא AlON חד-פאזי. לכן, לקבלת שקיפות יש ללטש ולהסיר את שכבת פני השטח של החומר. מרקמי דיפרקציית קרני-X מדגמים שונים הראו חוסר עקביות ביחסי העוצמות של השיאים שהתקבלו, הנובעים מגודל הגרעין הגדול שהתקבל בסנטור הממושך בטמפרטורה גבוהה (100-200 μm). תוצאות הדיפרקציה שימשו לחישוב פרמטר השריג של AlON, שהתקבל בממוצע בתחום 0.7948-0.7954 nm, כתלות בריכוז החנקן בדגם. תוצאות אלה מתאימות למדידות המופיעות בספרות.

דגמי AlON עברו ליטוש ואיכול כימי בחומצה זרחתית רותחת, בתהליך איכול שפותח ונמצא המתאים ביותר לדגמי ה-AlON. תמונות מיקרומבנה של דגמים מאוכלים הראו עלייה בגודל הגרעין עם העלאת הטמפרטורה. תופעה נוספת שנצפתה היא הופעת פגמי תאום רבים בכל הדגמים שבהם נעשה שימוש ב-La. תמונות פני שבר איפשרו להתרשם בצורה טובה מכמות הנקבוביות, מהגודל ומהפיזור שלהן. ניתן היה לראות בבירור

שתוספי הסנטור גורמים להקטנה ניכרת בכמות הנקבוביות. יחד עם זאת, בדגמים עם תוסף Y נצפו נקבוביות גדולות יחסית, חלקן בגודל של עד עשרות מיקרונים, שגורמות לפיזור משמעותי של האור. לעומת זאת, בדגמים עם התוספים Mg ו-La גודל הנקבוביות הקטן תרם לשיפור ניכר בשקיפות. כאשר ריכוז ה-La היה 0.1 wt.% או יותר, הופיעה פאזה משנית בגבולות הגרעינים, שבדיפרקציית קרני-X התגלתה כ-$LaAl_{11}O_{18}$. בבדיקת TEM של גבול גרעין בדגם עם Mg ו-La (מתחת לריכוז שיוצר פאזה משנית) לא נתגלו זיהומים או חלקיקים זרים כלשהם. יחד עם זאת, רק בבדיקת TEM ברזולוציה גבוהה ניתן יהיה לדעת אם קיימת בגבולות הגרעין שכבה דקה של אטומי התוספים.

הדגמים בעלי השקיפות הטובה ביותר כללו תוספי 0.3 wt.% Mg ו-0.02 wt.% La, או Mg בלבד, שסונטרו ב-2025°C למשך 12 שעות. אחוזי העברת אור שנמדדו באמצעות ספקטרופוטומטר היו עד כ-17% באור נראה וכ-25% בתחום האינפרא-אדום, עבור דגם בעובי של כ-2.8 מ״מ. תמונות המיקרומבנה הראו שבמקרים אלה התקבלה כמות נקבוביות נמוכה מאוד. לעומת זאת, בדגמים עם תוסף Y התקבל שיפור קל בלבד בשקיפות בהשוואה ל-AlON טהור, כתוצאה מגודל הנקבוביות.

תוספי הסנטור גורמים ליצירת פאזה נוזלית בחומר בטמפרטורת הסנטור הגבוהה, המאפשרת בתחילת הסנטור לגרגרי ה-AlON להסתדר מחדש בצורה צפופה יותר. בהמשך התהליך הגרגרים יוצרים לחץ על הנוזל שביניהם, עד לקבלת שכבה נוזלית דקה המקיפה את רוב הגרעינים. הנקבוביות מצטברת בעיקר בגבולות הגרעינים, ובשלבים מאוחרים יותר היא יוצאת מהחומר במנגנון של דיפוזיה דרך גבולות הגרעינים. התוצאה הסופית היא הקטנת כמות הנקבוביות בחומר.